JOHANNES GUTENBERG UNIVERSITÄT MAINZ

JG|U

Thermochromatographic studies of thallium isotopes on SiO_2 and α-Al_2O_3 surfaces

Thermochromatographische Untersuchungen von Thalliumisotopen auf SiO_2- und α-Al_2O_3-Oberflächen

Masterarbeit
zur Erlangung des Grades
»Master of Science«

dem Fachbereich Chemie, Pharmazie und Geowissenschaften
der Johannes Gutenberg-Universität in Mainz
vorgelegt von

Felix Ludwig Sprunk
geboren am 26. April 2000 in Bernkastel-Kues

Mainz, Mai 2025

Masterarbeit im Studiengang Chemie an der Johannes Gutenberg-Universität Mainz

Ich, Felix Ludwig Sprunk, Matrikelnummer 2754782, versichere, dass ich meine Masterarbeit selbstständig verfasst und keine anderen als die angegebenen schriftlichen und elektronischen Quellen sowie andere Hilfsmittel benutzt habe. Alle Ausführungen, die anderen Schriften wörtlich oder sinngemäß entnommen wurden, habe ich kenntlich gemacht.

Mainz, 31. Mai 2025

Felix Ludwig Sprunk

Betreut durch: Katharina Hermainski
Erstgutachter: Professor Dr. Christoph Düllmann
Zweitgutachter: Professor Dr. Michael Block

Die vorliegende Arbeit wurde von Dezember 2024 bis Mai 2025 im Arbeitskreis von Prof. Dr. Christoph Düllmann am GSI Helmholtzzentrum für Schwerionenforschung in Darmstadt angefertigt.

Acknowledgements

Firstly, I would like to express my sincere gratitude to Prof. Dr. Christoph Düllmann for the opportunity to conduct my master's thesis within the SHE chemistry group at GSI. Thank you for your time, your valuable feedback, and the trust you placed in me and my work. I would also like to thank my second examiner, Prof. Dr. Michael Block, for taking the time to read and evaluate my thesis.

I am especially grateful to my supervisor and good friend Katharina Hermainski. You always found time to answer my many questions, were open to my ideas, and supported me in every possible way. Your hard work and passion for science were truly inspiring.

Special thanks also go to Dr. Alexander Yakushev, who patiently answered every question I had and provided invaluable support through his experience and calmness. I would also like to thank Dr. Pavol Mosat and Dr. Jochen Ballof for their help, their time, and their support during our beamtimes in Řež. Also many thanks to Dr. Jadambaa Khuyagbaatar, Jörg Krier and Raul Cantemir for their help in preparing the experiments. My thanks extend to all other members of the research group, who created a pleasant and productive working atmosphere and offered help whenever problems arose.

I am also grateful to our colleagues from the Czech Technical University in Prague, especially Prof. Dr. Jan John and Dr. Pavel Bartl, as well as to Prof. Dr. Jon Petter Omtvedt from the University of Oslo, for their assistance and expertise during the experiments. Many thanks as well to the cyclotron operators in Řež for providing a stable beam throughout our measurements.

Last but certainly not least, I want to thank my parents, who supported me unconditionally, and my friends, who were always by my side.

Abstract (Zusammenfassung)

To gain a better understanding of the chemical behaviour of the superheavy element nihonium, several single-atom experiments with its lighter homologue thallium have been performed in the past. As these studies yielded partly contradictory results regarding the deposited species and their adsorption enthalpies, additional thermochromatography experiments were carried out in this work. The thallium isotopes ^{195}Tl and ^{196}Tl were produced by irradiating a gold target at the cyclotron of the nuclear physics institute of the Czech academy of sciences, Řež. The experiments were conducted offline, and the deposited species were analysed using gamma spectroscopy. Measurements were performed on quartz glass columns using oxygen, helium, and moist helium as carrier gases, and on an α-Al_2O_3 column using helium as the carrier gas. Thallium was found to be highly reactive, readily forming compounds with trace amounts of water or oxygen in the mobile phase or on the column surface. A species with an adsorption enthalpy of -123^{+4}_{-3} kJ/mol was observed and, in agreement with literature data, attributed to TlOH. In addition, several measurements with reactive gases imply a complex system between thallium, the added gases and the surface leading to species with different adsorption enthalpies. Due to the nearly identical experimental conditions in the helium-based experiments on quartz glass and α-aluminium oxide, the depositions observed on the latter were interpreted in the same way as on quartz glass. The adsorption enthalpy of metallic thallium could not be determined in the course of these studies, as no elemental thallium was observed, likely due to its high reactivity, even under the most inert conditions achievable in the experimental setup. In addition, experiments were conducted with the aim of hydroxylating or dehydroxylating quartz glass surfaces and identifying a suitable method to determine their hydroxylation state. Reflection–absorption infrared spectroscopy (RAIRS) was found to be an appropriate analytical technique for this purpose. Experimental results for the surface hydroxylation were largely consistent with expectations.

Um das chemische Verhalten des superschweren Elements Nihonium besser zu verstehen, wurden in der Vergangenheit mehrere Einzelatom-Experimente mit seinem leichteren Homologen Thallium durchgeführt. Da diese Untersuchungen teilweise widersprüchliche Ergebnisse hinsichtlich der abgeschiedenen Spezies und ihrer Adsorptionsenthalpien lieferten, wurden im Rahmen dieser Arbeit ergänzende thermochromatographische Experimente durchgeführt. Die Thalliumisotope ^{195}Tl und ^{196}Tl wurden durch Bestrahlung eines Goldtargets am Zyklotron des NPI CAS, Řež erzeugt. Die Experimente wurden offline durchgeführt; die abgeschiedenen Spezies wurden mittels Gammaspektroskopie analysiert. Die Messungen erfolgten an Quarzglaskolonnen unter Verwendung von Sauerstoff, Helium und feuchtem Helium als Trägergas sowie an α-Al_2O_3-Kolonnen mit Helium als Trägergas. Thallium erwies sich als hochreaktiv und reagierte bereits mit Spuren von Wasser oder Sauerstoff in der mobilen Phase oder auf der Kolonnenoberfläche. Es wurde eine Spezies mit einer Adsorptionsenthalpie von -123^{+4}_{-3} kJ/mol beobachtet, die in Übereinstimmung mit Literaturdaten TlOH zugeordnet wurde. Darüber hinaus implizieren mehrere Messungen mit den reaktiven Gasen, dass ein komplexes System zwischen Thallium, den zugesetzten Gasen und der Oberfläche besteht, die zu mehreren Spezies mit unterschiedlicher Adsorbtionsenthalpie führt. Aufgrund der nahezu identischen experimentellen Bedingungen in den Helium-basierten Experimenten an Quarzglas und α-Aluminiumoxid wurden auch die auf letzterem beobachteten Ablagerungen genauso interpretiert wie auf Quartzglas. Die Adsorptionsenthalpie von metallischem Thallium konnte im Rahmen dieser Arbeit nicht bestimmt werden, da kein elementares Thallium nachgewiesen wurde, vermutlich aufgrund seiner hohen Reaktivität, selbst unter den inertesten im Experiment erreichbaren Bedingungen. Zusätzlich wurden Experimente durchgeführt, um Quarzglasoberflächen gezielt zu hydroxylieren bzw. zu dehydroxylieren und eine geeignete Methode zur Bestimmung ihres Hydroxylierungsgrades zu finden. Es zeigte sich, dass die Reflexions-Absorptions-Infrarotspektroskopie (RAIRS) eine geeignete Analysemethode für diesen Zweck darstellt. Die erzielten Ergebnisse zur Hydroxylierung erfüllten zum großen Teil die Erwartungen.

Contents

1 Introduction **1**

2 Theoretical background **3**
2.1 Stability of superheavy elements . . . 3
2.1.1 The liquid drop model . . . 3
2.1.2 The nuclear shell model . . . 5
2.1.3 Superheavy elements . . . 5
2.2 Production of superheavy elements . . . 7
2.3 Relativistic effects . . . 9
2.4 Single-atom-chemistry and Monte Carlo simulation . . . 10
2.4.1 Single-atom-chemistry and -chromatography . . . 10
2.4.2 Monte Carlo simulation . . . 13
2.5 The chemistry of thallium . . . 15
2.5.1 Thallium hydroxides . . . 15
2.5.2 Thallium oxides . . . 15
2.5.3 Previous single atom studies of thallium . . . 16
2.6 Column surfaces . . . 18
2.6.1 Quartz glass . . . 18
2.6.2 Aluminium oxide . . . 20
2.6.3 Methods for surface examination . . . 21

3 Experimental and methods **23**
3.1 Examination of quartz glass surfaces . . . 23
3.1.1 Modification of quartz glass surfaces with (heavy) water . . . 23
3.1.2 Surface examination of the quartz plates using reflection-absorption infrared spectroscopy (RAIRS) . . . 24
3.2 Thermochromatographic studies of thallium . . . 25
3.2.1 Pre-treatment of the chromatography columns . . . 25
3.2.2 Thermochromatographic studies . . . 26
3.2.3 Evaluation process . . . 30

4 Results **35**
4.1 Examining of quartz glass surfaces . . . 35
4.2 Thermochromatographic studies of thallium . . . 36

4.2.1 Determination of the adsorption enthalpy of thallium on quartz glass in a pure helium atmosphere . . . 36
4.2.2 Determination of the adsorption enthalpy of thallium on quartz glass in a helium and oxygen atmosphere (Tl-O2-700) . . . 39
4.2.3 Determination of the adsorption enthalpy of thallium on quartz glass in a wet helium atmosphere (Tl-H2O-700) . . . 42
4.2.4 Determination of the adsorption enthalpy of thallium in a pure helium atmosphere on alpha-aluminium oxide (Tl-He-700-Al2O3) 45
4.2.5 Determination of the adsorption enthalpy of thallium on quartz glass in a pure oxygen atmosphere (Tl-pure-O2-700) . . . 48

5 Discussion and interpretation of the results 51
5.1 Examination of quartz glass surfaces . . . 51
5.2 Thermochromatographic studies of thallium . . . 52
5.2.1 Determined adsorption enthalpies of thallium species on quartz glass . . . 52
5.2.2 Determined adsorption enthalpies of thallium species on alpha-aluminium oxide . . . 55

6 Summary and outlook 57

7 Appendix 71
7.1 Evaluation of the Tl-He-300 experiment . . . 71
7.2 Temperature gradients . . . 72
7.3 Determination of the influence of the surface roughness of different materials on the adsorption enthalpy . . . 85

Chapter 1

Introduction

In 1869, Dmitri Mendelejew introduced the periodic table, arranging all known elements at the time by their atomic mass. He observed a recurring pattern in their chemical behaviour, which formed the basis of the periodic table.[1] Over the years, as new elements were discovered, the periodic table expanded and remains in use today, albeit with modifications to its classification.[2,3] One significant change was the shift from ordering elements by atomic mass to ordering them by the number of protons, known as the atomic number Z.[3,4]

Uranium ($Z = 92$) has the highest atomic number among naturally occurring elements. With the synthesis of the first transuranium elements, neptunium and plutonium in 1940, a race to discover new elements began.[5,6] Over the following decades, various research groups worldwide synthesized numerous new elements, pushing the perceived limits of the periodic table.[3,5,6] To date, all elements up to oganesson ($Z = 118$) have been successfully discovered.[3,7–9]

Due to the high nuclear charge and the resulting Coulomb repulsion, the stability of elements with $Z > 104$ cannot be explained by the liquid drop model alone.[6,7,10,11] Instead, these elements, starting from rutherfordium ($Z = 104$), exist only due to microscopic shell stabilization, as predicted by the nuclear shell model. These so-called transactinide elements, also referred to as superheavy elements (SHE), exhibit unique nuclear properties.[6,7,10] Since SHE are produced with extremely low cross sections, typically resulting in the creation of only one atom at a time, traditional macroscopic chemical investigations are impossible. This challenge has led to the development of novel experimental approaches.[3,12]

The periodic table allows for the prediction of certain chemical properties based on the position of an element.[4,7] However, in the realm of SHE (and their lighter homologs in the 7th. period), relativistic effects can cause deviations from established periodic trends, making their chemical properties less predictable based on periodic positioning alone.[7,13–16] Several well-known chemical properties, such as the characteristic color of gold, the stable oxidation states of lead, and the low melting point of mercury, can only be explained by relativistic effects.[17,18] A comprehensive understanding of the chemical behaviour of the lighter homologs of SHE is

crucial for predicting and interpreting gas chromatography experiments, as well as for assessing the influence of relativistic effects on their chemical properties.[6–8,11,19] According to the latest findings, the heaviest element whose chemical properties have been investigated experimentally is moscovium ($Z = 115$).[20] One proven method for investigating SHE is gas chromatography using columns with surfaces made of materials such as gold or quartz.[6,21,22] This technique enables a large number of interactions with a solid surface, whereas the species are immobilized on the surface for a certain time, which depends on the interaction strength between the species and the surface, and than can be desorbed and transported by a gas flow further along a chromatography column. Thus, a spacial separation of species with different volatilities or reactivities can be achieved. These experiments allow for the determination of the adsorption enthalpy, a key parameter in assessing the volatility of the investigated elements.[3,6,7,11,13,14,19]

In this work, single-atom chromatography experiments will be discussed to determine the adsorption enthalpy of thallium ($Z = 81$), the lighter homolog of the superheavy element nihonium ($Z = 113$), on quartz glass and α-Al_2O_3. This investigation is of great importance for characterizing nihonium's chemical properties. To achieve this, multiple experiments will be performed using different compositions of helium, water and oxygen as the mobile phases. Additionally, the influence of varying surface conditions of the chromatography columns on the experimental results will be examined.

Chapter 2

Theoretical background

2.1 Stability of superheavy elements

The binding energy of a nucleus is used to describe its stability.[3,15,23] This energy is defined as the difference between the experimentally determined mass of the nucleus and the theoretical mass obtained by adding up the masses of its constituents, the protons and neutrons.[3,23] There are two widely spread models to describe the binding energy per nucleon and following that the stability of different nuclides, the liquid drop model and the shell model.[3,23]

2.1.1 The liquid drop model

The concept of the liquid drop model (LDM) was introduced by George Gamow in 1930 and was expanded by Carl Friedrich von Weizsäcker in 1935.[3,24] As the name suggests, it is assumed that the atomic nucleus is an incompressible droplet in which the charge and mass are equally distributed. Additionally the LDM assumes that every proton and every neutron is identical and indistinguishable from another.[3,23,25–27]
With equation (2.1) respectively (2.2) it is possible to calculate the binding energy of a certain nucleus without taking quantum mechanical effects into account. The equation was introduced by von Weizsäcker in 1935, further developed by Hans Bethe in 1936, and is therefore called the Bethe–Weizsäcker formula.[3,27–29]

$$E_B = E_V + E_S + E_C + E_A + \delta\,\mathrm{MeV} \tag{2.1}$$

Here E_B represents the binding energy, E_V is the volume energy, E_S is the surface energy, E_C is the Coulomb energy, E_A is the asymmetry energy and δ is the pairing energy.[3]
The volume energy term accounts for the attractive interactions between nucleons within the nuclear volume.[3,27] The negative surface energy term reflects the lowering of the binding energy originating from nucleons with less binding partners on the surface of the nucleus.[3,27] The coulomb repulsion is taken into account by the negative coulomb energy term.[3,27] The asymmetry energy term accounts for the fact that nuclei with equal numbers of protons and neutrons are more stable than others.[3,27]

Finally, the pairing energy term represents the empirical observation that nuclei with an even number of protons and neutrons (even-even nuclei) exhibit increased stability, whereas nuclei with an odd number (odd-odd nuclei) show decreased stability. For nuclei with an odd-even or even-odd configuration, this term is zero.[3,27]
Following these explanations for the different energy terms the Bethe-Weizsäcker-formula can also be written as shown in equation (2.2).[3,27]

$$E_B = c_V \cdot A - c_S \cdot A^{\frac{2}{3}} - c_C \cdot \frac{Z(Z-1)}{A^{\frac{1}{3}}} - c_A \cdot \frac{(A-2Z)^2}{A} + \delta\,\mathrm{MeV} \qquad (2.2)$$

Here A stands for the number of nucleons, Z is the number of protons, the parameters c_V to c_A are proportionality constants obtained by mathematical fitting of empirical data and δ is the pairing term.

A comparison between the binding energies obtained from mass measurements and those calculated using the Bethe–Weizsäcker formula shows overall good agreement. However, for certain proton and neutron numbers, a larger deviation of the experimental data from the theoretical data can be observed, showing a highly increased stability for these nucleon numbers (see figure 2.1).[3,25,27] Notably stable nuclei, so called "magical nuclei" deviate significantly from predictions based on the liquid-drop model. These discrepancies are tied to closed shells in the nuclear potential and signal quantized structural effects, which require a more detailed model for explanation.[3,25,27]

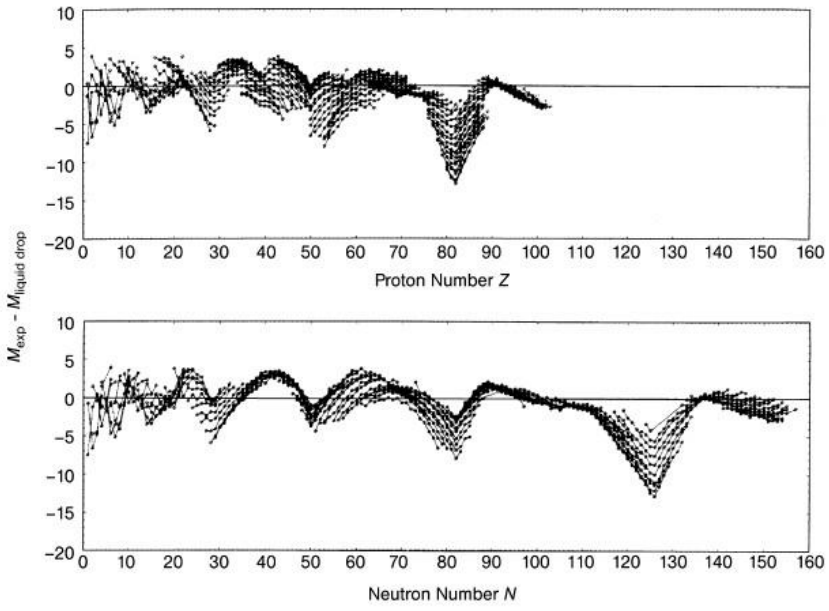

Figure 2.1: Differences between experimental atomic masses and masses calculated with the LDM as a function of proton number (top) or neutron number (bottom). Taken from [3]. Reprinted with permission from Wiley and Sons.

2.1.2 The nuclear shell model

Compared to the liquid drop model (LDM), the nuclear shell model (NSM) differs in two main aspects. First, the NSM does not assume a homogeneous distribution of nucleons within the nucleus. Instead, it posits that nucleons are arranged in specific 'shells', similar to electrons. Secondly, the NSM assumes that two nucleons cannot have the same quantum numbers. This can also be understood as the Pauli-principle, known from electrons, applied to nucleons.[25,27] Thus, in analogy to the Bohr model of the atom, every nucleon can be described with four individual quantum numbers. The main quantum number n describes the shell of the nucleon.[27] Each shell is divided in subshells with the name s, p, d, f and so on. Similarly to the electron orbitals, two nucleons can fit into one subshell. The subshell of each nucleon is described with the orbital quantum number l.[27] The magnetic quantum number m reflects the projection of the orbital angular momentum of the nucleons in the associated orbital.[27] Finally, the spin quantum number s describes the angular momentum of the nucleon.[27]

Assuming a spherical symmetric harmonic oscillator as the nuclear potential of the inert core made it possible to solve the Schrödinger equation for a nucleon moving in this potential. This solution demonstrated the existence of nuclear shell closures at proton and neutron numbers 2, 8, and 20.[3,25,30,31] Solving the Schrödinger equation beyond the third harmonic oscillator results in numbers for completed shells that differ from the experimental expected "magical"ones.[3,30,31] A way to explain the observed higher "magical numbers" with shell closures is to take the spin-orbit-interaction into account. This is the interaction between the orbital angular momentum and the spin of the nucleons, which results in a new quantum number j, the total angular momentum. This quantum number describes the splitting of spherical nuclei, which allows explaining the higher "magical numbers".[3,25,30] However, this is only an explanation for spherical nuclei thus to the assumption of a spherical harmonic oscillator. The Nilsson model takes deformation of the nuclei into account by adding an additional quantum number Ω and therefore describes non-spherical nuclei too.[3]

2.1.3 Superheavy elements

According to the LDM superheavy elements should not exist. Looking at equation (2.2) it is obvious that a nucleus is only stable against spontaneous fission if the short-range, attractive nuclear force compensates the long-range, repulsive Coulomb force.[3] To describe the stability against spontaneous fission for a certain element the fissility parameter X is used, which describes the ratio between the Coulomb energy and the surface energy (see equation (2.1)).[6,32] The fissility parameter increases with the proton number. At the same time the determined half-live of the elements against spontaneous fission rapidly decreases for the actinides in this model. With rutherfordium (Z=104) a half-live of $t_{1/2} = 10^{-14}$ s is reached (see figure 2.2), which is the time that is needed to form an electron shell around a nucleus. Therefore, only nuclei with a half-life longer than this 10^{-14} s are considered as elements.[6,11,15]

Superheavy elements (SHE) exist solely due to stabilizing nuclear shell effects. These shell effects increase the spontaneous fission barrier to such an extent that, for many SHE, alpha decay becomes the faster and thus dominant decay mode.[3,6,7,15,33]

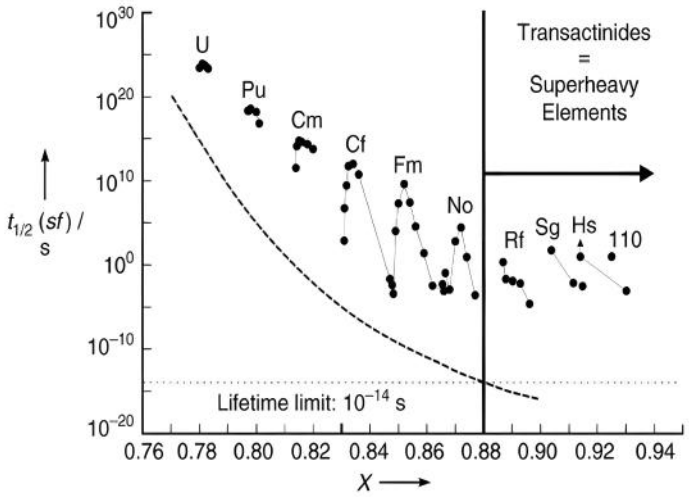

Figure 2.2: Known spontaneous fission (sf) half-lives ($t_{1/2}$) of nuclides with even numbers of protons and neutrons (dots) and calculated hypothetical half-lives (dashed line) based on the liquid drop model plotted against the fissility parameter X. The dotted line shows the limit of 10^{-14} s for the half-live of a chemical element. Taken from [6]. Reprinted with permission from John Wiley and Sons.

The NSM explains the increased stability of elements with certain shell configurations. Thus, it is possible to predict that certain elements with magic nucleon numbers, should be more stable than other proton-rich elements. The "island of stability" describes these, not found yet but more stable SHE.[6,9,15]
The predicted location of this "island" changed over the years. First predictions located the "island of stability" at a proton number of 126 and a neutron number of 184, which were changed to Z=114 and N=184 as research progressed.[7,34,35] More modern Hartree-Fock-type calculations confirmed the neutron number of 184 and assume a proton number of Z=114, 120 or 126.[7,36] All of these calculations were done for a spherical nucleus, but it is known today that the nuclei of superheavy elements are deformed, because of their quadrupole moment. A change in the shape of the nucleus also changes the position of neutrons and protons, which leads to further shell closures of these deformed nuclei. This results in more "magical" numbers at Z=108 and N=162, so to speak a "sub island" that connects the known parts of the periodic table with "the island of stability".[7,8] Today, the exact location of "the island of stability" is still in doubt as well as the predicted lifetimes for possible new elements with the calculated magical shell numbers, mainly because of alpha-decay in the region of the "island".[9,37]

2.2 Production of superheavy elements

The production of superheavy elements in a reactor via neutron capture and subsequent β^--decay is not possible. The most proton rich element that can be synthesized with this method is fermium, because there is no known fermium isotope that is unstable against β^--decay.[3,6,11]
Thus, every transfermium element has to be produced by heavy ion fusion reactions in accelerators.[6,8,11] Ions of a specific isotope are accelerated in these facilities and directed at a target nucleus with the intention of fusing both nuclei.[3,6,33,38]

The so called Q-value reveals whether a nuclear reaction is endothermic or exothermic. It is the rest-mass energy difference between the reacting nuclei and the product nuclei. A positive Q-value means the reaction is exothermic, a negative Q-value means it is endothermic. Heavy-ion nuclear fusions are endothermic reactions, which means the ions directed at the target have to have at least this energy to make a fusion possible.[3,38] But not only the Q-value has to be compensated, the repulsive, Coulomb force between the nuclei has to be overcome by the kinetic energy of the accelerated ion. If the kinetic energy is too low to overcome the Coulomb barrier, the nuclei cannot touch each other and therefore cannot fuse; instead, scattering reactions occur.[3,6,38,39]
The nuclear fusion process starts when the two nucleons get so close that the attractive nuclear force between both nucleons forms a dinuclear system. In this system, nucleons can be exchanged between the nuclei.[23,33,38] The nucleus formed after complete fusion of both nuclei is called compound nucleus (CN). The CN is an intermediate state containing the sum of all nucleons of the two initial nuclei.[6,14,38,40]
In the case of quasi-fission, the system decays through fission before the CN is formed completely.[3,38] The CN has a certain excitation energy, that depends on the selected reaction and beam energy.[14] There are two ways in which the CN can release its excitation energy: by spontaneous fission or by evaporation of neutrons. The competition between these two different processes is won by the faster process, which in the vast majority of cases is fission. This results in the forming of new nuclei from the compound nucleus (CN).[3,14] However, in a few cases the de-excitation takes place via the evaporation of neutrons. As neutrons are not electrically charged, they do not have to overcome a coulomb barrier in order to leave the nucleus. The evaporation of one neutron releases around 10 MeV (8 MeV of binding energy and 2 MeV of kinetic energy). After the evaporation of as many neutrons as needed to lose the excitation energy, the so called evaporation residue (EVR) is formed, which is the product of the fusion-evaporation reaction and the desired SHE.[6,14,41] The higher the excitation energy of the CN, the more neutrons need to be evaporated to release this energy, a fact that reduces the likelihood of the nucleus surviving.[14]

To achieve high cross-sections, two different approaches can be used. The first, called cold fusion, aims to form a CN with the lowest excitation energy possible, typically in the range of 10–20 MeV. This results in fewer neutrons needing to be evaporated from the CN, leading to a higher survival rate of the nucleus against fission. In this approach, targets typically made of lead or bismuth are used in

combination with heavier isotopes for the beam.[3,6,14,15] The main disadvantage of this approach is the higher coulomb barrier that has to be overcome in the fusion process, caused by a correlation between the product of the atomic numbers of target and beam and the height of the coulomb barrier. The second approach is the so called hot fusion. Lighter isotopes are chosen for the beam, while heavier (actinide) targets are used. This higher asymmetry between the nucleon numbers of the fusion educts leads to a lower Coulomb barrier and consequently an easier fusion of the nuclei. On the negative side, higher excitation energies (40-50 MeV) are achieved, resulting in a lower survival rate of the nuclei against fission.[3,6,14,15]

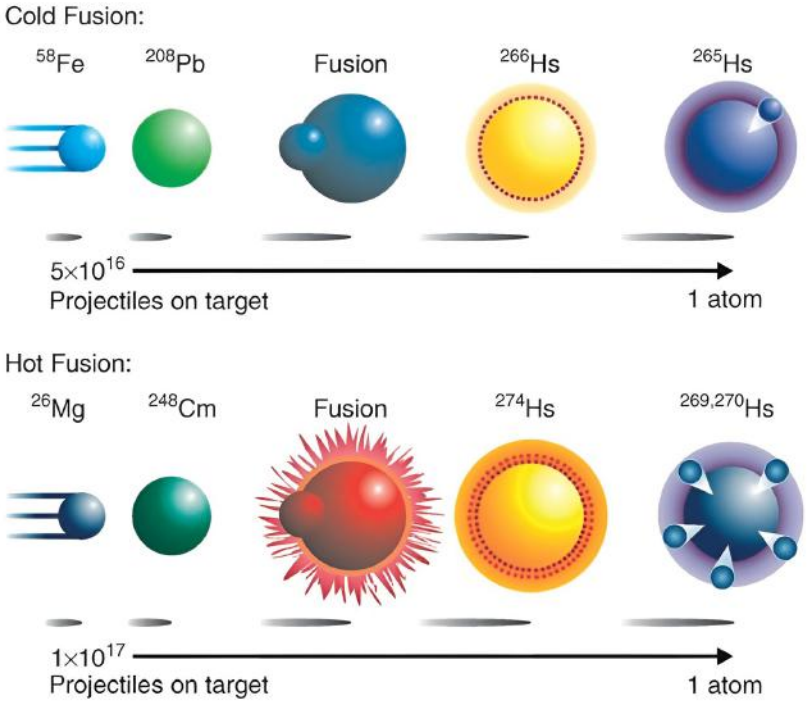

Figure 2.3: Schematic illustration of the ^{208}Pb(^{58}Fe, 1n)^{265}Hs reaction as an example for a cold-fusion reaction and ^{248}Cm(^{26}Mg, 4–5n)$^{269-270}$Hs for a hot-fusion reaction. Taken from[6]. Reprinted with permission from Wiley and Sons.

In general, the probability that the EVR is formed depends on three different factors, which are shown in equation (2.3).[14]

$$\sigma_{\mathrm{EVR}} = \sigma_{\mathrm{cap.}} \cdot p_{\mathrm{CN}} \cdot W_{\mathrm{sur.}} \tag{2.3}$$

Here σ_{EVR} is the cross section that the EVR is formed, $\sigma_{\mathrm{cap.}}$ is the capture cross section, p_{CN} is the fusion probability with which two captured nuclei transform into a compound nucleus and $W_{\mathrm{sur.}}$ is the probability for the CN to survive the evaporation process.[14] The effective cross section decreases exponentially with the atomic number. This was compensated by using the double "magical" nucleus ^{48}Ca as a projectile to discover the elements 113-118.[33,42]

2.3 Relativistic effects

As described previously, the periodic table provides a basis for predicting the chemical behaviour of elements based on their position. While this approach holds true for lighter elements, deviations from established periodic trends are observed for superheavy elements and their lighter homologues. These deviations arise primarily from relativistic effects, which become increasingly significant with higher atomic number, scaling with Z^2.[6,8] Relativistic effects dominate the chemistry of SHE and are essential to explain various properties of other heavy elements, such as the colour of gold, the preferred oxidation state +2 of lead, or the unusually low melting point of mercury.[17,18]

In the Bohr model, the attractive Coulomb force is balanced by the centrifugal force when an electron moves around the nucleus in a circular motion. This is described by equation (2.4)[14].

$$\frac{Z\,e^2}{4\,\pi\,\varepsilon_0\,r^2} \;=\; \frac{m_\mathrm{e}\,v^2}{r} \tag{2.4}$$

Here Z is the atomic number, e the elementary charge, ε_0 the dielectric constant, r the orbital radius, m_e the mass of the electron and v is the speed of the electron. If now the quantum condition $m_\mathrm{e} v r = n\hbar$ is inserted into equation (2.4) and the equation is solved for r, the following equation is obtained.[14]

$$r \;=\; n^2\,\frac{4\,\pi\,\varepsilon_0\,\hbar^2}{Z\,m_\mathrm{e}\,e^2} \tag{2.5}$$

From equation (2.5) it is clear that the radius of the circular motion of the electrons is a function of its mass. Einstein's theory of relativity says that the mass of an object is a function of its velocity. Following that, equation (2.6) shows the correlation between the velocity of an electron and its mass. Thus, there is a direct connection between the velocity of electrons and the radius of the circular motion around the nucleus.[14]

$$m_\mathrm{rel} \;=\; \frac{m_0}{\sqrt{1 \,-\, (v\,/\,c)^2}} \tag{2.6}$$

This results in the first relativistic effect, the direct relativistic effect. For higher proton numbers, the Coulomb force inside the atom gets stronger. To compensate for this effect, electrons move faster around the nucleus, which increases their mass and consequently decreases the radius of their circular motion.[6,14,43] As a result, orbitals with a significant electron probability density near the nucleus, such as the s- and $p_{1/2}$-orbitals, are contracted and energetically stabilized.[6,14,43]

Based on the direct relativistic effect, orbitals without electron density at the nucleus are better shielded from the nucleus because of the contracted orbitals. This leads to a weaker binding of the electrons and therefore an expansion of the radius of orbit. Following, these orbitals are energetically destabilized. This effect is called the indirect relativistic effect.[3,6,14,43]

The third and last relativistic effect, the spin-orbit coupling, splits the electron level of $l > 0$ (p, d, ... electrons) into $j = l \pm 1/2$ states. The SO splitting is much stronger for inner shells than outer shells with the same orbital quantum number l and decreases with increasing orbital quantum number for the same main quantum number n.[6,14]
All of the three described relativistic effects are in the same order of magnitude. Their influence scale with about Z^2.[6,7,14,17] This is why their influence is, especially for SHE, of great importance.[6,14,20]

2.4 Single-atom-chemistry and Monte Carlo simulation

2.4.1 Single-atom-chemistry and -chromatography

Short half-lives and low production rates of SHE allow no macroscopic studies of these elements. Instead, only individual atoms are available for investigation.[3,6,44] In this case, one of the most common equations in chemistry, the law of mass action, is no longer applicable to describe a single atom chemical reaction. The classical law of mass action describes the equilibrium of a chemical reaction with the chemical activity of both the educts and products.[45]Looking at only one atom at a time, it is not possible for this atom to be on both the product and educt side. This leads to a undefined equilibrium constant K. The same is true for the free enthalpy of the reaction.[3,46] To overcome this problem, it is possible to use the probability of the atom to be in the educt or product state to define K.[3] This makes chromatography studies of great interest for superheavy elements.[6,44] In chromatography, an atom or molecule frequently alternates between the mobile phase and adsorption on the stationary phase. This dynamic equilibrium provides insight into which state the particle is more likely to occupy under given conditions. Due to its rapid transport and separation capabilities, gas chromatography (gas as the mobile phase) is particularly well-suited for studies involving short-lived superheavy elements.[6,14,44,47] Especially fully automated chemical apparatus attached to separators like TASCA (TransActinide Separator and Chemistry Apparatus) at the GSI Helmholtzzentrum für Schwerionenforschung in Darmstadt, Germany, are very useful in this case, because here the elements are brought into the chromatography column directly after their production and separation.[48,49] A COMPACT (Cryo OnlineMultidetector for Physics And Chemistry of Transactinides) detector, consisting of two arrays of PIN diodes covered with a column material like SiO_2 or gold, works as the column and an α-detector at the same time and is often used at TASCA.[50]
Gas-solid chromatography relies on a series of adsorption-desorption processes on the column walls that atoms undergo as they travel through the column. The time every atom spends in a desorbed or adsorbed state depends for instance on the surface material, the adsorption enthalpy and the temperature. Assuming that the surface

of the column is smooth and homogeneous it is possible to describe the mean time an atom spends adsorbed on the wall with the so called Frenkel-equation.[44,51,52]

$$\bar{\tau} = \tau_0 \cdot \exp\left(\frac{-\Delta H_{\text{ads.}}}{R \cdot T}\right) \tag{2.7}$$

Here $\bar{\tau}$ is the lifetime of the species in the adsorbed state, τ_0 the period of oscillation of the species in the adsorbed state, $-\Delta H_{\text{ads.}}$ the adsorption enthalpy, R the molar gas constant and T the temperature.[44,51,52]

In principle, there are two ways for the species to be adsorbed to the surface. The first one, physisorption is based on Van der Waals bonding between the surface and the species.[3,53,54] Therefore, the strength of the bonding is dependent on the surface texture (a rougher surface equals a larger surface area), the distance between the bonding partners and the polarisation of the species. Due to the weak, non-covalent nature of the interaction, physisorption is relatively weak, with adsorption enthalpies typically below 50 kJ/mol. The process is fully reversible via desorption.[51,54–56] The second type of adsorption, chemisorption, often requires overcoming an activation energy (see figure 2.4a). Chemisorption involves the formation of a chemical (often covalent) bond between the surface and the adsorbed species. This process can be accompanied by changes in the coordination number, the breaking and formation of bonds, and alterations in the oxidation state. Chemisorption has a significantly higher adsorption enthalpy than physisorption and, in contrast to physisorption, is not always reversible. A desorbed species from this process might be chemically different from the adsorbed one.[51–57]

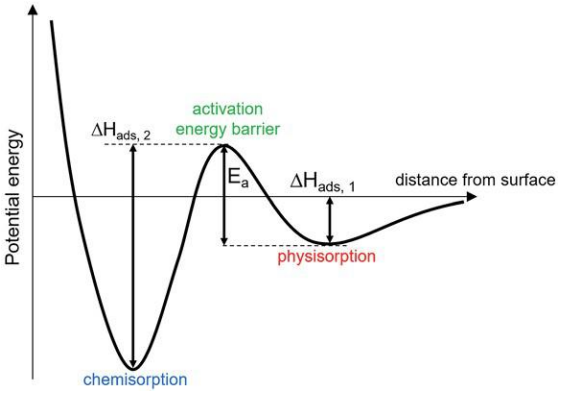

(a) Schematic one-dimensional diagram of the potential energy of an atom near the surface. The model assumes that a barrier from the physisorption can be overcome to form a stronger chemisorption. Taken from[52] (open access).

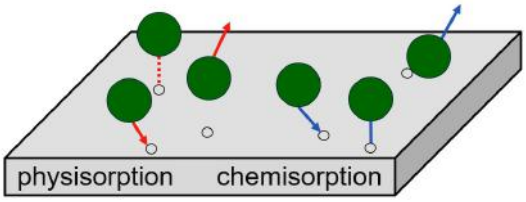

(b) Schematic of physisorption and chemisorption. For physisorption weak van der Waal bonds (red) between the surface (grey) and the species (green) lead to the adsorption of the species to the surface. In the case of chemisorption stronger, chemical bonds (blue) are formed between the species and the surface. These can exist even after desorption.

There are two widely used chromatographic techniques: isothermal chromatography (IC) and thermochromatography (TC). Both are based on these adsorption and desorption processes, and can be performed on different surfaces like gold or quartz glass.[6,7,14,51] In isothermal chromatography, the inert mobile phase flows through the column at a constant temperature. Depending on this temperature and

the adsorption enthalpy of the isotope, a certain fraction of the inserted atoms is adsorbed long enough to decay inside the column. By repeating the experiment at several temperatures and measuring the fraction of atoms passing through the column (the so-called breakthrough), an integrated chromatogram can be obtained. At a breakthrough of exactly 50%, the retention time equals the half-life of the isotope. From the retention time and the corresponding temperature, the adsorption enthalpy of the species can be calculated. [6,7,13,14,53]
In contrast, thermochromatography involves applying a temperature gradient, typically negative, along the column. When the species reaches the temperature corresponding to its adsorption energy, it is adsorbed onto the surface and remains there until it decays. From the position of the measured radiation inside the column, the adsorption temperature of the species can be determined, which in turn allows for the calculation of the adsorption enthalpy. [6,7,13,14,53] Figure 2.5 illustrates the yield as a function of temperature for both isothermal chromatography and thermochromatography.

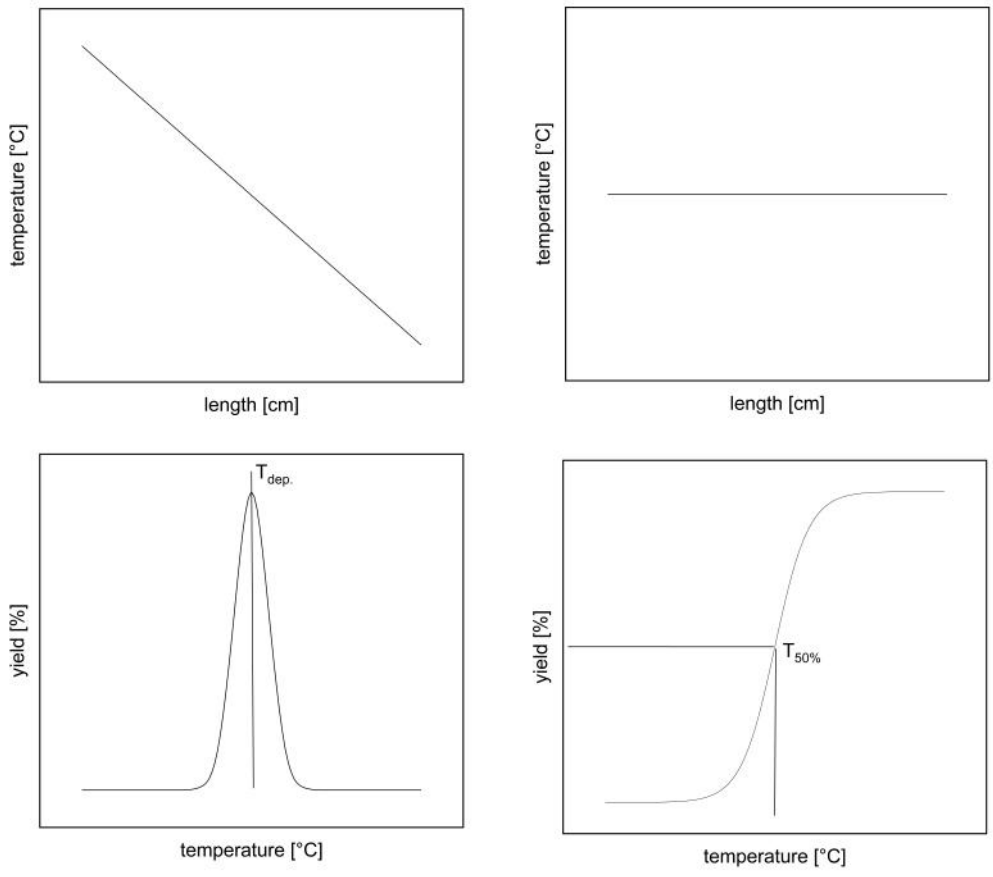

Figure 2.5: Comparison of thermochromatography (left) and isothermal chromatography (right). The deposition temperature (TC) and the temperature corresponding to 50 % breakthrough (IC) are indicated. Modified from [7].

2.4.2 Monte Carlo simulation

To calculate the adsorption enthalpy from the experimentally determined adsorption temperature, a Monte Carlo simulation can be done.[3,7] Monte Carlo simulations are used in all kinds of fields.[58] The method assumes that the behaviour of an ensemble can be predicted by a large number of random samples. For the calculation of the adsorption enthalpy in chromatography experiments, the Monte Carlo simulation developed by Zvára is used.[59] In this method, experimental parameters, such as the temperature gradient or the composition of the mobile phase, are used as input values for the simulation. Other parameters, such as the adsorption time on the surface or the lifetime, are chosen randomly during the simulation based on a defined distribution.[58–60] The adsorption enthalpy is defined as an input parameter and is varied until the simulation achieves the highest level of agreement with the experimental data.[51,53,59]

The process of the Monte Carlo simulation is best described by following one simulated atom through the chromatography column. At the beginning of the simulation, each simulated particle is assigned a random lifetime based on the exponential distribution of the half-life of the radionuclide. In offline experiments, the deposition pattern of the activity is measured after the experiment. Thus, only particles whose lifetime correspond to at least the experiment time can be measured. Therefore, for offline experiments, it is assumed that the lifetime equals the experiment time.[51,53,59] The simulated particle starts at the beginning of the column, position x_0. In the next step, a 'jump' is simulated, in which the particle travels a random distance based on an exponential distribution. This distribution is derived from the average jump distance, which is calculated using various experimental parameters, like the temperature or the gas flow rate. It is assumed that the particle is always adsorbed when hitting the surface after the travelled jump length.[51,59] The position of the simulated particle in the column is updated to x_i and the time the particle spent in the gas phase (flight time) is calculated from experimental parameters like the gas flow rate and the temperature. The atom is in an adsorbed state for a random timespan, based on the mean adsorption time (see equation 2.7). After the random adsorption time has passed, the atom is desorbed again. A freshly desorbed particle near the surface is very likely to collide with the surface wall again, leading to adsorption. Thus, the number of mean collisions with the surface after initial adsorption prolong the time of a full adsorption cycle. After the desorption of the atom, the calculated adsorption time is added to the flight time. This total time is compared to the previously allocated lifetime. If the lifetime has already elapsed, the simulation for this particle is terminated and its position in the column is recorded.[51,59] Otherwise, the next jump is simulated. The position is updated once more, and the adsorption cycle restarts until the combined flight and adsorption times reach the lifetime of the simulated particle or the particle reaches the end of the column. To obtain a dataset comparable to the experimental values, at least 5000 particles are simulated.[51,59] Figure 2.6a shows the flowchart for the described Monte Carlo simulation process.

However, the Monte Carlo simulation makes some assumptions that should be viewed critically. As it was already described before, the method assumes that every time a particle hits the surface, it is adsorbed, which does not necessarily have to be the case. Instead, the probability of adsorption is determined by the sticking coefficient. In addition, the Monte Carlo simulation does not differentiate between chemisorbed and physisorbed particles and the possibility to form a new species on the surface is not taken into account. These concerns were addressed by a Monte Carlo simulation extension, published by Dietzel et al. in 2024.[52] The central assumption of this extension is that a physisiorbed particle can become a chemisorbed species by overcoming an energy barrier (see figure 2.4a). By calculating the probability of overcoming this barrier, it is possible to simulate the adsorption enthalpy of both the original species and the new species formed through surface reactions, as well as the height of the energy barrier for this reaction.[52] The flowchart of this extension is shown in figure 2.6b.

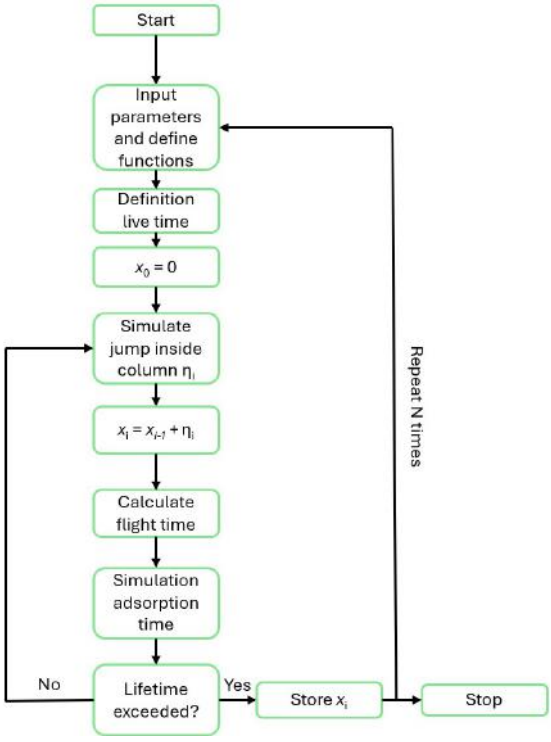

(a) Flowchart of the Monte Carlo method according to Zvara. Based on[59]

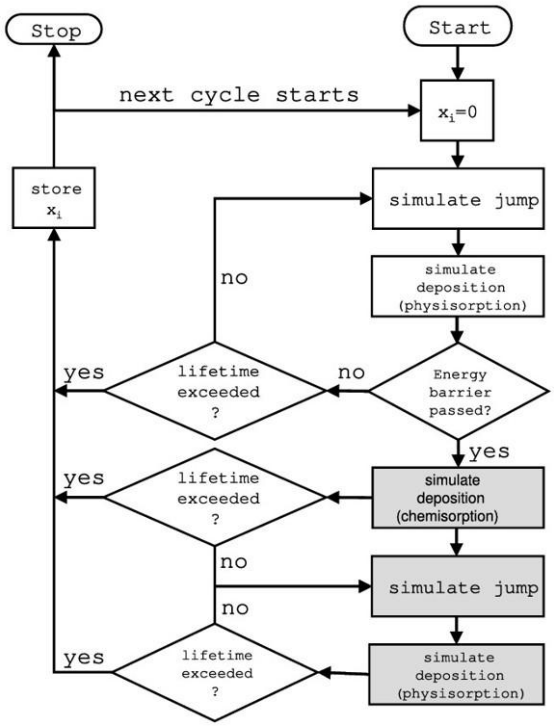

(b) Flowchart of the Monte Carlo extension method for considering the difference between chemisorption and physisorption. Taken from[52] (Open access).

2.5 The chemistry of thallium

Thallium is element 81 of the periodic table. The standard atomic mass is 204.38 u.[61] It was discovered by William Crookes in 1861 from seleniferous deposit of a sulphuric acid factory by observing a green spectral line at 535 nm. This line also gave it its name (from the greek word "thallos" meaning "green budding twig").[62–64]

Thallium has two stable isotopes, ^{203}Tl (29.52% nat. occurrence) and ^{205}Tl (70.48% nat. occurrence). ^{205}Tl is the end of the neptunium series decay chain. There are currently 41 known thallium isotopes, with ^{201}Tl as the only artificial isotope produced in higher amounts for nuclear imaging.[65–68] Thallium makes up a mass fraction in the earth's shell of about 0.29 ppm.[69]

Thallium is part of the group 13 elements (triels), the other ones being boron, aluminium, gallium, indium and nihonium. Consequently, thallium has the (non relativistic) electron configuration [Xe] $4f^{14}$ $5d^{10}$ $6s^2$ $6p^1$.[61,70] In its elemental form, it has a similar appearance to its neighbour element, lead.[68] From its position in the periodic table, it could be assumed that Tl(III) is the dominant oxidation state. However, due to the inert-pair effect, electrons in the 6s-orbital become an inert pair, lowering the dominant oxidation state to Tl(I).[4,65,68] Due to their charge and ionic radius, Tl(I)-ions are very similar to K-ions. Following that, these Tl(I)-ions can enter living cells and disturb enzymatic processes in the cell. Thallium is highly toxic in all of its forms, the lethal dose is between 8 and 15 mg/kg of body mass for the average human.[4,61,65,71]

2.5.1 Thallium hydroxides

The only known thallium hydroxide is TlOH. The pale yellow solid can be formed from the reaction of elemental thallium with water at room temperature. At 100 °C, the compound decomposes to Tl_2O (on a macroscopic scale). TlOH has a very similar chemical behaviour to KOH, it can act as a base and reacts with CO_2 to form Tl_2CO_3, which is the only known water soluble heavy metal carbonate.[68,72] The hypothetical $Tl(OH)_3$ or TlOOH do not exist or are unstable. Instead, $Tl_2O_3 \cdot 3\,H_2O$ and $Tl_2O_3 \cdot H_2O$ are known, which are thallium oxides because of their crystal structure.[68,72]

2.5.2 Thallium oxides

There are several known thallium oxides, the most common being Tl(I)- and Tl(III)-oxides.[68,72] α-Tl_2O_3 is the oxide of the Tl(III) oxidation state. The black solid crystallizes in the Ln_2O_3-C (Ln = lanthanide) structure and transforms into the Al_2O_3 structure under pressure at 600°C (β-Tl_2O_3). The melting point of α-Tl_2O_3 is 756°C. Heating the hydrated oxides produces the dehydrated form. This dehydration takes several hours. Heating the dehydrated oxide between 800°C and 1000°C reduces

the compound to Tl_2O, the oxide of the Tl(I) oxidation state.[68,72] Tl_2O crystallizes in the anti $CdCl_2$ structure, has a melting point of 596°C and a formation enthalpy of −179 kJ/mol. Thallium metal oxidises very fast to Tl_2O if exposed to air. This oxide can also be produced by heating up thallium monohydroxide to 100°C. Tl_2O is a black solid, hygroscopic and easily soluble in water.[68,72] A melt of Tl_2O is capable of damaging porcelain and glass by forming thallium silicate.[72]
The oxide of the Tl(II) oxidation state, TlO, is only stable in the gas phase or in a matrix.[68] The mixed oxide Tl_4O_3 ($(Tl)^{I}_{3}Tl^{III}O_3$) can be produced from a mixture of Tl_2CO_3 and Tl_2O_3.[68,72] The more uncommon thallium(I) hyperoxide, $Tl^{I}O_2$ is a violet solid that can be obtained by electrolysis of Tl_2SO_4 in oxalic acid-containing water at 20°C on a Pt-electrode. This oxide decomposes at 573°C.[68] Figure 2.7 shows an overview of the most common thallium species.

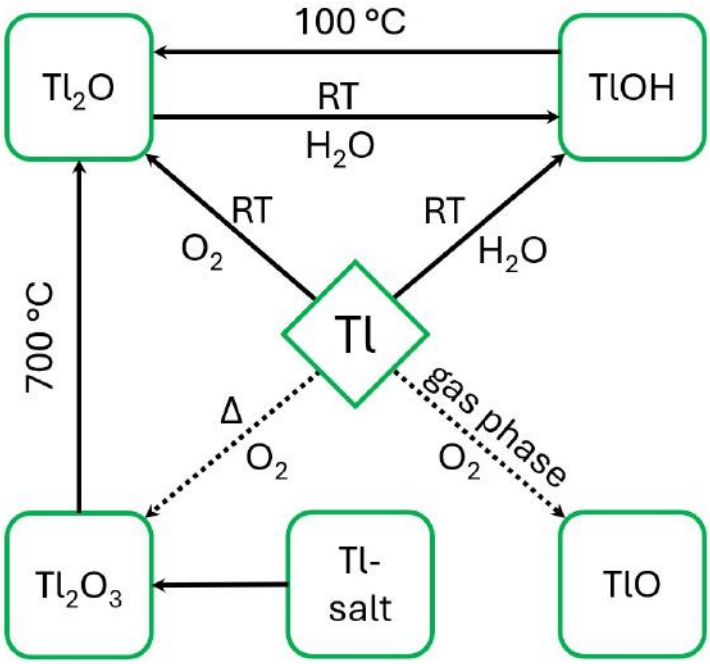

Figure 2.7: Overview of the most common thallium species and reactions

2.5.3 Previous single atom studies of thallium

Experiments to determine the volatility of thallium have been performed since the 1970s. B. Eichler found the adsorption enthalpy of carrier free thallium on SiO_2-glass to be (-112 ± 5) kJ/mol.[73,74] When experimental investigations of the chemical properties of nihonium were in preparation, the gas phase chemical behaviour of the lighter homologue thallium became the focus of attention again. Thus in 2013, A. Serov et al. conducted new experiments. They reported updated values for the adsorption on quartz glass and (for the first time) gold surfaces.[75] The authors used different reactive gases for their experiments on quartz glass and only found one species. Based on their results and experimental conditions, the authors suggested that OH groups were adsorbed onto the quartz columns used in the experiment,

where they reacted with thallium to form TlOH. Consequently, they attributed the determined adsorption enthalpy of (-134 ± 5) kJ/mol to TlOH.[75] Online isothermal vacuum chromatography measurements by P. Steinegger et al. yielded a value for the adsorption enthalpy of (-158 ± 3) kJ/mol for elemental thallium on quartz glass. Possible reactions of the metallic thallium with impurities and the quartz glass were precluded by the authors.[74] In 2018, L. Lens et al. showed new measurements with the COMPACT detector behind TASCA. In this article, no new adsorption enthalpy was reported; instead, a lower limit of 67 kJ/mol was published. However, the reported thallium deposition profile showed good agreement with the previous measurements by P. Steinegger et al.[76] In newer measurements performed by C. Gut et al. in 2023 two different thallium species with adsorption enthalpies of -90 kJ/mol and -140 kJ/mol were observed.[77] The authors did not clearly assign the values to specific species.[77] J. Wilson et al. presented the most recent results from both IC and TC measurements at the NRC10 conference in 2024. Several thallium species were observed, with adsorption enthalpies ranging from -96 kJ/mol to -202 kJ/mol. However, a definitive assignment of these species has not yet been made.[78] All experimentally determined adsorption enthalpies of thallium species on quartz glass are shown in table 2.1.

Table 2.1: Overview of experimentally determined adsorption enthalpies of thallium species on quartz glass, along with the corresponding chemical species.

species	ads. enthalpy [kJ/mol]	method	source
Tl	-112 ± 5	vac. chrom.	B. Eichler[73,74]
TlOH	-134 ± 5	gas chrom.	A. Serov[75]
Tl	-158 ± 3	vac. chrom.	P. Steinegger[74]
TlX	$-90, -140$	gas chrom.	C. Gut[77]
sev. species	$-96 - (-202)$	gas chrom.	J. Wilson[78]

Adsorption enthalpies were determined not only experimentally, but also through theoretical calculations. In 2016, V. Pershina performed calculations for the adsorption enthalpy of thallium atoms on quartz surfaces, resulting in a theoretical value of -150.2 kJ/mol.[79] This was in good agreement with the most recent experimental data at that time, reported by P. Steinegger et al. In 2022, new calculations were published by M. Ilias and V. Pershina. These updated studies distinguished between terminal, vicinal, and geminal OH groups on quartz surfaces (see chapter 2.6.1), thereby providing distinct adsorption enthalpies for differently hydroxylated surfaces (see table 2.2).[80]

Table 2.2: Overview of calculated adsorption enthalpies of thallium species on quartz glass, along with the corresponding chemical species. If different surface hydroxylation levels are considered, the predominant adsorption site is indicated as follows: [G] for geminal OH groups, [V] for vicinal OH groups, and [B] for bridged siloxane groups.

species	ads. enthalpy [kJ/mol]	method	source
Tl	-150.2	ADF BAND(1)	V. Pershina [79]
Tl	$-20.1[G], -44.2[V], -80.9[B]$	AMS BAND(1)	M. Ilias [80]
TlOH	$-133.1[G], -157.0[V], -324.5[B]$	AMS BAND(1)	M. Ilias [80]

(1): theoretical calculation method

2.6 Column surfaces

The most common column material for thermochromatography is SiO_2 or metallic surfaces like gold. In general, a suitable material should be non reactive to the gases used as mobile phase but show a certain reactivity with the atoms and molecules being investigated. [6,7,20,74,75] Knowing the exact composition of the surface used is crucial for ensuring better predictions and interpretations of the experimental results. Contaminations, cracks, and other impurities on the column surface can influence the experiment, leading to different adsorption enthalpies. [21,55]

2.6.1 Quartz glass

Quartz has the chemical formula SiO_2 and consist of a three-dimensional covalently bonded network of $(SiO_4)^{4-}$-tetrahedra [81,82] A distinction is made between crystalline quartz and quartz glass (vitreous silica). First, both quartz types share the same basic unit and the same O-Si-O bond angle (109.5°) inside the tetrahedral structure. However, the Si-O-Si bond angle and the rotational angle between adjacent tetrahedra differ. Crystalline quartz consists of a periodical network of the $(SiO_4)^{4-}$ tetrahedra with a defined unit cell. For vitreous silica, there is no such defined unit cell. Instead, the three-dimensional network is more 'random' than in the crystalline structure. This was first described by Zachariasen in 1932. [81–83] The differences between these structures is shown in figure 2.8.

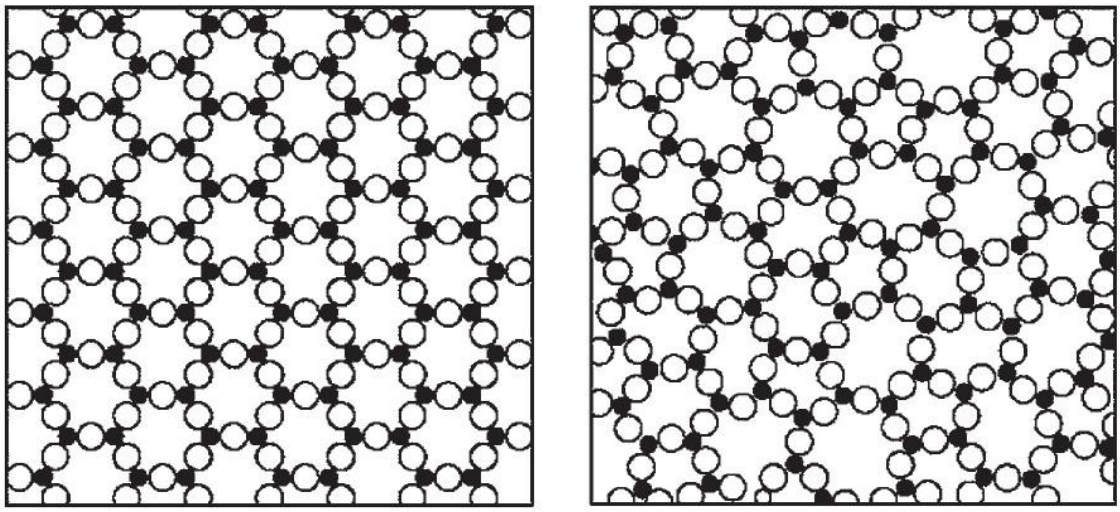

Figure 2.8: Schematic 2-dimensional comparison of the structure of crystalline (left) vs. non crystalline silica (right). Taken from [81]. Reprinted with permission from Springer Nature.

The primary functional groups of vitreous silica are siloxane (Si-O-Si bridge) and silanol groups (Si-OH).[51,79,84–86] The siloxane groups are largely inert (π-bonding), making them relatively irrelevant for determining the reactivity of the silica surface.[87] Silanol groups exist in several modifications with different stabilities (shown in figure 2.9), depending on the temperature and humidity. Terminal silanol groups are isolated OH-groups on the surface, while vicinal silanol groups are so close to each other, that there can be a hydrogen bond between the two OH-groups. Geminal silanols are structures with two OH-groups attached to one surface Si-atom.[51,79,85]

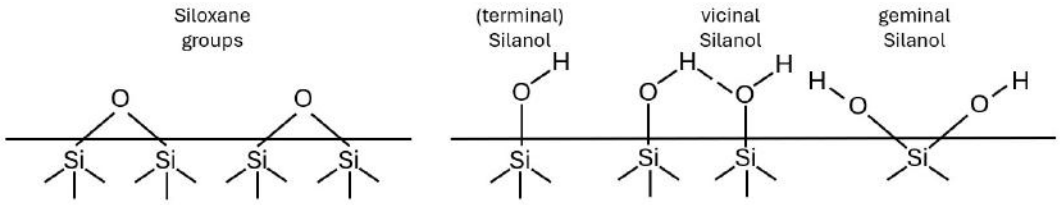

Figure 2.9: Siloxane groups (Si-O-Si) and various types of silanol groups (Si-OH) on the surface of vitreous silicas.

The initial silanol concentration on vitreous silica is dependent on the glass manufacturing method. Using a hydrogen-oxygen flame to melt the quartz granulate results in a higher silanol concentration on the surface, whereas electro-melting in a vacuum leads to a lower concentration.[84,88] It is possible to influence the silanol concentration on the surface of the quartz glass. Heating the glass to 1000 °C for several hours in a vacuum leads to the silanol groups splitting off water, resulting in a decrease of the silanol concentration.[79,84,88] Heating the quartz glass in the presence of water vapour or hydrogen increases the amount of silanol groups (hydroxylation), which also increases the reactivity of the surface.[88,89] These reactions allow controlling

the reactivity of the surface and thus make it possible to explain the results of the thermochromatography experiments.

2.6.2 Aluminium oxide

Aluminium oxide exists in seven different crystal structures, with α (corundum) and γ-Al_2O_3 being the most relevant. Under ultra-high vacuum conditions, the most stable surface termination of α-Al_2O_3 is the Al-terminated surface. The hydroxylation of α-Al_2O_3 is an exothermic process, meaning that corundum readily reacts with water to form $Al(OH)_3$ on its surface.[90–92] The kinetics of this reaction depend on various factors, including temperature and the amount of available water.[91–93] The resulting hydroxylated, oxygen-terminated surface exhibits reduced reactivity toward water due to surface saturation, but enhanced reactivity toward metals owing to the Lewis basicity of the hydrated layer. This hydroxylated surface is structurally similar to γ-$Al(OH)_3$.[90]

As with quartz glass surfaces, the number of surface O-H groups on aluminium oxide can be reduced by heating the material in an inert atmosphere. The dehydration process occurs in two steps: first, physically adsorbed water is removed from the $Al(OH)_3$ surface; second, chemically bound water is removed via breaking of O–H bonds. The remaining Al–O groups undergo coordination changes, forming oxygen bridges between aluminium atoms, analogous to siloxane bridges on quartz glass.[92] It remains unclear whether full dehydroxylation is achievable under experimental conditions.[92] The hydroxylation/dehydroxylation mechanism is illustrated in figure 2.10.

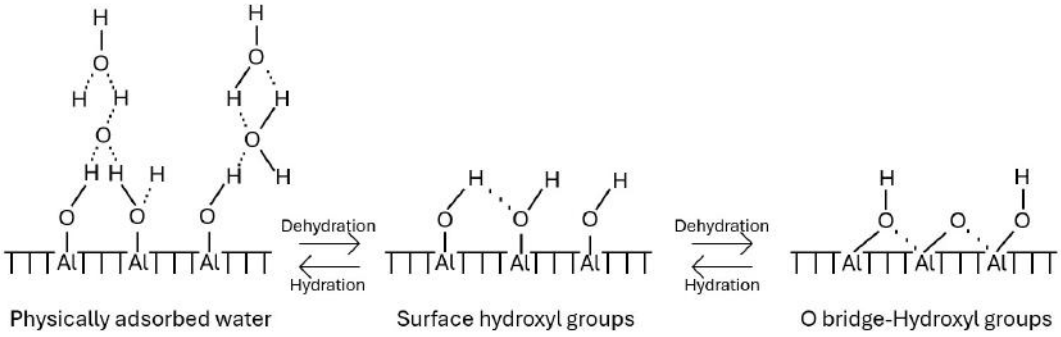

Figure 2.10: Hydroxylation/dehydroxylation process of a corundum surface. Taken from[92]. Reprinted with permission from Elsevier.

In the case of pure corundum with a single crystal modification, the hydroxylation and dehydroxylation processes are relatively straightforward. However, the columns used in this work are composed of sintered aluminium oxide, meaning that numerous Al_2O_3 crystallites are fused at high temperatures. This results in a broad spectrum of surface conditions. Consequently, the surface consists of different O-H group types, each involving varying coordination environments with surrounding aluminium atoms. These differing configurations require different temperatures for dehydroxylation.

This complicates the prediction of the required dehydroxylation temperature and the resulting degree of surface hydroxylation.[94,95]

2.6.3 Methods for surface examination

As described previously, surface composition is one of the key parameters in gas chromatography. Consequently, the analysis of the adsorbed species on the quartz glass surface is of high importance.
A widely used technique for surface characterization is X-ray photoelectron spectroscopy (XPS). This method utilizes the photoelectric effect to determine the characteristic binding energies of photoelectrons from specific elements, enabling the identification of the sample's composition.[96] However, XPS has certain limitations: it cannot detect hydrogen atoms, and both siloxane and silanol groups exhibit very similar binding energies, making their distinction challenging. Additionally, quartz is a non-conductive material, which leads to charging effects during XPS measurements, further complicating the analysis. Consequently, this method cannot directly determine the silanol concentration on quartz glass surfaces without additional effort.[97]
In contrast, infrared (IR) spectroscopy has been successfully applied for quartz glass characterization in the past, making it a promising alternative for surface analysis.[86,88,98]

IR spectroscopy is a well-established and widely used technique in chemistry. It is based on the absorption of infrared radiation by chemical bonds, causing them to vibrate. Different bonds absorb specific wavelengths, allowing qualitative analysis of molecules and materials. Additionally, quantitative analysis is possible using the Lambert-Beer law.[99–101] The most common IR technique, and the standard method for examining quartz glass, is transmission IR spectroscopy.[88,98] Here, an IR beam passes through the sample, with part of the light being absorbed. By comparing the emitted and detected light, precise information about the sample composition can be obtained.[86,88,101] However, this method provides information about the bulk composition of the sample rather than the surface properties.
An alternative approach is attenuated total reflectance IR spectroscopy (ATR-IR), where an ATR element enables total reflection of the incoming IR beam. A sample in close proximity to this ATR element interacts with the evanescent waves at the interface, allowing spectral analysis. However, ATR-IR spectra can only be directly compared to transmission spectra after additional, and often complex, data processing.[102,103]

A particularly promising technique for quartz surface analysis is reflection–absorption infrared spectroscopy (RAIRS). This highly sensitive optical method combines elements of both transmission and reflection IR spectroscopy.[104–106] Infrared radiation is directed onto the sample at a specific angle and interacts with adsorbed species, here, OH groups formed by the dissociative adsorption of water on the surface, before being reflected. The beam then passes through the adsorbed species again. Each time the beam interacts with the adsorbed species, specific wavelengths are absorbed by chemical bonds. After reflection, the beam is detected. Additionally, a portion of the

radiation is scattered rather than reflected, reducing the IR intensity that reaches the detector. Therefore, it is essential to position samples consistently at the same angle relative to the radiation source to ensure uniform scattering conditions.[101,104,106,107] Figure 2.11 illustrates the working principle of RAIRS.

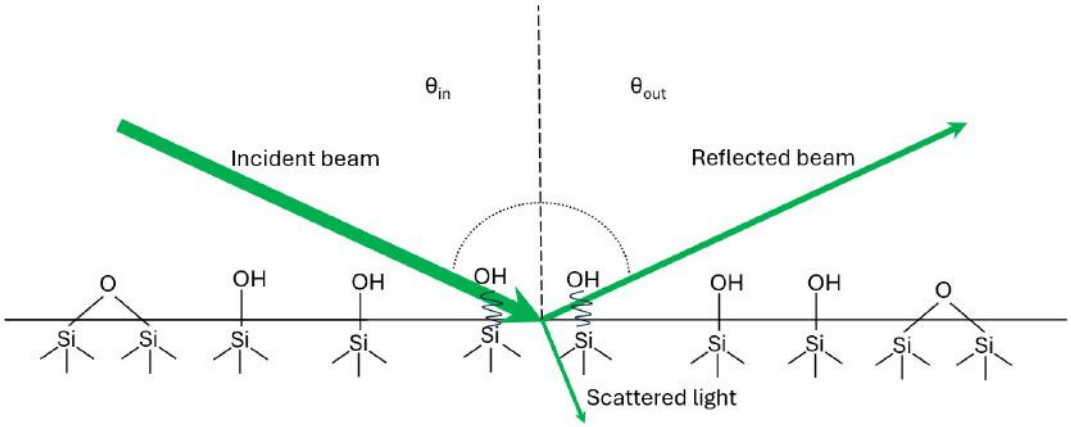

Figure 2.11: Principle of reflection–absorption infrared spectroscopy. The radiation passes through two adsorbed species. Si–OH bonds absorb radiation at specific wavelengths, while some radiation is scattered by the glass surface instead of being absorbed or reflected.

RAIRS offers several advantages over other spectroscopic methods. Since the IR beam is reflected, only species on the surface contribute to the detected signal (provided the beam reflects directly from the sample surface). Additionally, because the absorption of IR radiation is measured, the resulting spectra are more directly comparable to previously observed quartz glass transmission IR spectra.[88,104,106]

Chapter 3

Experimental and methods

To investigate the chemical behaviour of thallium on different surfaces, a series of preparative and analytical methods was employed. This chapter outlines the surface modification and characterization of quartz glass as well as the experimental procedures and evaluation methods used in the thermochromatographic studies of thallium.

3.1 Examination of quartz glass surfaces

3.1.1 Modification of quartz glass surfaces with (heavy) water

Quartz glass plates were modified and examined using RAIRS. The change in the OH-ratio on the surface of the plates allows for the validation of the applied modification methods. A total of five quartz glass plates were prepared, a reference sample, two samples modified at room temperature, and two samples prepared at high-temperatures.

These plates (quartz type: ilmasil® PN) were purchased from the manufacturer QSIL SE and cut to a size of 1 × 1 cm using a diamond saw. Two of these pieces were placed in two beakers each and submerged in either distilled water or D_2O (purity: 100 Atom% D). The beakers were covered with inverted, slightly larger beakers. Regular checks were conducted to ensure that the plates remained submerged; if necessary, liquid was refilled. After 13 days, the plates were removed from the liquids, carefully dried and subsequently examined using RAIRS (see chapter 3.1.2).

The following setup was used for high-temperature modifying of quartz glass surfaces.

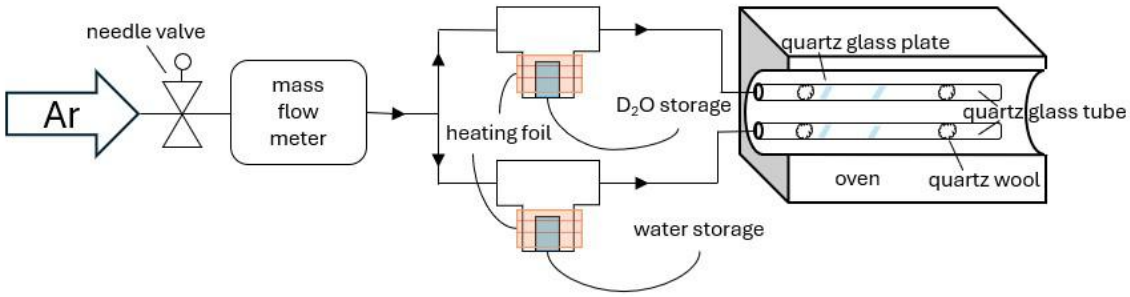

Figure 3.1: Schematic of the setup used for hydroxylation at high temperatures of quartz glass plates. The water/D_2O storage was placed inside a T-shaped aluminium tube.

An argon gas bottle (purity: 99.999%) was connected to the setup via polytetrafluoroethylene-tubes (PTFE-tubes). A needle valve and a mass flow meter (Merck, Aalborg Digital Mass Flow Meter) controlled the argon gas flow rate. The inert gas flow was split into two T-shaped aluminium tubes, each containing a small beaker filled with either distilled water or D_2O. A heating foil (Thermo TECH; 24 V, 30 W) was wrapped around each T-shaped tube. By applying power to the foil, the tube was heated, causing the liquid inside the beaker to slowly evaporate. The resulting vapour was transported by the gas flow into two quartz glass tubes, which were placed inside a tubular furnace (CARBOLITE GERO, EST 12/300B). Inside each tube, two quartz glass plates were positioned. Potential impurities were adsorbed on a cold quartz wool pluck at the beginning of the quartz glass tube.

The experiment was conducted over 13 days. To initiate the hydroxylation process, the oven was heated to 1000°C and a gas flow rate of 60–70 ml/min was set. A power supply was used to heat the foils up to 50-60 °C (H_2O: 16.0 V, 0.80 A; D_2O: 14.5 V, 0.68 A). The system was switched off overnight and on weekends, resulting in a total time at reaction temperature of 70 hours. Regular checks ensured that the beakers contained sufficient liquid at all times. After completion, the quartz plates were removed from the tubes and examined using RAIRS (see chapter 3.1.2).

3.1.2 Surface examination of the quartz plates using reflection-absorption infrared spectroscopy (RAIRS)

All RAIRS measurements were conducted at the Surface Science Laboratory at the Technical University Darmstadt. A Fourier-transform infrared-vacuum-spectrometer (Bruker Corporation,VERTEX 80) was used to measure the reflection-absorption infrared spectra of the pretreated quartz glass plates (see chapter 3.1.1). In addition, an untreated quartz glass plate was measured as well. The obtained spectra are difference spectra between the untreated and treated samples. Accordingly, the observed changes in intensity reflect differences in surface hydroxylation resulting from the treatment. Table 3.1 shows the parameters used for the measurement.

Table 3.1: Parameters of the RAIRS measurements of the quartz glass plates.

Parameter	Value
reflection angle	83 °
pressure	2.4 mbar
number of scans	1000

3.2 Thermochromatographic studies of thallium

3.2.1 Pre-treatment of the chromatography columns

Several chromatography columns (quartz glass and aluminium oxide) were pre-treated in preparation for gas chromatography experiments. Quartz glass columns were purchased from QSIL SE (outer diameter: (6.0 ± 0.2) mm, inner diameter: (4.0 ± 0.2) mm, length: (1000 ± 1) mm), while the alpha-aluminium oxide columns were manufactured by Kyocera (DEGUSSIT AL23; diameter: (6.0 ± 0.3) mm, length: (1000 ± 10) mm).

The following setup was used for dehydroxylation of the quartz glass tubes:

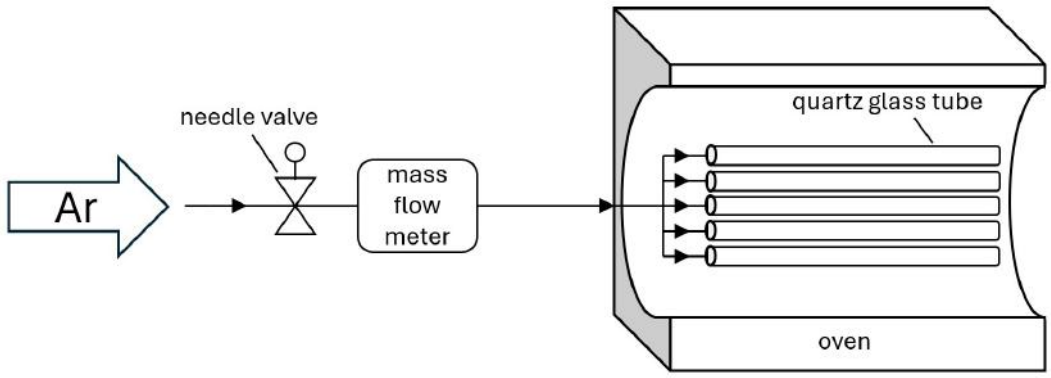

Figure 3.2: Schematic of the setup used for dehydroxylation of quartz glass columns. The oven used a built-in temperature sensor.

The argon flow was regulated using a needle valve and a mass flow meter before the gas is directed straight into the columns for dehydroxylation. Up to five quartz glass columns could be treated simultaneously. The columns were connected to the PTFE tubes using push-in fittings made of polybutylene terephthalate. All columns were placed inside a tubular furnace (THERMCONCEPT, ROS 105/900/12).

Similarly to the pretreatment of the quartz glass plates (see chapter 3.1.1), the experiment was conducted over several days. The gas flow rate was set to 60–70 sccm/min. The temperature was maintained for 5 hours per day, after which the oven was gradually cooled down over several hours. To prevent unwanted hydroxylation during cooling, the gas flow was never fully stopped and was set to 35 sccm/min overnight. After 20 hours at 1000 °C, the treated quartz columns were exchanged.

The alpha-aluminium oxide columns were baked out for 10 hours using the same setup. Instead of the push-in fittings, BOLA PTFE screw-in tube fittings had to be used to connect the aluminium oxide columns to the teflon tubes due to a slightly greater wall thickness.

3.2.2 Thermochromatographic studies

The same setup was used for all thermochromatography experiments. It consisted of a gas purification system followed by multiple ovens holding the chromatography column. Behind the ovens, the column was water-cooled to establish a temperature gradient along the column. A charcoal filter was placed at the end of the column to prevent radioactive particles from entering the gas exhaust. A schematic of the setup is shown in figure 3.3.

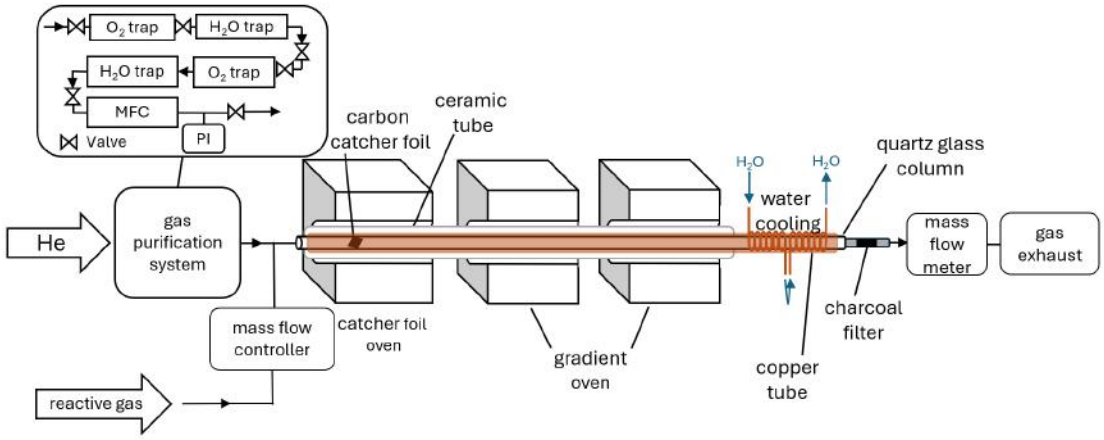

Figure 3.3: Schematic of the thermochromatography setup used for examining the adsorption enthalpy of different thallium species. This system includes various cartridges for gas purification, a mass flow controller (MFC) and a pressure indicator (PI).

Gas was transported to the experiment using PTFE or stainless steel capillaries. The connections were made with either push-in fittings composed of polybutylene terephthalate, Swagelok compression fittings made of stainless steel or BOLA PTFE screw-in tube fittings in the case of Al_2O_3. Helium (Linde, purity $\geq 99.9999\%$) was used as the carrier gas for all experiments. The gas purification system consisted of several cartridges designed to remove water and oxygen impurities. These cartridges were all made by Agilent Technologies and were a Spectromol Oxysorb ($H_2O <$ 30 ppb and $O_2 < 5$ ppb), a Spectromol Hydrosorb ($H_2O < 20$ ppb), a Big Moisture Trap, Model BMT-4 ($H_2O < 5$ ppb) and a Big Oxygen Trap, Model BMT-4 ($O_2 <$ 1 ppb). To control the gas flow of both helium and the reactive gas, two mass flow controllers (MKS, 1179AX; 1179BX) were used, along with a digital power supply and readout unit (MKS, PR400B).

For all experiments, the pre-treated columns described in chapter 3.2.1 were used. To ensure a smooth temperature gradient, the columns were placed inside a long copper tube with high thermal conductivity. This copper tube was inserted into a

shorter ceramic tube, which improved the stability inside the ovens and prevented heat emission from the tubes. The setup contained a total of three ovens. The first oven was used for heating the catcher foil and releasing thallium from it (in the following called catcher foil oven). The other two ovens were used for generating the temperature gradient. All heating ovens were manufactured by Heraeus Hanau (type B/A 1.7/10) and had a maximum temperature range of 900–1200°C. The temperature of each oven was controlled by varying the applied voltage from the associated power supply (Elektro-Automatik, Power Supply EA-PS 2042-20 B). At the end of the copper tube, two connected copper tube coils with circulating water were used to cool both the copper tube and the chromatography column to room temperature. To trap any activity passing the entire column, an activated charcoal filter was placed at the column's exit. A mass flow meter (Merck, Aalborg Digital Mass Flow Meter) was installed just behind the filter. By comparing its readings with those of the mass flow controller, potential leaks in the system could be identified. Finally, the gas leaving the setup was vented into a fume hood.

All experiments were conducted at the cyclotron of ÚJF in Řež. A gold foil (^{197}Au, 1.6-3.0 mg/cm^2) was irradiated for several hours with a ^{3}He beam (48 MeV; beam current: 200-600 nA). Carbon catcher foils (thickness: 75 µm) were used to collect nuclear reaction products recoiling from the target. In alignment with the calculations performed with the software LISEcute++ and the experimental data from [108] (see appendix table 7.5), the primary thallium isotope produced was ^{195}Tl ($t_{1/2} = 1.16$ h), with a smaller fraction of ^{196}Tl/^{196m}Tl ($t(^{196}Tl)_{1/2} = 1.84$ h; $t(^{196m}Tl)_{1/2} = 1.41$ h).

In the following section, the procedures of the different experiments will be explained.

Determining the adsorption enthalpy of Tl in a pure helium atmosphere (Tl-He-300)

First, the ovens were switched on and heated by applying specific voltages to them (table 3.2).

Table 3.2: Voltages applied to the different ovens during the experiment Tl-He-300.

Oven	Applied voltage [V]
Catcher foil oven	18.0
Gradient oven 1	14.9
Gradient oven 2	11.0

As soon as the temperature inside the copper tube was stable ($T_{max} = (398 \pm 20)$°C), the carbon catcher foil was placed inside the pretreated quartz glass column (see chapter 3.2.1). The foil was inserted far enough into the tube outside the ovens to ensure that it would later be positioned precisely inside the catcher foil oven (12 cm from the tube's edge). The column was then connected to the PTFE tubes, and a helium flow of 100 sccm/min was selected using the mass flow controller. No reactive

gas was added to the mobile phase. After flushing for 10 minutes, the column was inserted into the copper tube until the catcher foil was positioned in the middle of the catcher foil oven, marking the start of the experiment. During the experiment, the gas flow was continuously monitored, fluctuating between 99 and 101 sccm/min.

After 90 minutes, the helium flow was switched off, and the column was removed from the ovens through the cold end. The column was sealed using NMR-tube caps and left to cool for a few minutes. It was then cut into sections of (4 ± 0.2) cm. The first 12 cm of the column, including the catcher foil, were kept separately. A HPGe detector (Ortec Detector GMX20P4-70), which had been energy-calibrated beforehand with a ^{152}Eu source, was used to measure γ spectra of the catcher foil after heating, the charcoal filter, and each column segment. All samples were placed in a 3D-printed sample holder to ensure consistend measurement geometry. While the γ spectra were being recorded, a second quartz glass column was placed inside the ovens. After the establishment of the temperature gradient, a 1 m long thermocouple (type K) attached to a readout unit (Omega, HH801B) was used to measure the temperature gradient every 2 or 4 cm depending on the steepness of the gradient inside the column.

Determining the adsorption enthalpy of Tl in a pure helium atmosphere with a higher starting temperature (Tl-He-700)

The procedure for this experiment was nearly identical to the previous one. However, a temperature gradient starting at a higher temperature was chosen ($T_{\max} = (643 \pm 40)$°C). The voltages applied to the ovens are shown in table 3.3.

Table 3.3: Voltages applied to the different ovens during the experiment Tl-He-700.

Oven	Applied voltage [V]
Catcher foil oven	28.6
Gradient oven 1	21.0
Gradient oven 2	14.4

The catcher foil was inserted into a new, pretreated quartz glass column. After flushing with helium, the column was also placed inside the ovens. The experiment runtime was reduced to 60 minutes, with the gas flow fluctuating between 99 and 100 sccm/min.

After the experiment was completed, the column was treated and measured as described before. Additionally, sections that showed significant thallium deposition on their surfaces were further divided in half and measured again with the HPGe detector.

Determining the adsorption enthalpy of Tl in a helium and oxygen atmosphere (Tl-O2-700)

The applied voltages and therefore the temperature gradient for this experiment remained unchanged compared to the experiment Tl-He-700. The catcher foil was placed inside a new pretreated quartz column, and the PTFE tubes were attached. The mobile phase consisted of a gas mixture of 80 sccm/min helium and 20 sccm/min oxygen (Linde, purity $\geq$ 99.995%). The experiment runtime was again 60 minutes, with the gas flow fluctuating between 102 and 109 sccm/min.

After the experiment, the column was cut into sections and analysed using the HPGe detector. The temperature gradient was determined using the thermocouple and the readout unit.

Determining the adsorption enthalpy of Tl in a wet helium atmosphere (Tl-H2O-700)

For this experiment, the gas purification system was removed from the setup. Instead, a T-shaped tube equipped with a heating foil was installed between the mass flow controller and the column (see chapter 3.1.1). A beaker filled with distilled water was placed inside this tube. By applying a voltage of 16.0 V to the heating foil, the tube was heated to approximately 55 °C, causing the water to slowly evaporate and be transported by the helium flow (100 sccm/min) into the chromatography column. The applied voltages for the ovens were the same as in the previous experiments. The experiment runtime was 60 minutes. During the experiment, the gas flow fluctuated between 101 and 104 sccm/min.

After stopping the gas flow and removing the quartz glass column from the ovens, the measurement of the γ spectra and the determination of the temperature gradient were carried out in the same manner as in the previous experiments.

Determining the adsorption enthalpy of Tl in a pure helium atmosphere on aluminium oxide (Tl-He-700-Al2O3)

For this experiment, a pretreated α-Al_2O_3 column was used instead of a quartz glass column. To attach the column to the Teflon tubes, BOLA PTFE screw-in tube fittings were required, because of a slightly greater wall thickness of the α-Al_2O_3 columns. The rest of the setup, the mobile phase, and the applied voltages were identical to those used in experiment Tl-He-700. The experiment runtime was 90 minutes, with the gas flow fluctuating between 100 and 101 sccm/min.

Unlike the quartz glass columns, the ceramic column could not be cut. Instead, (2 ± 0.2) cm segments were marked on the outer surface. Using a lead block (wall thickness: around 7 cm (sides) and 1 cm (front)) with two round, opposing openings as a collimator and the HPGe detector, the entire column was then scanned segment by segment. During the measurement, the collimator shielded the whole column with an exception of a 2 cm opening in front of the detector, allowing to scan the

segments. The collimator was tested beforehand using an ^{152}Eu source, to make sure that the shielding, especially for lower energetic gamma rays, is adequate. To determine the temperature gradient, another α-Al_2O_3 column was placed inside the ovens before measuring the gradient with the thermocouple as described above.

Determination of the adsorption enthalpy of Tl in a pure oxygen atmosphere (Tl-pure-O2-700)

This experiment was conducted during an additional beamtime. The applied voltages remained unchanged, when compared to the previous measurements. The catcher foil was again placed inside a pretreated quartz column, and the PTFE tubes were connected. A flow of 100 sccm/min of oxygen (Linde, purity $\geq$ 99.995%) was set for the mobile phase. The experiment was carried out for 47 minutes, and the actual gas flow was measured to be around 150 sccm/min.

After the experiment, the column was once again cut into 4 cm long pieces, which were analysed using the HPGe detector. The temperature gradient was determined using a thermocouple connected to the readout unit.

3.2.3 Evaluation process

As described in the previous chapter, γ-spectra of the column pieces were recorded during the experiments. These spectra represent the number of detected γ-rays at specific energies. By comparing the measured spectra with literature values for energy and relative intensity, it is possible to identify isotopes based on their characteristic γ-ray emissions, thereby enabling an analysis of the samples isotope composition.

To prove that the desired isotopes were produced in the nuclear reaction as predicted by the calculations (see table 7.5), it would be beneficial to analyse the γ-spectrum of the catcher foil used in the experiment. However, it was not possible to record a spectrum of the catcher foil immediately after irradiation due to its high activity, which resulted in a measurement dead time exceeding 78 %. Instead, figure 3.4 presents the γ-spectrum of the column section located directly adjacent to the catcher foil from the Tl-He-700 experiment after the experiment.

A reliable method for element identification in the spectrum is the analysis of X-ray peaks, which appear as intense peaks at lower energies. Based on these X-ray peaks, it can be concluded that only ^{195}Tl and ^{196}Tl/^{196m}Tl were present in the analyzed column piece. The X-ray lines of ^{196}Tl/^{196m}Tl are so close to those of ^{195}Tl that they cannot be resolved in the full spectrum. This result agrees well with the theoretically calculated and experimentally determined isotope distribution (see table 7.5). Even the low-intensity ^{195}Tl peaks ($I_\gamma \approx 2\,\%$), are observed in the obtained γ-spectrum.[109]
In comparison to ^{195}Tl, ^{196}Tl/^{196m}Tl were produced in smaller quantities. Consequently, the lower-intensity γ-rays of this isotope were too weak to be distinguished from the spectral background.[110] Therefore, only the most intense peaks of

^{196}Tl/^{196m}Tl ($I_\gamma > 10\,\%$) are visible in the spectrum.

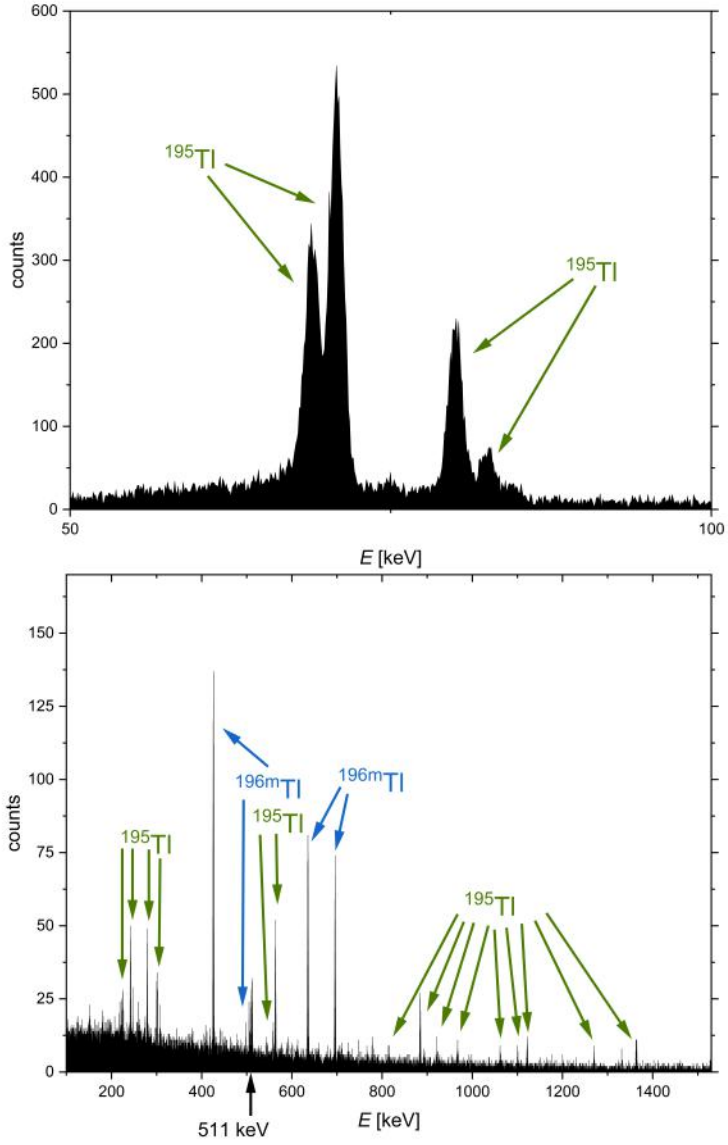

Figure 3.4: Determined γ-spectrum of the first four centimetres next to the catcher foil of the Tl-He-700 experiment. In the first spectrum, the X-ray section is shown. The second spectrum shows the rest of the spectrum. The most significant peaks are assigned to their corresponding isotopes. The characteristic annihilation peak at 511 keV is also visible.

Four distinct γ-ray lines (70 keV, 426 keV, 563 keV, and 884 keV) were analysed in all acquired spectra to obtain thermochromatograms. The peaks were fitted using a Gaussian function which was subsequently integrated. The integral included a constant baseline correction under the assumption that the baseline on both sides of the peak was of similar height. If this assumption was not valid, a manual baseline

correction was applied. In such cases, a previously determined linear baseline was subtracted from the peak before integration. An example of a Gaussian fit, including the determined baseline, is shown in figure 3.5, for the 884 keV ($I_\gamma = 10.6\,\%$) line from the spectrum in figure 3.4.

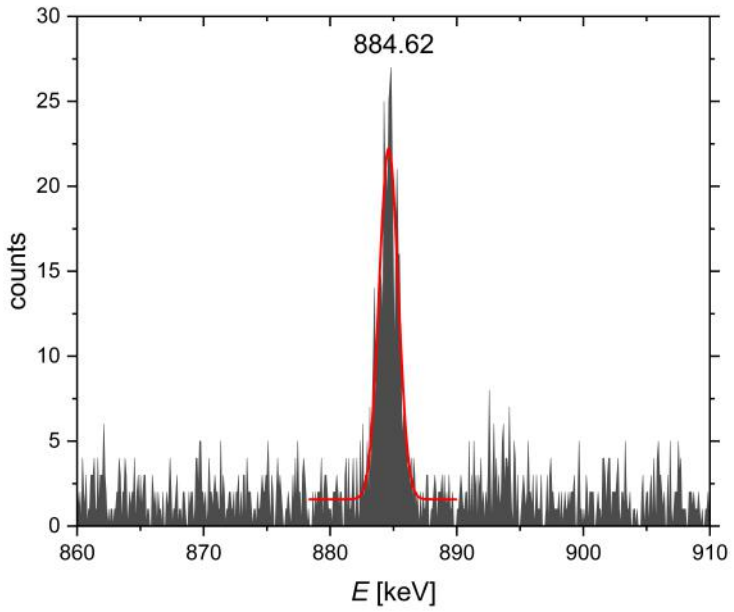

Figure 3.5: Gaussian fit of the 884 keV line of the γ-spectrum of the first four centimeters next to the catcher foil of the Tl-He-700 experiment.

Next, the obtained net peak areas, along with their respective uncertainties, were normalized to the measurement time in seconds (live time), yielding the count rate in counts per second (cps). Since the spectra were recorded over several hours, radioactive decay during this period had to be accounted for. To correct for that decay, the activities were extrapolated to the start time of the first measurement using the exponential decay law. The errors associated with the start and stop times were assumed to be negligible. Since all column segments were manually cut, an uncertainty of $\pm\,2$ mm in segment length was assumed. This uncertainty was added to the total error, leading to an approximate increase of 10% in the extrapolated activity uncertainty. To ensure that no γ lines of impurities overlapped with the γ lines of Tl, several lines were evaluated. Only if all these lines showed the same deposition distribution inside the column it was assumed that no significant nuclear impurities were present. As described in chapter 3.2.2, some column segments were divided in half if they exhibited significantly higher activity than adjacent sections. Consequently, in these cases, the examined segments were 2 cm long instead of the usual 4 cm. For a consistent evaluation, it was necessary to standardize all column pieces to the same length. It was assumed that the activity within a given segment was homogeneously distributed, allowing for a proportional division of both length and activity for all 4 cm pieces. This approach enabled direct comparison of activity

across all measured segments. For the Tl-He-300, Tl-He-700-Al2O3 and the Tl-pure-O2-700 experiments, the 426 keV line was used for comparison, because it was the strongest line in case of the first experiment, respectively the line that was collimated the best. For all other experiments the 884 keV line was used.
To determine the adsorption enthalpies of the deposited species inside the columns, Monte Carlo simulations following Zvára's approach were performed.[59] Multiple simulations were conducted, varying the adsorption enthalpy as a parameter. The simulation that best matches the shape of the thallium deposition provides the adsorption enthalpy. To choose the best fitting parameter, χ^2 was determined for all simulations. The C++ code used for the simulation was developed by Katharina Hermainski.[111] The input parameters for each experiment are provided in the respective chapters. The simulation was conducted only for the region between the catcher foil and the end of the column, as transport and deposition of thallium in the opposite direction were considered unlikely due to the prevailing gas flow.

Additional experimental parameters used in the Monte Carlo simulations were also subject to uncertainties, leading to variations in the determined adsorption enthalpy. To estimate the uncertainty of the adsorption enthalpy, input parameters were systematically varied within their respective error margins.
In the first step, the uncertainty of the gas flow rate Q was considered. According to the manufacturer, the mass flow meter used to measure the gas flow had an error of 1%. Adding this error to the observed fluctuations in gas flow during the experiments yielded the upper and lower bounds for each experiment.
In a subsequent simulation, the influence of pressure was examined. Although the system was assumed to be open to atmospheric pressure (1 bar), a possible increase in pressure due to the charcoal filter and Teflon capillaries was considered, leading to a maximum assumed pressure of 1.1 bar.
The residence time of thallium atoms inside the column was also investigated. The evaporation of thallium atoms results in a distribution of residence times, depending on when each atom is released. For the initial simulation, based on previous experiments with polonium, it was assumed that the catcher foil required five minutes to reach a sufficient temperature to release most of the thallium atoms. This assumption was based on the fact that the column, including the catcher foil, was inserted into a preheated oven, leading to rapid heating. Additionally, the total experiment duration was taken into account. The full runtime was chosen as the upper limit, while half of the runtime was considered the lower limit. These limits were set to account for a probable gradual decrease in the number of evaporated atoms during the runtime of the experiment
Another parameter subject to uncertainty was the inner radius of the columns. The manufacturer specified the inner diameter as (4±0.2) mm for the quartz glass columns. Consequently, the radius was assumed to be 2 mm, with an upper limit of 2.2 mm and a lower limit of 1.8 mm.

For conducting the Monte Carlo simulations, the temperature gradient of the experiment was required. The uncertainty of this gradient was estimated based on multiple factors. The given uncertainty for the thermocouple was ± 2 °C, and the error for

the readout unit was 0.05%. Thus, the overall uncertainty could not be smaller than the sum of these two values. However, a comparison of different measurements of the same temperature gradient (same oven currents/voltages) revealed larger deviations. Additionally, the position of the thermocouple inside the column was subject to uncertainties. In particular, small positioning errors had a significant impact in the hotter regions of the column, where the temperature gradient was steep. Consequently, an additional uncertainty was assumed for these areas. As a result, the total uncertainty ranged from $\pm 40\,°C$ in the hottest regions of the column to approximately $\pm 2\,°C$ at room temperature. Temperature gradients were measured at intervals of two centimetres and interpolated using the Akima spline method to obtain a continuous profile. The final temperature gradients are provided in the appendix (see tables 7.1 - 7.4).

The influence of all considered parameters on the adsorption enthalpy for each experiment is summarized in the respective chapters. Since it is not entirely certain which thallium species are present in the depositions and the molar mass of the species has only a minimal impact on the Monte Carlo simulation, the molar masses used in the simulation were based on the weights of the respective investigated isotopes.

Chapter 4

Results

4.1 Examining of quartz glass surfaces

As described in chapter 3.1.2, the surfaces of treated and untreated quartz glass plates were examined using RAIRS. To compare the resulting spectra of the five samples, the spectrum of the untreated quartz glass was used as a reference spectrum for the other samples. Figure 4.1 shows the respective differences of each spectrum from the reference spectrum.

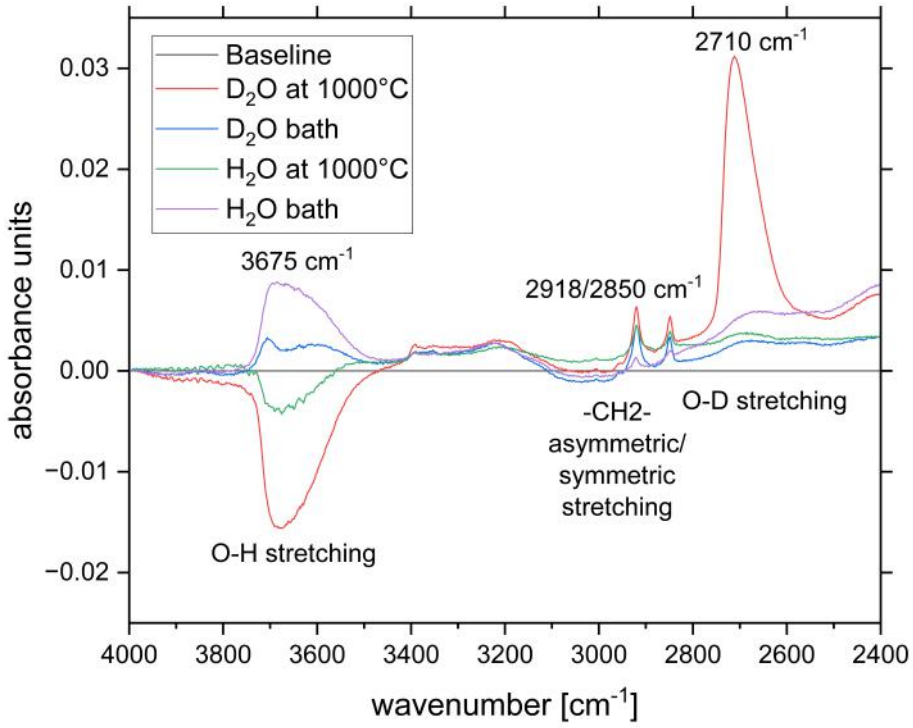

Figure 4.1: Differential spectra of the four treated quartz glass samples compared to the untreated sample as a reference. The most important peaks are labelled with their corresponding wavenumbers and assigned vibrations.

In the case of the sample treated with D_2O vapour at high temperatures, the intensity of the O-H stretching peak is considerably lower than in the reference spectrum, while the O-D stretching peak intensity is significantly increased. However, the surface of the glass sample treated with water vapour at high temperatures shows an decreased O-H stretching peak intensity. In addition, the background at the O-D stretching peak is slightly increased. This is observed in all of the remaining samples. The two samples treated at room temperature both show an increased O-H stretching peak intensity, with the one treated in the water bath exhibiting a stronger increase. Both the CH_2 asymmetric and symmetric stretching peaks are slightly increased in all samples.

4.2 Thermochromatographic studies of thallium

4.2.1 Determination of the adsorption enthalpy of thallium on quartz glass in a pure helium atmosphere

Thallium evaporation at 300 °C (Tl-He-300)

Thallium deposition was only observed in the column segment adjacent to the catcher foil. It was therefore decided that further evaluation of this experiment was not meaningful, as the measured activity was extremely low (0.055 ±0.003 counts/s for the 426 keV line). Compared to activities observed in other measurements, it was concluded that the temperature of the catcher foil oven was likely insufficient to evaporate a significant amount of thallium. Therefore, further evaluation is not meaningful. The corresponding histogram as well as the obtained activity per segment are shown in the appendix (see figures 7.1 and 7.2).

Thallium evaporation at 700 °C (Tl-He-700)

The activity of each column segment was determined as described in chapter 3.2.3. Compared to the previously discussed experiment, the activity measured here was several orders of magnitudes higher. Consequently, it was assumed that the evaporation of Tl atoms from the catcher foil was successful, allowing for further evaluation. The used input parameters for the Monte Carlo simulation is shown in table 4.1. Figure 4.2 shows the measured thallium depositions as well as the Monte Carlo simulation.

Table 4.1: Input parameters used for the Monte Carlo simulation to determine the adsorption enthalpy of Tl on a quartz glass column in pure helium. Here, M is the molar mass of Tl, F_{mp} the fraction of helium in the mobile phase, ρ the density at the boiling point, Q the gas flow rate, r the inner radius of the column, p the pressure inside the column, τ_0 the period of oscillation at the surface, T the temperature, and t_{exp} the experiment duration. It was assumed that the catcher foil required five minutes to heat up and evaporate thallium; therefore, the experiment duration assumed for the simulation was reduced by five minutes.

Input parameter	Value	Reference
M_{Tl}	195 g/mol	-
M_{He}	4 g/mol	-
F_{mp}	1	-
ρ_{Tl}	11.85 g/cm^3	[68]
ρ_{He}	0.125 g/cm^3	[112]
Q	100 sccm/min	-
r	2 mm	-
p	1 bar	-
τ_0	$0.2 \cdot 10^{-12}$ s^{-1}	[51]
T	see table 7.1	-
t_{exp}	3300 s	-

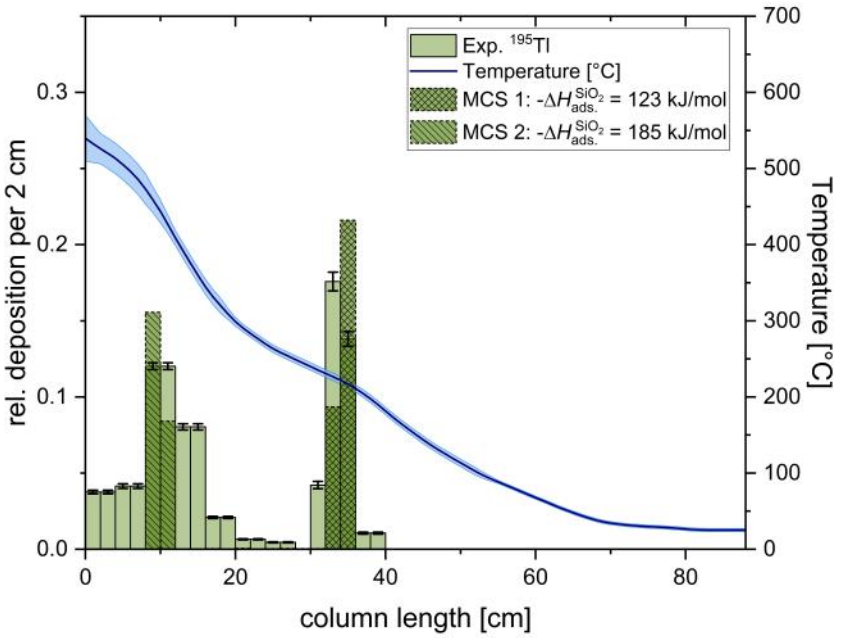

Figure 4.2: Thermochromatogram of Tl (884 keV line) on pretreated quartz glass columns in a pure helium atmosphere at an evaporation temperature of 700 °C. The measured deposition is represented by the light green bars, while the Monte Carlo simulation is illustrated by the darker green, striped bars. The temperature gradient is shown in blue. To improve comparability between the simulation and the experimental data, the simulated activity was scaled by the ratio of the activity of the corresponding experimental peak to the total experimental activity. 0 cm corresponds to position of catcher foil. No Tl was detected in the charcoal filter.

Two distinct deposition zones were observed in the column. A sharp deposition peak A was found at a column temperature of around 250 °C and has a relative intensity of around 40%. The broader deposition peak B shows a deposition temperature at its maximum height of around 460 °C and relative intensity of around 60%. Using the parameters listed in table 4.1, the best fit between simulation and experimental data was obtained for adsorption enthalpies of $-123\,\mathrm{kJ/mol}$ and $-185\,\mathrm{kJ/mol}$, respectively. It is noteworthy that, especially for peak B, the simulation does not fully reproduce the peak shape of the actual measured deposition.

Table 4.2 shows the used lower and upper limits of all considered input parameters as well as the corresponding influence on the adsorption enthalpy.

Table 4.2: Parameters varied in the simulation, their respective values, and the deviation from the with the most probable value determined adsorption enthalpy $\Delta(-\Delta H_{\mathrm{ads.}})$ for experiment Tl-He-700.

Parameter	Input value	$\Delta(-\Delta H_{\mathrm{ads};A})[\frac{\mathrm{kJ}}{\mathrm{mol}}]$	$\Delta(-\Delta H_{\mathrm{ads};B})[\frac{\mathrm{kJ}}{\mathrm{mol}}]$
Q_{low}	98 sccm/min	0	-1
Q_{high}	101 sccm/min	0	0
p_{high}	1.1 bar	0	-1
$t_{\mathrm{exp,low}}$	1800 s	-2	-4
$t_{\mathrm{exp,high}}$	3600 s	1	0
r_{low}	1.8 mm	1	1
r_{high}	2.2 mm	0	-2
T_{low}	see table 7.1	-3	-4
T_{high}	see table 7.1	3	5

To determine the overall uncertainty of the adsorption enthalpy, all individual deviations (table 4.2) were summed. The final adsorption enthalpies, including uncertainties, are:

$$-\Delta H_{\mathrm{ads};A} = 123^{+5}_{-5}\,\frac{\mathrm{kJ}}{\mathrm{mol}}$$

$$-\Delta H_{\mathrm{ads};B} = 185^{+5}_{-12}\,\frac{\mathrm{kJ}}{\mathrm{mol}}$$

4.2.2 Determination of the adsorption enthalpy of thallium on quartz glass in a helium and oxygen atmosphere (Tl-O2-700)

The evaluation of the γ spectra was performed as described for the previous measurements. The input parameters used for the Monte Carlo simulation are shown in table 4.3.

Table 4.3: Input parameters used for the Monte Carlo simulation to determine the adsorption enthalpy of Tl on a quartz glass column in a helium-oxygen atmosphere. Here, M is the molar mass of Tl, F_{mp} the fraction of helium in the mobile phase, ρ the density at the boiling point, Q the gas flow rate, r the inner radius of the column, p the pressure inside the column, τ_0 the period of oscillation at the surface, T the temperature, and t_{exp} the experiment duration. It was assumed that the catcher foil required five minutes to heat up and evaporate thallium; therefore, the experiment duration assumed for the simulation was reduced by five minutes.

Input parameter	Value	Reference
M_{Tl}	195 g/mol	-
M_{He}	4 g/mol	-
$M_{\mathrm{O_2}}$	32 g/mol	-
F_{mp}	0.8	-
ρ_{Tl}	11.85 g/cm^3	[68]
ρ_{He}	0.125 g/cm^3	[112]
$\rho_{\mathrm{O_2}}$	1.141 g/cm^3	[113]
Q	100 sccm/min	-
r	2 mm	-
p	1 bar	-
τ_0	$0.2 \cdot 10^{-12}$ s^{-1}	[51]
T	see table 7.1	-
t_{exp}	3300 s	-

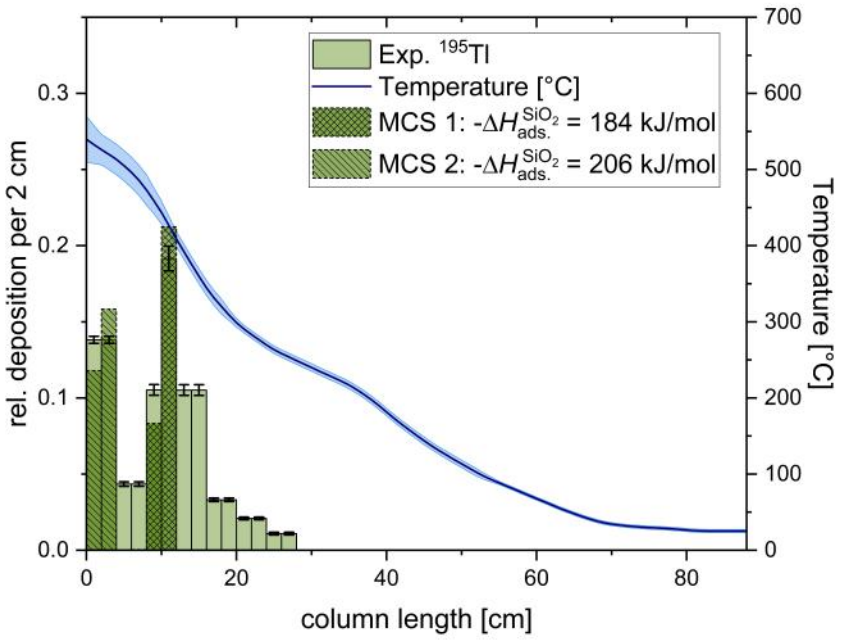

Figure 4.3: Thermochromatogram of Tl (884 keV line) on pretreated quartz glass columns in a helium-oxygen atmosphere. The measured deposition is represented by the light green bars, while the Monte Carlo simulation is illustrated by the darker green, striped bars. The temperature gradient is shown in blue. To improve comparability between the simulation and the experimental data, the simulated activity was scaled by the ratio of the activity of the corresponding experimental peak to the total experimental activity. 0 cm corresponds to position of catcher foil. No Tl was detected in the charcoal filter.

Two deposition zones were found in the column in this experiment as well. The broad deposition zone B at a column temperature of around 430 °C and a relative intensity of around 72% was assigned to an adsorption enthalpy of −184 kJ/mol. This species shows the same broad deposition form as the one with a similar adsorption enthalpy described in chapter 4.2.1. The second deposition zone C was detected at the very beginning of the column, next to the catcher foil at a column temperature of around 530 °C with a relative intensity of around 28%. An absolute value for the adsorption enthalpy cannot be given, as the deposition appears to be diffusion-controlled and might occur at higher temperatures if the column were initially hotter. Instead, the Monte Carlo simulation yields a limit for the adsorption enthalpy of $-\Delta H_{\text{ads.}} \geq 206$ kJ/mol.

The error of the adsorption enthalpies were determined as described in chapter 3.2.3. The flow fluctuated between 102 and 109 sccm/min. This slightly increased flow rate is caused by the calibration of the mass flow meter that was done with pure helium. Because oxygen has a higher mass, the mass flow meter overestimated the actual gas flow. To account for this increased uncertainty, the lower and upper limit of the gas flow was adjusted accordingly (see table 4.4).

Table 4.4: Parameters varied in the simulation, their respective values, and the deviation from the with the most probable value determined adsorption enthalpy $\Delta(-\Delta H_{\text{ads.}})$ for experiment Tl-O2-700.

Parameter	Input value	$\Delta(-\Delta H_{\text{ads};B})[\frac{\text{kJ}}{\text{mol}}]$	$\Delta(-\Delta H_{\text{ads};C})[\frac{\text{kJ}}{\text{mol}}]$
Q_{low}	90 sccm/min	0	0
Q_{high}	110 sccm/min	1	1
p_{high}	1.1 bar	0	0
$t_{\text{exp,low}}$	1800 s	-4	-4
$t_{\text{exp,high}}$	3600 s	1	1
r_{low}	1.8 mm	1	2
r_{high}	2.2 mm	-1	-1
T_{low}	see table 7.1	-4	-5
T_{high}	see table 7.1	5	6

Following that, the final adsorption enthalpies, including uncertainties, are:

$$-\Delta H_{\text{ads};B} = 184^{+8}_{-9}\,\frac{\text{kJ}}{\text{mol}}$$

$$-\Delta H_{\text{ads};C} \geq 196\,\frac{\text{kJ}}{\text{mol}}$$

The large errors of the adsorption enthalpies are mainly caused by the high uncertainties of the higher temperatures in the column (see chapter 3.2.3).

4.2.3 Determination of the adsorption enthalpy of thallium on quartz glass in a wet helium atmosphere (Tl-H2O-700)

The evaluation of the taken γ spectra was performed as described for the previous measurements. Again the 884 keV line was selected for determining the adsorption enthalpies of the depositions (figure 4.4). The input parameters used for the Monte Carlo simulation are shown in table 4.5.

Table 4.5: Input parameters used for the Monte Carlo simulation to determine the adsorption enthalpy of Tl on a quartz glass column in wet helium. Here, M is the molar mass of Tl, F_{mp} the fraction of helium in the mobile phase, ρ the density at the boiling point, Q the gas flow rate, r the inner radius of the column, p the pressure inside the column, τ_0 the period of oscillation at the surface, T the temperature, and t_{exp} the experiment duration. It was assumed that the catcher foil required five minutes to heat up and evaporate thallium; therefore, the experiment duration assumed for the simulation was reduced by five minutes.

Input parameter	Value	Reference
M_{Tl}	195 g/mol	-
M_{He}	4 g/mol	-
F_{mp}	1	-
ρ_{Tl}	11.85 g/cm^3	[68]
ρ_{He}	0.125 g/cm^3	[112]
Q	100 sccm/min	-
r	2 mm	-
p	1 bar	-
τ_0	$0.2 \cdot 10^{-12}$ s^{-1}	[51]
T	see table 7.2	-
t_{exp}	3300 s	-

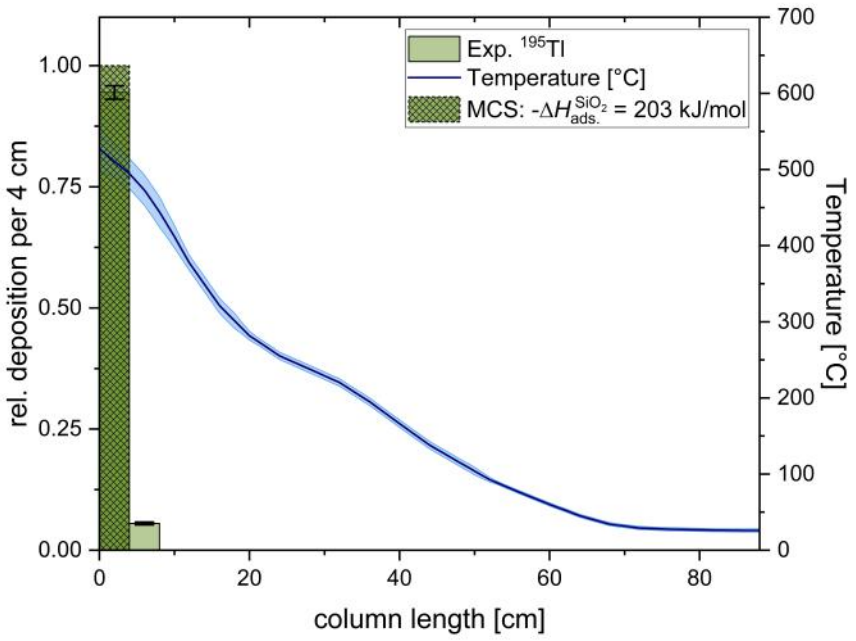

Figure 4.4: Thermochromatogram of Tl (884 keV line) on pretreated quartz glass columns in a wet helium atmosphere. The measured deposition is represented by the light green bars, while the Monte Carlo simulation is illustrated by the darker green, striped bars. The temperature gradient is shown in blue. To improve comparability between the simulation and the experimental data, the simulated activity was scaled by the ratio of the activity of the corresponding experimental peak to the total experimental activity. 0 cm corresponds to position of catcher foil. No Tl was detected in the charcoal filter.

For this experiment, one sharp deposition zone C was found in the column at a temperature of around 510 °C. This deposition was observed at the very beginning of the column. As it was described in chapter 4.2.2, it is not possible to give an absolute adsorption enthalpy for this species. Following that, the Monte Carlo simulation reveals a limit for the adsorption enthalpy of $-\Delta H_{\text{ads.}} \geq 203\,\text{kJ/mol}$. This is the lowest enthalpy value at which all simulated particles remain in the first section of the column.

The errors of the adsorption enthalpy were determined as described in chapter 3.2.3. The flow fluctuated between 101 and 104 sccm/min. This slightly increased flow rate is mainly caused by the water vapour added to the mobile phase. To account for this increased uncertainty, the lower and upper limit of the gas flow rate was adjusted accordingly (see table 4.6).

Table 4.6: Parameters varied in the simulation, their respective values, and the deviation from the with the most probable value determined adsorption enthalpy $\Delta(-\Delta H_{\text{ads.}})$ for experiment Tl-H2O-700.

Parameter	Input value	$\Delta(-\Delta H_{\text{ads;}C})[\frac{\text{kJ}}{\text{mol}}]$
Q_{low}	95 sccm/min	0
Q_{high}	105 sccm/min	0
p_{high}	1.1 bar	-1
$t_{\text{exp,low}}$	1800 s	-4
$t_{\text{exp,high}}$	3600 s	1
r_{low}	1.8 mm	1
r_{high}	2.2 mm	-1
T_{low}	see table 7.2	-5
T_{high}	see table 7.2	5

Following that, the final limit of the adsorption enthalpy, including uncertainties, are:

$$-\Delta H_{\text{ads;}C} \geq 192\,\frac{\text{kJ}}{\text{mol}}$$

The large error is mainly caused by the high uncertainties of the higher temperatures in the column (see chapter 3.2.3).

4.2.4 Determination of the adsorption enthalpy of thallium in a pure helium atmosphere on alpha-aluminium oxide (Tl-He-700-Al2O3)

Due to the wall thickness of the collimator, there is a small offset of 0.5 cm between the positions the gamma spectra were measured and the measurement points of the temperature gradient. Because the Monte Carlo simulation does not allow step sizes smaller than 1 cm, the temperature gradient was interpolated for 0.5 cm steps (see table 7.3). The input parameters used for the Monte Carlo simulation are shown in table 4.7.

Table 4.7: Input parameters used for the Monte Carlo simulation to determine the adsorption enthalpy of Tl on a α-Al_2O_3 column in a pure helium atmosphere. Here, M is the molar mass of Tl, F_{mp} the fraction of helium in the mobile phase, ρ the density at the boiling point, Q the gas flow rate, r the inner radius of the column, p the pressure inside the column, τ_0 the period of oscillation at the surface, T the temperature, and t_{exp} the experiment duration. It was assumed that the catcher foil required five minutes to heat up and evaporate thallium; therefore, the experiment duration assumed for the simulation was reduced by five minutes.

Input parameter	Value	Reference
M_{Tl}	196 g/mol	-
M_{He}	4 g/mol	-
F_{mp}	1	-
ρ_{Tl}	11.85 g/cm^3	[68]
ρ_{He}	0.125 g/cm^3	[112]
Q	100 sccm/min	-
r	2 mm	-
p	1 bar	-
τ_0	$0.2 \cdot 10^{-12}$ s^{-1}	[51]
T	see table 7.3	-
t_{exp}	5100 s	-

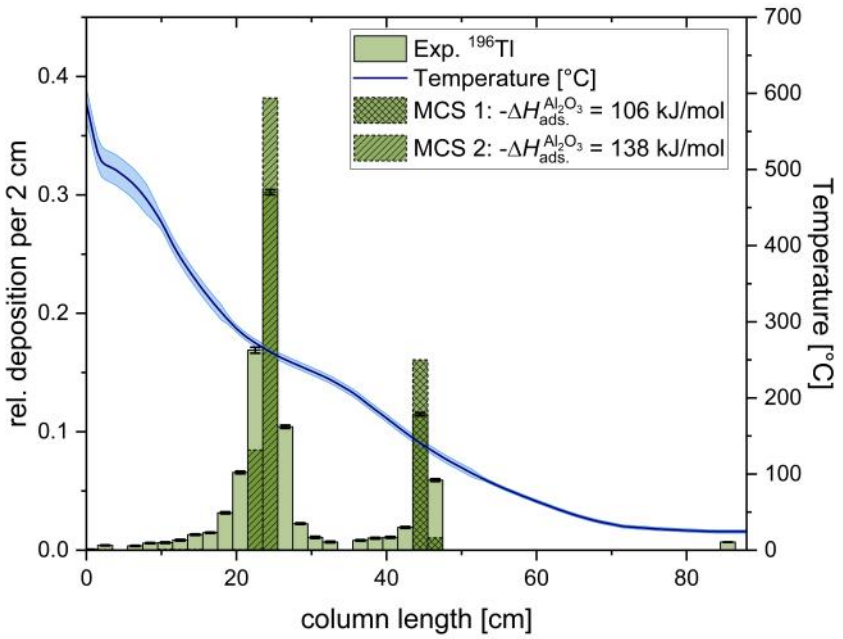

Figure 4.5: Thermochromatogram of Tl (426 keV line) on a α-Al_2O_3 column in a pure helium atmosphere. The measured deposition is represented by the light green bars, while the Monte Carlo simulation is illustrated by the darker green, striped bars. The temperature gradient is shown in blue. To improve comparability between the simulation and the experimental data, the simulated activity was scaled by the ratio of the activity of the corresponding experimental peak to the total experimental activity. 0 cm corresponds to position of catcher foil. No Tl was detected in the charcoal filter.

In this experiment two depositions zones, D and E were found in the column. Deposition zone D was found at a column temperature of around 140 °C and has a relative intensity of around 25%. In comparison, deposition zone E has a deposition temperature of 260 °C and a relative intensity of around 75%. The adsorption enthalpies values from the Monte Carlo simulations are -106 kJ/mol and -138 kJ/mol. The error of the adsorption enthalpies were determined as describe before. All varied parameters are shown in table 4.8.

Table 4.8: Parameters varied in the simulation, their respective values, and the deviation from the with the most probable value determined adsorption enthalpy $\Delta(-\Delta H_{\text{ads.}})$ for experiment Tl-He-700-Al2O3.

Parameter	Input value	$\Delta(-\Delta H_{\text{ads};D})[\frac{\text{kJ}}{\text{mol}}]$	$\Delta(-\Delta H_{\text{ads};E})[\frac{\text{kJ}}{\text{mol}}]$
Q_{low}	98 sccm/min	0	0
Q_{high}	102 sccm/min	1	1
p_{high}	1.1 bar	0	0
$t_{\text{exp,low}}$	3600 s	-2	-1
$t_{\text{exp,high}}$	5400 s	0	1
r_{low}	1.8 mm	0	1
r_{high}	2.2 mm	-1	-1
T_{low}	see table 7.3	-1	-1
T_{high}	see table 7.3	1	1

Following the varied parameters, the final adsorption enthalpies, including uncertainties, are:

$$-\Delta H_{\text{ads};D}^{\text{Al}_2\text{O}_3} = 106^{+2}_{-4}\,\frac{\text{kJ}}{\text{mol}}$$

$$-\Delta H_{\text{ads};E}^{\text{Al}_2\text{O}_3} = 138^{+4}_{-3}\,\frac{\text{kJ}}{\text{mol}}$$

4.2.5 Determination of the adsorption enthalpy of thallium on quartz glass in a pure oxygen atmosphere (Tl-pure-O2-700)

The evaluation of the taken γ spectra was performed as described for the previous measurements. The input parameters used for the Monte Carlo simulation are shown in table 4.9.

Table 4.9: Input parameters used for the Monte Carlo simulation to determine the adsorption enthalpy of Tl on a quartz glass column in a pure oxygen atmosphere. Here, M is the molar mass of Tl, F_{mp} the fraction of helium in the mobile phase, ρ the density at the boiling point, Q the gas flow rate, r the inner radius of the column, p the pressure inside the column, τ_0 the period of oscillation at the surface, T the temperature, and t_{exp} the experiment duration. It was assumed that the catcher foil required five minutes to heat up and evaporate thallium; therefore, the experiment duration assumed for the simulation was reduced by five minutes.

Input parameter	Value	Reference
M_{Tl}	196 g/mol	-
M_{He}	4 g/mol	-
$M_{\mathrm{O_2}}$	32 g/mol	-
F_{mp}	0	-
ρ_{Tl}	11.85 g/cm^3	[68]
ρ_{He}	0.125 g/cm^3	[112]
$\rho_{\mathrm{O_2}}$	1.141 g/cm^3	[113]
Q	100 sccm/min	-
r	2 mm	-
p	1 bar	-
τ_0	$0.2 \cdot 10^{-12}$ s^{-1}	[51]
T	see table 7.4	-
t_{exp}	2520 s	-

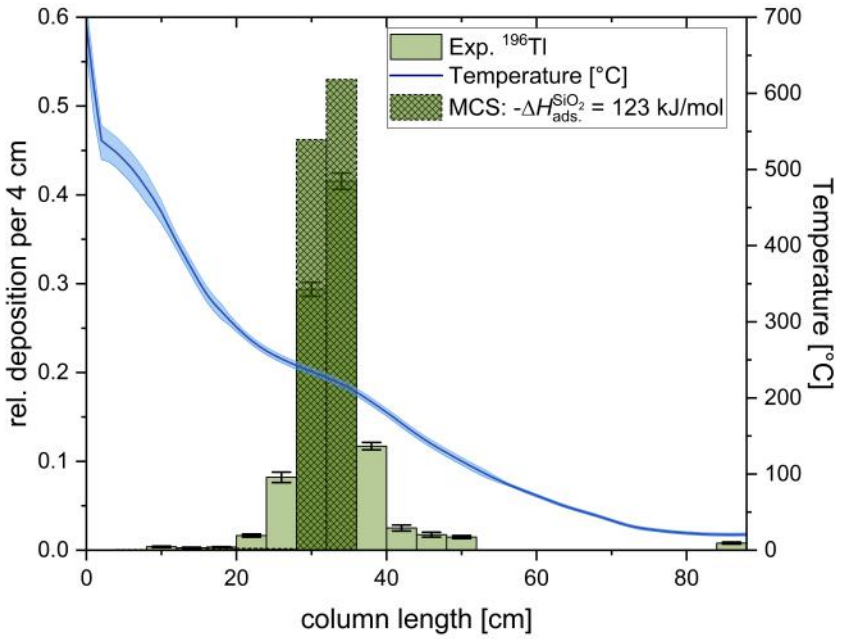

Figure 4.6: Thermochromatogram of Tl (426 keV line) on pretreated quartz glass columns in a pure oxygen atmosphere. The measured deposition is represented by the light green bars, while the Monte Carlo simulation is illustrated by the darker green, striped bars. The temperature gradient is shown in blue. To improve comparability between the simulation and the experimental data, the simulated activity was scaled by the ratio of the activity of the corresponding experimental peak to the total experimental activity. 0 cm corresponds to position of the catcher foil. No Tl was detected in the charcoal filter.

One deposition zone was found in the column for this experiment. This deposition zone F at a column temperature of around 220°C was assigned to an adsorption enthalpy of -123 kJ/mol. This enthalpy is identical to the enthalpy of deposition zone A, that was found in experiment Tl-He-700. However, the peak shape appears to be much broader.

The errors of the adsorption enthalpy were determined as described in chapter 3.2.3. The flow was measured to be around 150 sccm/min. The higher measured flow rate can be attributed to the use of a mass flow controller calibrated for helium. When used with oxygen, it overestimates the flow rate by a factor of 1.4. Therefore, the actual flow rate corresponded to the anticipated value of around 100 sccm/min.

Table 4.10: Parameters varied in the simulation, their respective values, and the deviation from the with the most probable value determined adsorption enthalpy $\Delta(-\Delta H_{\text{ads.}})$ for experiment Tl-pure-O2-700.

Parameter	Input value	$\Delta(-\Delta H_{\text{ads};F})[\frac{\text{kJ}}{\text{mol}}]$
Q_{low}	93 sccm/min	-1
Q_{high}	107 sccm/min	2
p_{high}	1.1 bar	-1
$t_{\text{exp,low}}$	1410 s	-3
$t_{\text{exp,high}}$	2820 s	1
r_{low}	1.8 mm	1
r_{high}	2.2 mm	-1
T_{low}	see table 7.4	-1
T_{high}	see table 7.4	1

Following that, the final adsorption enthalpies, including uncertainties, are:

$$-\Delta H_{\text{ads};F} = 123^{+5}_{-7}\,\frac{\text{kJ}}{\text{mol}}$$

Chapter 5

Discussion and interpretation of the results

5.1 Examination of quartz glass surfaces

The evaluation of the obtained infrared spectra (see figure 4.1) yields results that do not align well with theoretical expectations in most cases, although some findings did align with them. A lower peak intensity corresponds to a reduced concentration of the respective species on the surface compared to the reference sample, whereas a higher intensity indicates an increased concentration. As previously described, it was assumed that the concentration of O–H and O–D groups on the surface would increase for samples treated with (heavy) water vapour at elevated temperatures. Consequently, it is plausible that the spectrum of the sample treated with D_2O vapour (see figure 4.1, red line) shows a decreased intensity of the O–H stretching peak and an increased intensity of the O–D stretching peak. In this case, part of the hydrogen atoms would be replaced with deuterium, and new O–D groups would be formed on the surface.

For the sample treated at high temperatures with water vapour (see figure 4.1, green line), an increased concentration of O-H groups would be expected. Instead a decrease was found in the infrared spectrum. A possible explanation is that, under the given experimental conditions, dehydroxylation and hydroxylation processes occur simultaneously and compete with each other. Additionally, the quartz wool plug used in the setup likely reduces the amount of water reaching the sample surface, shifting the chemical equilibrium towards dehydroxylation.
The sample treated in a D_2O bath (see figure 4.1, blue line) exhibits a pronounced O-H signal, which is unexpected under these treatment conditions. This signal is likely caused by the adsorption of water from ambient air after treatment. In contrast, the sample treated in a regular water bath (see figure 4.1, violet line) shows the highest O-H group concentration among all samples. Since it is known from the D_2O bath-treated sample that the actual increase in surface hydroxylation is limited, the observed O-H signal likely originates from physically adsorbed water rather than chemically formed hydroxyl groups.

In summary, the results of the RAIRS measurements generally not align with theoretical expectations. As previously discussed, literature broadly agrees that the degree of hydroxylation of quartz glass can be modified using the methods applied in this study.[86,88] This was confirmed only for the sample treated with D_2O at high temperatures. The decrease in O-H concentration observed for the high-temperature H_2O treatment may be explained by the reduced water availability at the surface. Moreover, the sensitivity of the RAIRS method to the exact positioning of the sample within the spectrometer may contribute to the observed deviations, as even minor misalignments can significantly affect the recorded spectra. Nevertheless, the pronounced spectral changes observed in the treated samples indicate that the surface modification method is effective and detectable via RAIRS, particularly when compared to a reference sample. However, more measurements to confirm the effectiveness of the RAIRS method are needed to develop a more robust and error-resistant procedure for sample analysis, which is essential to improve reliability of the quartz glass surface analysis.

5.2 Thermochromatographic studies of thallium

5.2.1 Determined adsorption enthalpies of thallium species on quartz glass

The goal of these experiments was to determine the adsorption enthalpies of various thallium species on quartz glass. In three experiments on quartz glass, a total of five adsorption enthalpy values were measured. Considering the respective uncertainties, it was found that some adsorption enthalpies values overlapped within error margins, resulting in three distinct values: $-123 \pm 5\,\mathrm{kJ/mol}$, $-185^{+12}_{-7}\,\mathrm{kJ/mol}$ and $\leq -192\,\mathrm{kJ/mol}$ (see chapter 4.2). In the following (and also in the chapter 'Results'), these enthalpies will be referred to as A, B, and C. Also the Tl-pure-O2-700 experiment yielded an adsorption enthalpy of $-123\,\mathrm{kJ/mol}$ but exhibited a very broad deposition zone. Since the peak shape differed significantly from that observed for A, this deposition was attributed to an additional species, hereafter referred to as F. Table 5.1 provides an overview of the identified deposition peaks along with their corresponding adsorption enthalpies on quartz glass.

Table 5.1: Summary of the determined deposition peaks with corresponding deposition temperature and adsorption enthalpy on quartz glass as well as the gas phase composition.

Experiment	gas phase	dep. temp. [°C]	$-\Delta H_{\mathrm{ads}}$ [kJ/mol]	peak
Tl-He-700	He	≈ 250	123 ± 5	A
Tl-He-700	He	≈ 460	185^{+5}_{-12}	B
Tl-O2-700	He + O_2	≈ 430	184^{+8}_{-9}	B
Tl-O2-700	He + O_2	≈ 530	≥ 196	C
Tl-H2O-700	He + H_2O	≈ 510	≥ 192	C
Tl-pure-O2-700	O_2	≈ 220	123^{+5}_{-7}	F

The observation of three (respectively four) distinct adsorption enthalpies suggests the presence of three (four) different thallium species in the experiments, indicating that the initially formed thallium atoms must have undergone chemical reactions to form additional species. Potential reaction partners could, in principle, be present either on the column surface or in the gas phase.

Adsorption enthalpy A was solely determined from the Tl-He-700 experiment. The absence of reactive gases and the use of less reactive (pretreated) quartz columns in this experiment was intended to prevent thallium atoms from undergoing chemical reactions and forming new species. However, a second deposition peak corresponding to adsorption enthalpy B was also observed, implying the presence of a second species and, consequently, reactive components within the column during the experiment. This suggests that enthalpy A is unlikely to correspond to elemental thallium due to its high reactivity towards these components. The measured adsorption enthalpy $-123 \pm 5\,\mathrm{kJ/mol}$ is in good agreement with the literature value of $-134 \pm 5\,\mathrm{kJ/mol}$,[75] which has been attributed to thallium hydroxide.
Completely eliminating potential impurities from the experimental setup is nearly impossible. Given that thallium is highly reactive (see chapter 2.5) and reacts readily with even trace impurities, it is likely that the measured adsorption enthalpy corresponds to thallium hydroxide, which may have been formed through reactions either with impurities in the gas phase or with residual active groups on the treated surface. A minor discrepancy was observed between the peak shape of the actual measured deposition and the Monte Carlo simulation. This can be attributed to the fact that the thallium evaporation was not instantaneous (as assumed in the simulation); instead, atoms were continuously released as the catcher foil was heated. Consequently, retention times within the column varied among individual atoms. A broad distribution of retention times, which influenced the peak shape of the experimental data, must therefore be assumed. These effects could not be incorporated into the simulation, as the exact distribution of residence times was unknown. Accounting for these effects would likely have resulted in a broader simulated peak.

However, this effect does not explain the discrepancy between the actual and simulated peak shape of deposition peak B. The species with adsorption enthalpy B exhibits a very broad deposition peak, making it difficult to simulate using the standard Monte Carlo approach. It is well established that deposition patterns can broaden when chemical reactions occur during an experiment.[114–116] Moreover, enthalpy B does not correspond to any published literature value (see table 2.1), complicating its assignment to a specific species. The occurrence of the broad peak in the experiment with added oxygen implies that it is caused by an oxide species. Following that, the peak in the experiment with pure helium could be caused by oxygen impurities in the gas phase or on the column surface or surface modifications due to the oxygen. As discussed in chapter 2.5, several thallium oxide species are known. The most stable and common oxides, Tl_2O and Tl_2O_3, both contain two thallium atoms per molecule. Thermochromatography is a single-atom technique that detects individual thallium atoms. As the probability of atomic interactions is negligible, the formation of multi-thallium species can be ruled out. Consequently,

these oxides can be excluded as possible candidates for adsorption enthalpy B. However, certain mono-thallium oxide species are known. For example, TlO is stable only in the gas phase, which suggests that it could exist under the experimental conditions. Its general instability may account for the broad shape of the deposition peak, provided that a transport reaction is involved in the process. TlOO represents another possible mono-thallium oxide species. Thus, the peak shape of B could be explained by the formation of one or several different thallium species, most likely oxides.
Alternatively, another explanation for the broad deposition observed for B is possible. In the Tl-He-700 experiment, the amount of gas-phase impurities should have been sufficiently low that reactions with the hot surface represent the more likely pathway for reactions of previously elemental thallium. This would imply that B could correspond to a reaction zone where elemental thallium interacts with residual reactive groups on the quartz surface. Although the pretreatment of the columns significantly reduces the concentration of O-H groups, it is unlikely that the surface was completely dehydroxylated. If the formation of a more volatile species, such as TlOH occurs the species would then desorb from the surface and be detected in deposition zone A. Other, less volatile species would remain adsorbed on the surface at higher temperatures. Given the available data, it is not possible to conclusively clarify the origin of deposition zone B. A mixture of different species cannot be excluded, nor can the presence of a reaction zone between thallium and the surface.

Adsorption enthalpy C was identified in experiments involving either a helium-oxygen mixture or wet helium. As previously discussed, it was assumed that thallium would react with water to form thallium hydroxide. Consequently, adsorption enthalpy A was expected to appear in the Tl-H2O-700 experiment as well. However, no deposition of thallium hydroxide was detected. According to macroscopic chemistry experiments with thallium, thallium hydroxide should have been present under these conditions (see chapter 2.5). Instead, the position of deposition zone C directly adjacent to the catcher foil suggests that the thallium species, once evaporated, was immediately immobilized upon first contact, presumably as a result of a chemical reaction with the hot surface. The resulting thallium species became strongly bound to the surface, most likely through a bond between thallium atoms and oxygen atoms on the quartz surface. All experiments in which deposition zone C was observed likely involved the presence of water. In the Tl-H2O-700 experiment water vapour was added intentionally and in the Tl-O2-700 experiment, it can be assumed that water was present as an impurity in the oxygen gas. Therefore, it appears reasonable to assume that water increases the reactivity between thallium and the hot quartz surface, thereby enabling the formation of strong surface bonds.
Based on this assumption, the question arises why deposition zone C was not detected in the Tl-pure-O2-700 experiment. The obtained data suggest that with increasing oxygen content, a growing proportion of the initially bound species was desorbed from deposition zone C and redeposited further downstream at deposition zones B or F, respectively. This indicates that oxygen participates in the desorption process of a thallium oxide, potentially enabling the cleavage of the strong Tl-O-Si bonds through oxidative mechanisms. These observations point to a complex interaction

system involving thallium, the quartz surface, and the reactants water and oxygen, which can be influenced by small changes in experimental conditions.

An unambiguous assignment of deposition zones C, F, and (as discussed previously) B based on the available results is not possible. Even though there are indications pointing toward specific species, alternative interpretations cannot be excluded. The strongly bound species associated with peak C could correspond to elemental thallium chemisorbed onto the surface, but strongly bound hydroxide or oxide species are also conceivable. Adsorption enthalpy F could potentially be assigned to thallium hydroxide, similar to enthalpy A, but due to the broad deposition zone, the existence of another species with a coincidentally similar adsorption enthalpy cannot be ruled out. Further experiments are required to achieve a definitive assignment.

Comparing these results to the literature data (see chapter 2.5.3) does not yield a clearer picture of single-atom thallium chemistry. As described earlier, the assignment of deposition zone A to TlOH was already proposed by Serov et al.[75] The experimentally determined adsorption enthalpy of -123 ± 5,kJ/mol for this species is in good agreement with the value calculated by Ilias and Pershina for TlOH adsorbed on geminal OH groups on quartz glass.[80] The adsorption enthalpies determined for the other species, however, do not match any values reported in the literature. This underlines the necessity of further experiments to allow for definitive assignments. Notably, the most recent studies also reported similar difficulties in assigning adsorption enthalpies to specific species.[77,78]

5.2.2 Determined adsorption enthalpies of thallium species on alpha-aluminium oxide

As mentioned in chapter 2.6.2, the columns for the experiments on corundum were composed of sintered aluminium oxide, resulting in a rougher and thus larger surface area. This raises the question of whether such surface characteristics significantly influence the adsorption process and therefore shifts the obtained adsorption enthalpy. However, accompanying investigations (see appendix section 7.3) indicate that this effect is minor and can be neglected within the scope of the experimental uncertainties. It is therefore useful to compare the results from the experiment using α-aluminium oxide columns with those of the Tl-He-700 experiment, as all experimental conditions except for the column material were identical. While two distinct deposition peaks (A and B; see chapter 5.2.1) were observed on quartz glass, two corresponding depositions peaks (D and E) were also identified on α-aluminium oxide. The associated adsorption enthalpies were -106^{+4}_{-2} kJ/mol for peak D and -138^{+3}_{-4} kJ/mol for peak E. Table 5.2 provides an overview of all identified deposition peaks along with their corresponding adsorption enthalpies on aluminium oxide.

Table 5.2: Summary of the determined deposition peaks with corresponding deposition temperature and adsorption enthalpy on aluminium oxide as well as the gas phase composition.

Experiment	gas phase	dep. temp. [°C]	$-\Delta H_{\text{ads}}$ [kJ/mol]	peak
Tl-He-700-Al2O3	He	≈ 140	106^{+2}_{-4}	D
Tl-He-700-Al2O3	He	≈ 260	138^{+4}_{-3}	E

As in the case of quartz glass, the presence of two deposition zones implies the presence of two thallium species. Given thallium's high reactivity toward trace impurities, it is reasonable to assume that these species were formed through reactions with residual gases or surface functionalities in the column. Consequently, the observed species are not elemental thallium. Since the experimental parameters were identical, it is further assumed that the same thallium species were deposited in both experiments. Deposition peak D was therefore assigned to TlOH, while peak E could be conclusively attributed to a less volatile oxidized Tl species (see chapter 5.2.1). It is noteworthy that the adsorption enthalpies obtained on α-aluminium oxide are shifted to lower values compared to those on quartz glass. Since these are the first thermochromatographic experiments with thallium on α-aluminium oxide, there are no existing literature data for direct comparison. To further investigate the influence of α-aluminium oxide on the adsorption behaviour of thallium species, additional experiments using this material are recommended. Repeating the measurements under the same conditions as for quartz glass columns would enable a direct comparison between the two substrates. Identifying systematic trends could improve the predictive power for future studies involving lighter homologues or superheavy elements themselves.

Chapter 6

Summary and outlook

The first part of this thesis focused on the chemical treatment of quartz glass plates with the aim of either hydroxylating or dehydroxylating their surfaces and identifying a suitable method to examine the resulting surface groups. Since X-ray photoelectron spectroscopy (XPS) did not yield the desired results, reflection–absorption infrared spectroscopy (RAIRS) was employed. The observed behaviour of the quartz glass surfaces did not fully align with the theoretical expectations for hydroxylation and dehydroxylation. The decrease in O–H group concentration in a sample presumed to undergo hydroxylation suggests that, at elevated temperatures, the hydroxylation and dehydroxylation processes behave as a chemical equilibrium. Thus, a sufficient partial pressure of water is likely required to shift the equilibrium more towards surface hydroxylation. RAIRS has been identified as a promising technique for the future characterization of hydroxylation states on quartz surfaces. To validate its applicability, additional measurements are planned, starting with a systematic investigation of the dehydroxylation process. Several samples will be heated in an inert gas atmosphere at 1000 °C for varying durations. This simpler reaction, without a competing hydroxylation process, will allow for validation of the RAIRS method based on the observable trend of dehydroxylation on the examined sample surfaces. Another promising technique for the characterization of quartz surfaces is ultraviolet photoelectron spectroscopy (UPS). Measurements using that analytical method are planned as well.

The second major part of this thesis focused on the thermochromatographic determination of adsorption enthalpies of various thallium species on quartz glass and α-aluminium oxide. On quartz glass, a total of six deposition peaks was observed, corresponding to three (four) distinct adsorption enthalpies. The theoretical assumption that thallium is highly reactive towards even trace impurities was confirmed, as no elemental thallium was detected in any of the experiments. The species with an adsorption enthalpy of $-123 \pm 5\,\mathrm{kJ/mol}$ is in good agreement with the literature value of $-134 \pm 5\,\mathrm{kJ/mol}$ for TlOH and is thus also assigned to TlOH.[75] A second, broader deposition peak with an adsorption enthalpy of $(-185^{+4}_{-8})\,\mathrm{kJ/mol}$ was not assigned to a specific species. Instead, the possibility of a mixture of different thallium oxide species or the presence of a reaction zone on the quartz column was discussed. A third thallium species, with an estimated adsorption enthalpy of $\geq -192\,\mathrm{kJ/mol}$,

could only be reported as a lower limit due to its proximity to the catcher foil. Based on its position and the experimental conditions, this species was attributed to a thallium compound strongly bound to the surface. The results suggest a complex and sensitive system involving multiple thallium species, the precise nature of which remains to be clarified in future investigations.
In the experiment using an α-aluminium oxide column, two deposition zones were identified. Since the experimental conditions were identical to those of one of the quartz glass column experiments, in which two species were also observed, it was assumed that the same species were deposited. To gain a better understanding of how adsorption enthalpies of thallium (or other elements) differ between quartz glass and α-aluminium oxide surfaces, additional thermochromatographic measurements using corundum columns are recommended. Such data could support more reliable predictions in future experiments, particularly those involving lighter homologues or superheavy elements. The obtained adsorption enthalpies and the observed complexity of the thallium species system provide valuable insights into the chemistry of single thallium atoms. Thallium has been the subject of considerable scientific debate in recent years, and the findings presented here confirm the high complexity of its chemical behaviour. Additional measurements will be essential to obtain a more comprehensive and conclusive understanding. It may also be beneficial to complement chromatography experiments with ultra micro quantities (picogram to microgram) of specific thallium compounds. By starting with a known species (e.g. thallium hydroxide) a more systematic overview of the expected deposition behaviour of the compound can be obtained.

Bibliography

[1] D. Mendelejew, *Zeitschrift für Chemie* **1869**, *12*, 405–406.

[2] M. R. Kibler, *Foundations of Chemistry* **2007**, *9*, 221–234.

[3] J. Kratz, K. H. Lieser, *Nuclear and Radiochemistry: Fundamentals and Applications*, Wiley, 3rd ed., **2013**.

[4] M. Binnewies, M. Finze, M. Jäckel, P. Schmidt, H. Willner, G. Rayner-Canham, *Allgemeine und Anorganische Chemie*, Springer Spektrum, 3rd ed., **2016**.

[5] G. T. Seaborg, *Chemical and Engineering News Archive* **1945**, *23*, 2190–2193.

[6] M. Schädel, *Angewandte Chemie International Edition* **2006**, *45*, 368–401.

[7] A. Türler, V. Pershina, *Chemical Reviews* **2013**, *113*, 1237–1312.

[8] S. A. Giuliani, Z. Matheson, W. Nazarewicz, E. Olsen, P.-G. Reinhard, J. Sadhukhan, B. Schuetrumpf, N. Schunck, P. Schwerdtfeger, *Reviews of Modern Physics* **2019**, *91*, 011001.

[9] Y. Oganessian, V. K. Utyonkov, *Reports on Progress in Physics* **2015**, *78*, 036301.

[10] K. J. Moody, *The Chemistry of Superheavy Elements - Synthesis of Superheavy Elements*, Springer, 2nd ed., **2014**.

[11] M. Schädel, *Philosophical Transactions of the Royal Society A: Mathematical Physical and Engineering Sciences* **2015**, *373*, 20140191.

[12] V. Pershina, *The Chemistry of Superheavy Elements - Theoretical Chemistry of the Heaviest Elements*, Springer, 2nd ed., **2014**.

[13] J. Kratz, *Handbook of Nuclear Chemistry - Elements and isotopes: Formation, transformation, distribution - Chemistry of Transactinides*, *Vol. 2*, Springer, 2nd ed., **2011**.

[14] C. E. Düllmann, *Nuclear and Radiochemistry - Volume 2: Modern Applications - Radioelements: Transactinides*, de Gruyter, 2nd ed., **2022**.

[15] Y. Oganessian, *Nuclear Physics News* **2019**, *29*, 5–10.

[16] P. Schwerdtfeger, L. F. Pašteka, A. Punnett, P. O. Bowman, *Nuclear Physics A* **2015**, *944*, 551–577.

[17] P. Pyykko, *Chemical Reviews* **1988**, *88*, 563–594.

[18] J. Autschbach, *The Journal of Chemical Physics* **2012**, *136*, 1–15.

[19] A. Novgorodov, F. Rösch, N. Korolev, *Handbook of Nuclear Chemistry - Instrumentation, separation techniques, enviromental issues - Radiochemical separations by thermochromatography*, *Vol. 5*, Springer, 2nd ed., **2011**.

[20] A. Yakushev, J. Khuyagbaatar, C. E. Düllmann, M. Block, R. A. Cantemir, D. M. Cox, D. Dietzel, F. Giacoppo, Y. Hrabar, M. Iliaš, E. Jäger, J. Krier, D. Krupp, N. Kurz, L. Lens, S. Löchner, C. Mokry, P. Mošať, V. Pershina, S. Raeder, D. Rudolph, J. Runke, L. G. Sarmiento, B. Schausten, U. Scherer, P. Thörle-Pospiech, N. Trautmann, M. Wegrzecki, P. Wieczorek, *Frontiers in Chemistry* **2024**, *12*, 1474820.

[21] A. Yakushev, L. Lens, C. E. Düllmann, J. Khuyagbaatar, E. Jäger, J. Krier, J. Runke, H. M. Albers, M. Asai, M. Block, J. Despotopulos, A. Di Nitto, K. Eberhardt, U. Forsberg, P. Golubev, M. Götz, S. Götz, H. Haba, L. Harkness-Brennan, R.-D. Herzberg, F. P. Heßberger, D. Hinde, A. Hübner, D. Judson, B. Kindler, Y. Komori, J. Konki, J. V. Kratz, N. Kurz, M. Laatiaoui, S. Lahiri, B. Lommel, M. Maiti, A. K. Mistry, C. Mokry, K. J. Moody, Y. Nagame, J. P. Omtvedt, P. Papadakis, V. Pershina, D. Rudolph, L. G. Samiento, T. K. Sato, M. Schädel, P. Scharrer, B. Schausten, D. A. Shaughnessy, J. Steiner, P. Thörle-Pospiech, A. Toyoshima, N. Trautmann, K. Tsukada, J. Uusitalo, K.-O. Voss, A. Ward, M. Wegrzecki, N. Wiehl, E. Williams, V. Yakusheva, *Frontiers in Chemistry* **2022**, *10*, 976635.

[22] A. Yakushev, L. Lens, C. E. Düllmann, M. Block, H. Brand, T. Calverley, M. Dasgupta, A. Di Nitto, M. Götz, S. Götz, H. Haba, L. Harkness-Brennan, R.-D. Herzberg, F. P. Heßberger, D. Hinde, A. Hübner, E. Jäger, D. Judson, J. Khuyagbaatar, B. Kindler, Y. Komori, J. Konki, J. V. Kratz, J. Krier, N. Kurz, M. Laatiaoui, B. Lommel, C. Lorenz, M. Maiti, A. K. Mistry, C. Mokry, Y. Nagame, P. Papadakis, A. Såmark-Roth, D. Rudolph, J. Runke, L. G. Sarmiento, T. K. Sato, M. Schädel, P. Scharrer, B. Schausten, J. Steiner, P. Thörle-Pospiech, A. Toyoshima, N. Trautmann, J. Uusitalo, A. Ward, M. Wegrzecki, V. Yakusheva, *Frontiers in Chemistry* **2021**, *9*, 753778.

[23] G. Herrmann, *Angewandte Chemie International Edition* **1988**, *27*, 1417–1436.

[24] G. Gamow, *Proceedings of the Royal Society of London. Series A Containing Papers of a Mathematical and Physical Character* **1930**, *126*, 632–644.

[25] T. Fényes, *Handbook of Nuclear Chemistry - Basics of Nuclear Science - Basics Properties of the Atomic Nucleus*, Springer, 2nd ed., **2011**.

[26] R.-D. Herzberg, *The Chemistry of Superheavy Elements - Nuclear Structure of Superheavy Elements*, Springer, 2nd ed., **2014**.

[27] F. Rösch, *Nuclear- and Radiochemistry - Volume 1: Introduction*, De Gruyter, 2nd ed., **2022**.

[28] C. F. v. Weizsäcker, *Zeitschrift für Physik* **1935**, *96*, 431–458.

[29] H. A. Bethe, R. F. Bacher, *Reviews of Modern Physics* **1936**, *8*, 82–229.

[30] O. Haxel, J. H. D. Jensen, H. E. Suess, *Physical Review* **1949**, *75*, 1766–1766.

[31] M. G. Mayer, *Physical Review* **1949**, *75*, 1969–1970.

[32] N. Schunck, D. Regnier, *Progress in Particle and Nuclear Physics* **2022**, *125*, 103963.

[33] G. Münzenberg, M. Gupta, *Handbook of Nuclear Chemistry - Elements and isotopes: Formation, transformation, distribution - Production and Identification of Transactinide Elements*, *Vol. 2*, Springer, 2nd ed., **2011**.

[34] W. D. Myers, W. J. Swiatecki, *Nuclear Physics* **1966**, *81*, 1–60.

[35] E. O. Fiset, J. R. Nix, *Nuclear Physics A* **1972**, *193*, 647–671.

[36] S. Ćwiok, P.-H. Heenen, W. Nazarewicz, *Nature* **2005**, *433*, 705–709.

[37] V. Pershina, *Comptes Rendus. Chimie* **2020**, *23*, 255–265.

[38] L. G. Sobotka, V. E. Viola, *Handbook of Nuclear Chemistry - Basics of Nuclear Science - Nuclear Reactions*, Springer, 2nd ed., **2011**.

[39] V. I. Zagrebaev, Y. Aritomo, M. G. Itkis, Y. T. Oganessian, M. Ohta, *Physical Review C* **2001**, *65*, 014607.

[40] N. Bohr, *Nature* **1936**, *137*, 344–348.

[41] V. I. Zagrebaev, *Physical Review C* **2001**, *64*, 034606.

[42] D. C. Hoffman, D. A. Shaughnessy, *Handbook of Nuclear Chemistry - Elements and isotopes: Formation, transformation, distribution - Superheavy Elements*, *Vol. 2*, Springer, 2nd ed., **2011**.

[43] P. Pyykko, J. P. Desclaux, *Accounts of Chemical Research* **1979**, *12*, 276–281.

[44] N. Trautmann, S. Happel, F. Roesch, *Nuclear and Radiochemistry - Volume 2: Modern Applications - Radiochemical separations*, de Gruyter, 2nd ed., **2022**.

[45] P. W. Atkins, J. de Paula, *Atkins' physical chemistry*, Oxford University Press, 8th ed., **2006**.

[46] C. Le Naour, D. C. Hoffman, D. Trubert, *The Chemistry of Superheavy Elements - Fundamental and Experimental Aspects of Single Atom-at-a-Time Chemistry*, Springer, 2nd ed., **2014**.

[47] K. D. Bartle, P. Myers, *Trends in Analytical Chemistry* **2002**, *21*, 547–557.

[48] J. M. Gates, C. E. Düllmann, M. Schädel, A. Yakushev, A. Türler, K. Eberhardt, J. V. Kratz, D. Ackermann, L.-L. Andersson, M. Block, W. Brüchle, J. Dvorak, H. G. Essel, P. A. Ellison, J. Even, U. Forsberg, J. Gellanki, A. Gorshkov, R. Graeger, K. E. Gregorich, W. Hartmann, R.-D. Herzberg, F. P. Heßberger, D. Hild, A. Hübner, E. Jäger, J. Khuyagbaatar, B. Kindler, J. Krier, N. Kurz, S. Lahiri, D. Liebe, B. Lommel, M. Maiti, H. Nitsche, J. P. Omtvedt, E. Parr, D. Rudolph, J. Runke, H. Schaffner, B. Schausten, E. Schimpf, A. Semchenkov, J. Steiner, P. Thörle-Pospiech, J. Uusitalo, M. Wegrzecki, N. Wiehl, *Physical Review C* **2011**, *83*, 054618.

[49] H. W. Gäggeler, D. T. Jost, U. Baltensperger, A. Weber, A. Kovacs, D. Vermeulen, A. Türler, *Nuclear Instruments and Methods in Physics Research Section A: Accelerators Spectrometers Detectors and Associated Equipment* **1991**, *309*, 201–208.

[50] A. Yakushev, J. M. Gates, A. Türler, M. Schädel, C. E. Düllmann, D. Ackermann, L.-L. Andersson, M. Block, W. Brüchle, J. Dvorak, K. Eberhardt, H. G. Essel, J. Even, U. Forsberg, A. Gorshkov, R. Graeger, K. E. Gregorich, W. Hartmann, R.-D. Herzberg, F. P. Heßberger, D. Hild, A. Hübner, E. Jäger, J. Khuyagbaatar, B. Kindler, J. V. Kratz, J. Krier, N. Kurz, B. Lommel, L. J. Niewisch, H. Nitsche, J. P. Omtvedt, E. Parr, Z. Qin, D. Rudolph, J. Runke, B. Schausten, E. Schimpf, A. Semchenkov, J. Steiner, P. Thörle-Pospiech, J. Uusitalo, M. Wegrzecki, N. Wiehl, *Inorganic Chemistry* **2014**, *53*, 1624–1629.

[51] I. Zvára, *The Inorganic Radiochemistry of Heavy Elements*, Springer, 1st ed., **2008**.

[52] D. Dietzel, A. Yakushev, C. E. Düllmann, *Journal of Radioanalytical and Nuclear Chemistry* **2024**, *333*, 3487–3496.

[53] R. Eichler, B. Eichler, *The Chemistry of Superheavy Elements - Thermochemical Data from Gas-Phase Adsorption and Methods of Their Estimation*, Springer, 2nd ed., **2014**.

[54] M. Králik, *Chemical Papers* **2014**, *68*, 1625–1638.

[55] A. Dąbrowski, *Advances in Colloid and Interface Science* **2001**, *93*, 135–224.

[56] F. Huber, J. Berwanger, S. Polesya, S. Mankovsky, H. Ebert, F. J. Giessibl, *Science* **2019**, *366*, 235–238.

[57] S. G. Brass, G. Ehrlich, *Physical Review Letters* **1986**, *57*, 2532–2535.

[58] R. L. Harrison, C. Granja, C. Leroy, *AIP Conference Proceedings*, **2010**.

[59] I. Zvára, *Radiochimica Acta* **1985**, *38*, 95–102.

[60] D. C. Joy, *Scanning Microscopy* **1991**, *5*, 329–337.

[61] G. Genchi, A. Carocci, G. Lauria, M. S. Sinicropi, A. Catalano, *Applied Sciences* **2021**, *11*, 8322.

[62] W. Crookes, *The London Edinburgh and Dublin Philosophical Magazine and Journal of Science* **1861**, *21*, 301–305.

[63] W. Crookes, *Proceedings of the Royal Society of London* **1863**, *12*, 150–159.

[64] R. K. DeKosky, *The British Journal for the History of Science* **1973**, *6*, 400–423.

[65] M. Sager, *Toxicological and Environmental Chemistry* **1994**, *45*, 11–32.

[66] Z. Sóti, J. Magill, R. Dreher, *EPJ Nuclear Sciences and Technologies* **2019**, *5*, 6.

[67] M. S. Verani, *Clinical Nuclear Medicine* **1983**, *8*, 276–287.

[68] E. Wiberg, N. Wiberg, A. Holleman, *Anorganische Chemie Band 1 - Grundlagen und Hauptgruppenelemente*, de Gruyter, 103rd ed., **2017**.

[69] H. H. Binder, *Kleines Lexikon der chemischen Elemente: mit zahlreichen Abbildungen und Tabellen*, Lehmanns Media, 2nd ed., **2016**.

[70] A. L. J. Peter, T. Viraraghavan, *Environment International* **2005**, *31*, 493–501.

[71] M. Klemm, D. Meißner, *Toxichem Krimtech* **2012**, *79*, 17–22.

[72] E. Pietsch, E. Haller, A. Kotowski, M. D. Maire, F. Struwe, *Gmelins Handbuch der Anorganischen Chemie - Thallium und Radioaktive Isotope*, Verlag Chemie, 8th ed., **1940**.

[73] B. Eichler, *Das Verhalten Flüchtiger Radionuklide im Temperaturgradientenrohr unter Vakuum*, Report ZFK-346, Zentralinstitut Kernforschung Dresden, **1977**.

[74] P. Steinegger, M. Asai, R. Dressler, R. Eichler, Y. Kaneya, A. Mitsukai, Y. Nagame, D. Piguet, T. K. Sato, M. Schädel, S. Takeda, A. Toyoshima, K. Tsukada, A. Türler, A. Vascon, *The Journal of Physical Chemistry C* **2016**, *120*, 7122–7132.

[75] A. Serov, R. Eichler, R. Dressler, D. Piguet, A. Türler, A. Vögele, D. Wittwer, H. W. Gäggeler, *Radiochimica Acta* **2013**, *101*, 421–426.

[76] L. Lens, A. Yakushev, C. E. Düllmann, M. Asai, J. Ballof, M. Block, H. M. David, J. Despotopulos, A. Di Nitto, K. Eberhardt, J. Even, M. Götz, S. Götz, H. Haba, L. Harkness-Brennan, F. P. Heßberger, R. D. Herzberg, J. Hoffmann, A. Hübner, E. Jäger, D. Judson, J. Khuyagbaatar, B. Kindler, Y. Komori, J. Konki, J. V. Kratz, J. Krier, N. Kurz, M. Laatiaoui, S. Lahiri, B. Lommel,

M. Maiti, A. K. Mistry, C. Mokry, K. Moody, Y. Nagame, J. P. Omtvedt, P. Papadakis, V. Pershina, J. Runke, M. Schädel, P. Scharrer, T. Sato, D. Shaughnessy, B. Schausten, P. Thörle-Pospiech, N. Trautmann, K. Tsukada, J. Uusitalo, A. Ward, M. Wegrzecki, N. Wiehl, V. Yakusheva, *Radiochimica Acta* **2018**, *106*, 949–962.

[77] C. Gut, J. Wilson, P. V. Grundler, van der Meulen N.P., A. Sommerhalder, P. Steinegger, *Annual Report 2023 - Offline thermochromatography of Tl on various dehydroxylated fused silica surfaces*, Paul Scherrer Institut - Laboratory of Radiochemistry, **2023**.

[78] J. M. Wilson, M. Asai, Y. Ito, T. Kazuaki, Y. Nagame, R. Eichler, A. Sommerhalder, P. V. Grundler, N. P. van der Muelen, D. Herrmann, T. K. Sato, P. Steinegger, *Online and offline gas-adsorption chromatography with Tl for future Nh experiments*, 10th International Conference on Nuclear and Radiochemistry, Brighton, **2024**.

[79] V. Pershina, *The Journal of Physical Chemistry C* **2016**, *120*, 20232–20238.

[80] M. Iliaš, V. Pershina, *Inorganic Chemistry* **2022**, *61*, 15910–15920.

[81] L. P. Davila, S. H. Risbud, J. F. Shackelford, *Ceramic and Glass Materials - Structure, Properties and Processing - Quartz and Silicas*, Springer, 1st ed., **2008**.

[82] R. H. Doremus, *Annual Review of Materials Science* **1972**, *2*, 93–120.

[83] W. H. Zachariasen, *Journal of the American Chemical Society* **1932**, *54*, 3841–3851.

[84] A. P. Velmuzhov, M. V. Sukhanov, M. F. Churbanov, T. V. Kotereva, L. V. Shabarova, Y. P. Kirillov, *Inorganic Materials* **2018**, *54*, 925–930.

[85] V. Pershina, *Physical Chemistry Chemical Physics* **2016**, *18*, 17750–17756.

[86] J. E. Shelby, *Introduction to Glass Science and Technology*, The Royal Society of Chemistry, 2nd ed., **2005**.

[87] H. Boehm, *Angewandte Chemie International Edition* **1966**, *5*, 533–544.

[88] J. E. Shelby, *Journal of Non-Crystalline Solids* **1994**, *179*, 138–147.

[89] J. E. Shelby, *Journal of Applied Physics* **1980**, *51*, 2589–2593.

[90] P. J. Eng, T. P. Trainor, G. E. Brown Jr., G. A. Waychunas, M. Newville, S. R. Sutton, M. L. Rivers, *Science* **2000**, *288*, 1029–1033.

[91] X.-G. Wang, A. Chaka, M. Scheffler, *Physical Review Letters* **2000**, *84*, 3650–3653.

[92] X. Yang, Z. Sun, D. Wang, W. Forsling, *Journal of Colloid and Interface Science* **2007**, *308*, 395–404.

[93] J. W. Elam, C. E. Nelson, M. A. Cameron, M. A. Tolbert, S. M. George, *The Journal of Physical Chemistry B* **1998**, *102*, 7008–7015.

[94] R. H. Doremus, *Ceramic and Glass Materials - Structure, Properties and Processing - Alumina*, Springer, 1st ed., **2008**.

[95] C. van Nguyen, S. K. Sistla, S. van Kempen, N. A. Giang, A. Bezold, C. Broeckmann, F. Lange, *Journal of the Ceramic Society of Japan* **2016**, *124*, 301–312.

[96] M. P. Seah, *Surface and Interface Analysis* **1980**, *2*, 222–239.

[97] J. P. Matinlinna, S. Areva, L. V. J. Lassila, P. K. Vallittu, *Surface and Interface Analysis* **2004**, *36*, 1314–1322.

[98] P. B. McGinnis, J. E. Shelby, *Journal of Non-Crystalline Solids* **1994**, *179*, 185–193.

[99] L. M. Ng, R. Simmons, *Analytical Chemistry* **1999**, *71*, 343–350.

[100] T. Hecht, *Physikalische Grundlagen der IR-Spektroskopie: Von mechanischen Schwingungen zur Vorhersage und Interpretation von IR-Spektren*, Springer, 1st ed., **2019**.

[101] H. Günzler, *IR-Spektroskopie*, Wiley, 4th ed., **2011**.

[102] M. Koç, E. Karabudak, *Applied Spectroscopy Reviews* **2017**, *53*, 420–438.

[103] I. A. Mudunkotuwa, A. A. Minshid, V. H. Grassian, *The Analyst* **2014**, *139*, 870–881.

[104] P. Hollins, *Infrared Reflection–Absorption Spectroscopy*, Wiley, 1st ed., **2006**.

[105] G. Steiner, *Handbook of Spectroscopy - Measurement Techniques*, Wiley, 1st ed., **2003**.

[106] M. Trenary, *Annual Review of Physical Chemistry* **2000**, *51*, 381–403.

[107] F. Hoffmann, *Surface Science Reports* **1983**, *3*, 107.

[108] J. D. Stickler, K. J. Hofstetter, *Physical Review C* **1974**, *9*, 1064–1071.

[109] X. Huang, M. Kang, *Nuclear Data Sheets* **2014**, *121*, 395–560.

[110] H. Xiaolong, *Nuclear Data Sheets* **2007**, *108*, 1093–1286.

[111] K. Hermainski, *master thesis*, Johannes-Gutenberg-University Mainz, **2024**.

[112] J. Satterly, *Reviews of Modern Physics* **1936**, *8*, 347–357.

[113] A. Van Itterbeek, O. Verbeke, *Cryogenics* **1960**, *1*, 77–80.

[114] S. Hübener, S. Taut, A. Vahle, R. Dressler, B. Eichler, H. W. Gäggeler, D. T. Jost, D. Piguet, A. Türler, W. Brüchle, *Radiochimica Acta* **2001**, *89*, 737–742.

[115] A. Vahle, S. Hübener, R. Dressler, B. Eichler, A. Türler, *Radiochimica Acta* **1997**, *78*, 53–58.

[116] A. Vahle, PhD thesis, TU Dresden, **1996**.

List of Figures

2.1 Differences between experimental atomic masses and masses calculated with the LDM 4
2.2 Spontaneous fission half-lives 6
2.3 Comparison cold-fusion and hot-fusion 8
2.5 Comparison of thermochromatography and isothermal chromatography. 12
2.7 Overview of the most common thallium species 16
2.8 Structure of crystalline vs. non crystalline silica 19
2.9 Siloxane groups and various types of silanol groups 19
2.10 Hydroxylation/dehydroxylation process of a corundum surface 20
2.11 Principle of reflection–absorption infrared spectroscopy 22

3.1 Schematic of the setup used for hydroxylation at high temperatures of quartz glass plates. The water/D_2O storage was placed inside a T-shaped aluminium tube. 24
3.2 Schematic of the setup used for dehydroxylation of quartz glass columns. The oven used a built-in temperature sensor. 25
3.3 Schematic of the thermochromatography setup used for examining the adsorption enthalpy of different thallium species. 26
3.4 Determined γ-spectrum of the first four centimetres next to the catcher foil of the Tl-He-700 experiment. 31
3.5 Gaussian fit of the 884 keV line of the γ-spectrum of the first four centimeters next to the catcher foil of the Tl-He-700 experiment. . . . 32

4.1 Differential spectra of the four treated quartz glass samples in comparison to the untreated sample as a reference 35
4.2 Thermochromatogram of Tl on pretreated quartz glass columns in a pure helium atmosphere 37
4.3 Thermochromatogram of Tl on pretreated quartz glass columns in a helium-oxygen atmosphere 40
4.4 Thermochromatogram of Tl on pretreated quartz glass columns in a wet helium atmosphere 43
4.5 Thermochromatogram of Tl on a α-Al_2O_3 column in a pure helium atmosphere 46
4.6 Thermochromatogram of Tl on pretreated quartz glass columns in a helium-oxygen atmosphere 49

7.1 Thermochromatogram of Tl on pretreated quartz glass columns at a lower evaporation temperature 71
7.2 Histogram of the deposited activity of thallium isotopes on a preheated quartz glass column at a starting temperature of 300°C. 72
7.3 Laser scanning images and corresponding height profiles of α-aluminium oxide and quartz glass plates. 86

List of Tables

2.1 Overview of experimentally determined adsorption enthalpies of thallium species on quartz glass, along with the corresponding chemical species. . . . 17
2.2 Overview of calculated adsorption enthalpies of thallium species on quartz glass, along with the corresponding chemical species. . . . 18

3.1 Parameters of the RAIRS measurements of the quartz glass plates. . 25
3.2 Voltages applied to the different ovens during the experiment Tl-He-300. 27
3.3 Voltages applied to the different ovens during the experiment Tl-He-700. 28

4.1 Input parameters used for the Monte Carlo simulation for determining the adsorption enthalpy of Tl on a quartz glass column . . . 37
4.2 Error parameters and results for experiment Tl-He-700 . . . 38
4.3 Input parameters used for the Monte Carlo simulation for determining the adsorption enthalpy of Tl on a quartz glass column in a helium-oxygen atmosphere . . . 39
4.4 Error parameters and results for experiment Tl-O2-700 . . . 41
4.5 Input parameters used for the Monte Carlo simulation for determining the adsorption enthalpy of Tl on a quartz glass column in a wet helium atmosphere . . . 42
4.6 Error parameters and results for experiment Tl-H2O-700 . . . 44
4.7 Input parameters used for the Monte Carlo simulation for determining the adsorption enthalpy of Tl on a α-Al_2O_3 column in a pure helium atmosphere . . . 45
4.8 Error parameters and results for experiment Tl-He-700-Al2O3 . . . 47
4.9 Input parameters used for the Monte Carlo simulation for determining the adsorption enthalpy of Tl on a quartz glass column in a pure oxygen atmosphere . . . 48
4.10 Error parameters and results for experiment Tl-pure-O2-700 . . . 50

5.1 Summary of the determined deposition peaks with corresponding deposition temperature and adsorption enthalpy on quartz glass as well as the gas phase composition. . . . 52
5.2 Summary of the determined deposition peaks with corresponding deposition temperature and adsorption enthalpy on aluminium oxide as well as the gas phase composition. . . . 56

7.1 Interpolated temperature gradient for experiment Tl-O2-700 and Tl-He-700 72
7.2 Interpolated temperature gradient for experiment Tl-H2O-700 75
7.3 Interpolated temperature gradient for experiment Tl-He-700-Al2O3 . 77
7.4 Interpolated temperature gradient for experiment Tl-pure-O2-700 . . 82
7.5 Calculated and experimental isotope distribution from the reaction of a 48 MeV ^{3}He beam and a ^{197}Au foil. 84
7.6 Determined mean surface roughness parameters, the area of the 'photographed' and the 'actual' surface as well as the calculated factors for the α-aluminium oxide and quartz glass plates 86

Chapter 7

Appendix

7.1 Evaluation of the Tl-He-300 experiment

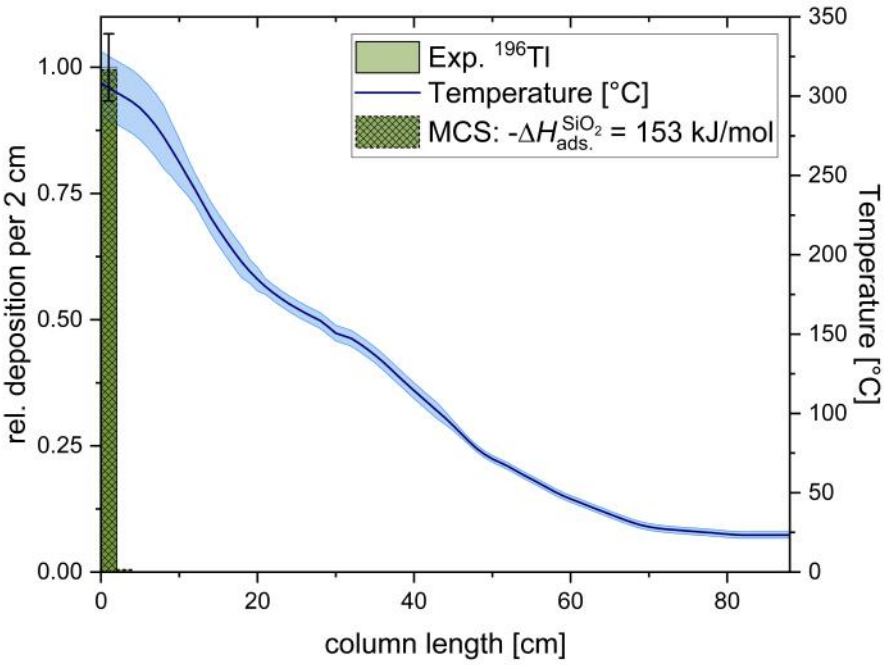

Figure 7.1: Thermochromatogram of Tl (426 keV line) on pretreated quartz glass columns in a pure helium atmosphere at 300 °C evaporation temperature. The measured deposition is represented by the light green bars, while the Monte Carlo simulation is illustrated by the darker green, striped bars. The temperature gradient is shown in blue. To improve comparability between the simulation and the experimental data, the simulated activity was scaled by the ratio of the activity of the corresponding experimental peak to the total experimental activity. 0 cm corresponds to position of catcher foil. No Tl was detected in the charcoal filter.

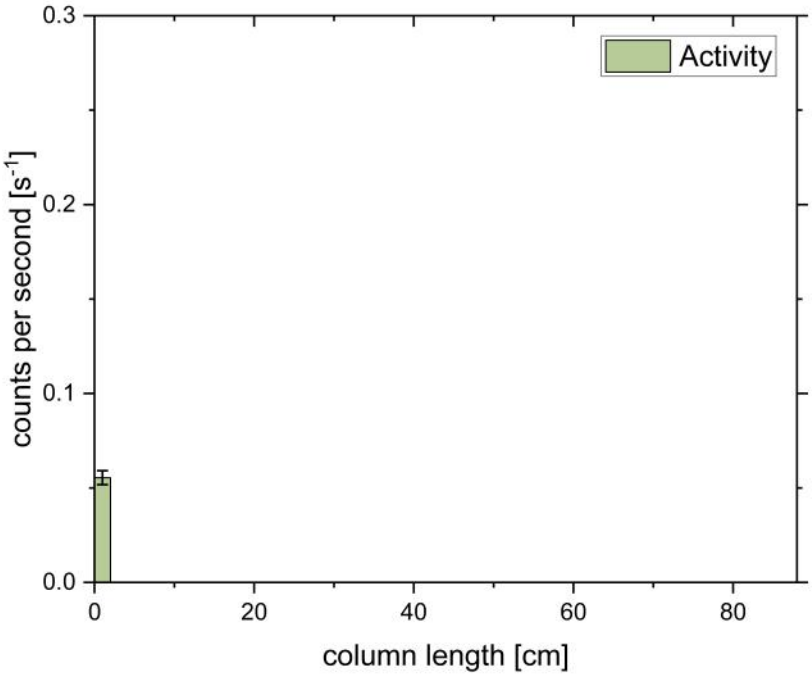

Figure 7.2: Histogram of the deposited activity of thallium isotopes on a preheated quartz glass column at a starting temperature of 300°C.

7.2 Temperature gradients

Table 7.1: Interpolated temperature gradient for experiment Tl-O2-700 and Tl-He-700. The temperature was measured every second centimetre. The remaining values were interpolated using the Akima Spline method. $T_{\min}$ and $T_{\max}$ describe the lower and upper limit of the error interval of the measured temperature (see chapter 3.2.3)

position [cm]	T [K]	$T_{\min}$ [K]	$T_{\max}$ [K]
0.0	320.75	280.75	360.75
1.0	301.31	261.31	341.31
2.0	340.75	300.75	380.75
3.0	450.98	410.98	490.98
4.0	596.25	556.25	636.25
5.0	783.15	743.15	823.15
6.0	902.75	862.75	942.75
7.0	906.44	866.44	946.44
8.0	909.75	869.75	949.75
9.0	913.44	873.44	953.44
10.0	912.19	872.19	952.19
11.0	857.67	822.67	892.67
12.0	813.05	783.05	843.05

position [cm]	T [K]	$T_{\min}$ [K]	$T_{\max}$ [K]
13.0	805.93	780.93	830.93
14.0	799.25	779.25	819.25
15.0	792.92	772.92	812.92
16.0	786.45	766.45	806.45
17.0	778.37	758.37	798.37
18.0	769.35	749.35	789.35
19.0	758.95	738.95	778.95
20.0	746.35	726.35	766.35
21.0	731.81	714.81	748.81
22.0	716.75	701.75	731.75
23.0	699.81	687.81	711.81
24.0	681.85	671.85	691.85
25.0	665.24	655.24	675.24
26.0	648.85	638.85	658.85
27.0	632.94	622.94	642.94
28.0	617.65	607.65	627.65
29.0	604.69	594.69	614.69
30.0	593.25	583.25	603.25
31.0	582.11	575.11	589.11
32.0	572.05	566.05	578.05
33.0	563.66	558.66	568.66
34.0	556.45	551.45	561.45
35.0	549.57	544.57	554.57
36.0	542.85	537.85	547.85
37.0	536.68	531.68	541.68
38.0	531.45	526.45	536.45
39.0	526.84	521.84	531.84
40.0	522.26	517.26	527.26
41.0	517.70	512.70	522.70
42.0	513.15	508.15	518.15
43.0	508.62	503.62	513.62
44.0	504.11	499.11	509.11
45.0	499.59	494.59	504.59
46.0	495.05	490.05	500.05
47.0	490.04	485.04	495.04
48.0	484.22	479.22	489.22
49.0	477.71	472.71	482.71
50.0	470.65	465.65	475.65
51.0	462.94	457.94	467.94
52.0	454.71	449.71	459.71
53.0	446.45	441.45	451.45
54.0	438.65	433.65	443.65
55.0	431.27	426.27	436.27
56.0	424.02	419.02	429.02
57.0	417.01	412.01	422.01

position [cm]	T [K]	$T_{\min}$ [K]	$T_{\max}$ [K]
58.0	410.35	405.35	415.35
59.0	404.04	399.04	409.04
60.0	398.01	393.01	403.01
61.0	392.19	387.19	397.19
62.0	386.55	381.55	391.55
63.0	380.95	375.95	385.95
64.0	375.45	370.45	380.45
65.0	370.30	366.11	374.48
66.0	365.75	362.57	368.93
67.0	361.61	359.43	363.79
68.0	357.49	355.31	359.67
69.0	353.38	351.20	355.56
70.0	349.25	347.08	351.42
71.0	345.10	342.93	347.27
72.0	340.95	338.78	343.12
73.0	336.80	334.63	338.96
74.0	332.65	330.48	334.82
75.0	328.65	326.48	330.81
76.0	324.87	322.71	327.03
77.0	321.26	319.10	323.42
78.0	317.75	315.59	319.91
79.0	314.45	312.30	316.61
80.0	311.58	309.43	313.74
81.0	309.22	307.06	311.37
82.0	307.45	305.30	309.60
83.0	306.12	303.97	308.28
84.0	305.02	302.87	307.18
85.0	304.14	301.98	306.29
86.0	303.45	301.30	305.60
87.0	302.89	300.74	305.04
88.0	302.36	300.21	304.51
89.0	301.83	299.68	303.98
90.0	301.25	299.10	303.40
91.0	300.51	298.36	302.66
92.0	299.65	297.50	301.80
93.0	298.89	296.74	301.04
94.0	298.45	296.30	300.60
95.0	298.30	296.15	300.45
96.0	298.25	296.10	300.40
97.0	298.25	296.10	300.40
98.0	298.25	296.10	300.40
99.0	298.24	296.09	300.39
100.0	298.25	296.10	300.40

Table 7.2: Interpolated temperature gradient for experiment Tl-H2O-700. The temperature was measured every second centimetre. The remaining values were interpolated using the Akima Spline method. $T_{\min}$ and $T_{\max}$ describe the lower and upper limit of the error interval of the measured temperature (see chapter 3.2.3)

position [cm]	T [K]	$T_{\min}$ [K]	$T_{\max}$ [K]
0.0	321.85	281.85	361.85
1.0	400.85	360.85	440.85
2.0	479.85	439.85	519.85
3.0	558.85	518.85	598.85
4.0	637.85	597.85	677.85
5.0	809.80	769.80	849.80
6.0	981.75	941.75	1021.75
7.0	985.00	945.00	1025.00
8.0	988.25	948.25	1028.25
9.0	974.45	934.45	1014.45
10.0	960.65	920.65	1000.65
11.0	880.50	845.50	915.50
12.0	800.35	770.35	830.35
13.0	792.05	767.05	817.05
14.0	783.75	763.75	803.75
15.0	775.85	755.85	795.85
16.0	767.95	747.95	787.95
17.0	757.05	737.05	777.05
18.0	746.15	726.15	766.15
19.0	731.75	711.75	751.75
20.0	717.35	697.35	737.35
21.0	701.10	684.10	718.10
22.0	684.85	669.85	699.85
23.0	667.65	655.65	679.65
24.0	650.45	640.45	660.45
25.0	636.43	626.43	646.43
26.0	622.40	612.40	632.40
27.0	608.38	598.38	618.38
28.0	594.35	584.35	604.35
29.0	584.50	574.50	594.50
30.0	574.65	564.65	584.65
31.0	564.80	557.30	572.30
32.0	554.95	548.95	560.95
33.0	548.35	543.35	553.35
34.0	541.75	536.75	546.75
35.0	535.15	530.15	540.15
36.0	528.55	523.55	533.55
37.0	524.18	519.18	529.18
38.0	519.80	514.80	524.80
39.0	515.43	510.43	520.43

position [cm]	T [K]	$T_{\min}$ [K]	$T_{\max}$ [K]
40.0	511.05	506.05	516.05
41.0	506.65	501.65	511.65
42.0	502.25	497.25	507.25
43.0	497.85	492.85	502.85
44.0	493.45	488.45	498.45
45.0	487.15	482.15	492.15
46.0	480.85	475.85	485.85
47.0	474.55	469.55	479.55
48.0	468.25	463.25	473.25
49.0	461.03	456.03	466.03
50.0	453.80	448.80	458.80
51.0	446.58	441.58	451.58
52.0	439.35	434.35	444.35
53.0	432.33	427.33	437.33
54.0	425.30	420.30	430.30
55.0	418.28	413.28	423.28
56.0	411.25	406.25	416.25
57.0	405.53	400.53	410.53
58.0	399.80	394.80	404.80
59.0	394.08	389.08	399.08
60.0	388.35	383.35	393.35
61.0	382.75	377.75	387.75
62.0	377.15	372.15	382.15
63.0	371.55	367.36	375.74
64.0	365.95	362.77	369.13
65.0	361.75	359.57	363.93
66.0	357.55	355.37	359.73
67.0	353.35	351.17	355.53
68.0	349.15	346.98	351.32
69.0	345.20	343.03	347.37
70.0	341.25	339.08	343.42
71.0	337.30	335.13	339.47
72.0	333.35	331.18	335.52
73.0	329.65	327.49	331.81
74.0	325.95	323.79	328.11
75.0	322.25	320.09	324.41
76.0	318.55	316.39	320.71
77.0	315.75	313.59	317.91
78.0	312.95	310.79	315.11
79.0	310.15	307.99	312.31
80.0	307.35	305.20	309.50
81.0	306.08	303.92	308.23
82.0	304.80	302.65	306.95
83.0	303.53	301.37	305.68
84.0	302.25	300.10	304.40

position [cm]	T [K]	$T_{\min}$ [K]	$T_{\max}$ [K]
85.0	301.85	299.70	304.00
86.0	301.45	299.30	303.60
87.0	301.05	298.90	303.20
88.0	300.65	298.50	302.80
89.0	300.45	298.30	302.60
90.0	300.25	298.10	302.40
91.0	300.05	297.90	302.20
92.0	299.85	297.70	302.00
93.0	299.70	297.55	301.85
94.0	299.55	297.40	301.70
95.0	299.40	297.25	301.55
96.0	299.25	297.10	301.40
97.0	299.20	297.05	301.35
98.0	299.15	297.00	301.30
99.0	299.10	296.95	301.25
100.0	299.05	296.90	301.20

Table 7.3: Interpolated temperature gradient for experiment Tl-He-700-Al2O3. The temperature was measured every second centimetre. The remaining values were interpolated using the Akima Spline method. $T_{\min}$ and $T_{\max}$ describe the lower and upper limit of the error interval of the measured temperature (see chapter 3.2.3)

position [cm]	T [K]	$T_{\min}$ [K]	$T_{\max}$ [K]
0.0	369.65	329.65	409.65
0.5	371.85	331.85	411.85
1.0	378.87	338.87	418.87
1.5	389.11	349.11	429.11
2.0	400.95	360.95	440.95
2.5	415.80	375.80	455.80
3.0	436.76	396.76	476.76
3.5	464.80	424.80	504.80
4.0	500.85	460.85	540.85
4.5	561.47	521.47	601.47
5.0	647.60	607.60	687.60
5.5	736.84	716.84	756.84
6.0	806.75	786.75	826.75
6.5	856.53	836.53	876.53
7.0	898.82	878.82	918.82
7.5	931.38	911.38	951.38
8.0	951.95	931.95	971.95
8.5	963.94	943.94	983.94
9.0	970.23	950.23	990.23
9.5	967.86	947.86	987.86
10.0	953.85	933.85	973.85

position [cm]	T [K]	$T_{\min}$ [K]	$T_{\max}$ [K]
10.5	931.40	921.40	941.40
11.0	906.99	896.99	916.99
11.5	882.59	872.59	892.59
12.0	860.15	850.15	870.15
12.5	837.61	827.61	847.61
13.0	814.49	804.49	824.49
13.5	795.16	785.16	805.16
14.0	783.95	773.95	793.95
14.5	779.61	769.61	789.61
15.0	777.08	767.08	787.08
15.5	775.04	772.65	777.43
16.0	772.15	769.76	774.54
16.5	768.47	766.08	770.85
17.0	764.80	762.42	767.18
17.5	760.96	758.58	763.34
18.0	756.75	754.37	759.13
18.5	751.92	749.54	754.29
19.0	746.43	744.05	748.80
19.5	740.40	738.03	742.77
20.0	733.95	731.58	736.32
20.5	727.12	724.75	729.48
21.0	719.83	717.47	722.19
21.5	712.08	709.73	714.44
22.0	703.85	701.50	706.20
22.5	694.77	692.42	697.12
23.0	684.98	682.64	687.33
23.5	675.26	672.92	677.60
24.0	666.35	664.02	668.68
24.5	658.24	655.91	660.57
25.0	650.42	648.09	652.74
25.5	642.91	640.59	645.23
26.0	635.75	633.43	638.07
26.5	628.82	626.50	631.13
27.0	622.02	619.71	624.33
27.5	615.41	613.10	617.71
28.0	609.05	606.75	611.35
28.5	602.93	600.63	605.23
29.0	596.97	594.68	599.27
29.5	591.16	588.86	593.45
30.0	585.45	583.16	587.74
30.5	579.87	577.58	582.16
31.0	574.47	572.19	576.76
31.5	569.32	567.03	571.60
32.0	564.45	562.17	566.73
32.5	559.95	557.67	562.23

position [cm]	T [K]	$T_{\min}$ [K]	$T_{\max}$ [K]
33.0	555.83	553.55	558.11
33.5	552.07	549.80	554.35
34.0	548.65	546.38	550.92
34.5	545.43	543.16	547.70
35.0	542.31	540.04	544.58
35.5	539.31	537.04	541.58
36.0	536.45	534.18	538.72
36.5	533.66	531.40	535.93
37.0	530.92	528.65	533.18
37.5	528.28	526.02	530.55
38.0	525.85	523.59	528.11
38.5	523.56	521.30	525.82
39.0	521.31	519.05	523.58
39.5	519.11	516.85	521.37
40.0	516.95	514.69	519.21
40.5	514.82	512.56	517.08
41.0	512.70	510.44	514.96
41.5	510.58	508.32	512.83
42.0	508.45	506.20	510.70
42.5	506.30	504.05	508.55
43.0	504.12	501.87	506.37
43.5	501.91	499.66	504.16
44.0	499.65	497.40	501.90
44.5	497.21	494.97	499.46
45.0	494.54	492.29	496.78
45.5	491.72	489.47	493.96
46.0	488.85	486.61	491.09
46.5	486.01	483.76	488.25
47.0	483.10	480.86	485.34
47.5	479.99	477.75	482.23
48.0	476.55	474.31	478.79
48.5	472.83	470.59	475.06
49.0	469.03	466.79	471.26
49.5	465.21	462.98	467.44
50.0	461.45	459.22	463.68
50.5	457.75	455.52	459.98
51.0	454.06	451.83	456.28
51.5	450.36	448.14	452.59
52.0	446.65	444.43	448.87
52.5	442.88	440.66	445.10
53.0	439.06	436.84	441.28
53.5	435.23	433.02	437.45
54.0	431.45	429.23	433.67
54.5	427.75	425.54	429.96
55.0	424.14	421.93	426.36

position [cm]	T [K]	$T_{\min}$ [K]	$T_{\max}$ [K]
55.5	420.64	418.43	422.85
56.0	417.25	415.04	419.46
56.5	413.96	411.76	416.17
57.0	410.75	408.54	412.95
57.5	407.58	405.38	409.79
58.0	404.45	402.25	406.65
58.5	401.31	399.11	403.51
59.0	398.20	395.99	400.40
59.5	395.16	392.96	397.36
60.0	392.25	390.05	394.45
60.5	389.48	387.28	391.67
61.0	386.79	384.60	388.99
61.5	384.16	381.97	386.35
62.0	381.55	379.36	383.74
62.5	378.94	376.75	381.13
63.0	376.35	374.16	378.53
63.5	373.78	371.59	375.96
64.0	371.25	369.06	373.44
64.5	368.79	366.60	370.97
65.0	366.40	364.21	368.58
65.5	364.05	361.87	366.24
66.0	361.75	359.57	363.93
66.5	359.47	357.29	361.64
67.0	357.22	355.04	359.39
67.5	355.03	352.86	357.21
68.0	352.95	350.77	355.13
68.5	350.94	348.76	353.12
69.0	348.96	346.78	351.13
69.5	346.99	344.82	349.17
70.0	345.05	342.88	347.22
70.5	343.11	340.94	345.28
71.0	341.17	339.00	343.34
71.5	339.25	337.08	341.42
72.0	337.35	335.18	339.52
72.5	335.49	333.32	337.65
73.0	333.66	331.49	335.82
73.5	331.85	329.68	334.02
74.0	330.05	327.88	332.22
74.5	328.26	326.10	330.43
75.0	326.50	324.34	328.66
75.5	324.76	322.60	326.92
76.0	323.05	320.89	325.21
76.5	321.40	319.24	323.56
77.0	319.83	317.67	321.99
77.5	318.32	316.16	320.48

position [cm]	T [K]	$T_{\min}$ [K]	$T_{\max}$ [K]
78.0	316.85	314.69	319.01
78.5	315.42	313.27	317.58
79.0	314.06	311.91	316.22
79.5	312.77	310.61	314.93
80.0	311.55	309.39	313.71
80.5	310.41	308.26	312.57
81.0	309.35	307.20	311.50
81.5	308.34	306.18	310.49
82.0	307.35	305.20	309.50
82.5	306.33	304.18	308.49
83.0	305.34	303.18	307.49
83.5	304.49	302.34	306.65
84.0	303.95	301.80	306.10
84.5	303.60	301.45	305.75
85.0	303.25	301.10	305.40
85.5	302.90	300.75	305.05
86.0	302.55	300.40	304.70
86.5	302.20	300.05	304.35
87.0	301.85	299.70	304.00
87.5	301.50	299.35	303.65
88.0	301.15	299.00	303.30
88.5	300.83	298.68	302.98
89.0	300.54	298.39	302.69
89.5	300.29	298.14	302.44
90.0	300.05	297.90	302.20
90.5	299.82	297.67	301.97
91.0	299.59	297.44	301.74
91.5	299.37	297.22	301.52
92.0	299.15	297.00	301.30
92.5	298.94	296.79	301.09
93.0	298.74	296.59	300.89
93.5	298.54	296.39	300.69
94.0	298.35	296.20	300.50
94.5	298.16	296.01	300.31
95.0	297.99	295.84	300.14
95.5	297.85	295.70	299.99
96.0	297.75	295.60	299.90
96.5	297.70	295.55	299.85
97.0	297.67	295.52	299.82
97.5	297.66	295.51	299.80
98.0	297.65	295.50	299.80
98.5	297.65	295.50	299.79
99.0	297.64	295.49	299.79
99.5	297.64	295.49	299.79

position [cm]	T [K]	$T_{\min}$ [K]	$T_{\max}$ [K]
100.0	297.65	295.50	299.80

Table 7.4: Interpolated temperature gradient for experiment Tl-pure-O2-700. The temperature was measured every second centimetre. The remaining values were interpolated using the Akima Spline method. $T_{\min}$ and $T_{\max}$ describe the lower and upper limit of the error interval of the measured temperature (see chapter 3.2.3)

position [cm]	T [K]	$T_{\min}$ [K]	$T_{\max}$ [K]
0.00	308.55	268.55	348.55
1.0	305.14	265.14	345.14
2.0	315.55	275.55	355.55
3.0	331.09	291.09	371.09
4.0	377.85	337.85	417.85
5.0	545.80	505.80	585.80
6.0	750.05	710.05	790.05
7.0	904.18	864.18	944.18
8.0	1001.35	961.35	1041.35
9.0	1017.39	977.39	1057.39
10.0	1007.05	967.05	1047.05
11.0	990.69	955.69	1025.69
12.0	963.35	933.35	993.35
13.0	880.94	840.94	905.94
14.0	811.25	786.25	831.25
15.0	803.34	783.34	823.34
16.0	795.75	775.75	815.75
17.0	785.86	765.86	805.86
18.0	775.15	755.15	795.15
19.0	762.49	742.49	782.49
20.0	748.55	728.55	768.55
21.0	733.72	716.72	750.72
22.0	717.15	702.15	732.15
23.0	698.04	686.04	710.04
24.0	678.85	668.85	688.85
25.0	660.97	650.97	670.97
26.0	643.35	633.35	653.35
27.0	625.82	615.82	635.82
28.0	609.75	599.75	619.75
29.0	597.16	587.16	607.16
30.0	586.65	576.65	596.65
31.0	576.25	569.25	583.25
32.0	566.25	560.25	572.25
33.0	556.96	551.96	561.96
34.0	548.55	543.55	553.55
35.0	541.18	536.18	546.18

position [cm]	T [K]	$T_{\min}$ [K]	$T_{\max}$ [K]
36.0	534.95	529.95	539.95
37.0	529.48	524.48	534.48
38.0	524.55	519.55	529.55
39.0	520.00	515.00	525.00
40.0	515.75	510.75	520.75
41.0	511.79	506.79	516.79
42.0	507.85	502.85	512.85
43.0	503.95	498.95	508.95
44.0	500.05	495.05	505.05
45.0	495.94	490.94	500.94
46.0	491.41	486.41	496.41
47.0	486.38	481.38	491.38
48.0	480.75	475.75	485.75
49.0	474.57	469.57	479.57
50.0	468.01	463.01	473.01
51.0	461.19	456.19	466.19
52.0	454.25	449.25	459.25
53.0	447.10	442.10	452.10
54.0	439.77	434.77	444.77
55.0	432.50	427.50	437.50
56.0	425.55	420.55	430.55
57.0	419.02	414.02	424.02
58.0	412.81	407.81	417.81
59.0	406.87	401.87	411.87
60.0	401.15	396.15	406.15
61.0	395.58	390.58	400.58
62.0	390.13	385.13	395.13
63.0	384.82	379.82	389.82
64.0	379.65	374.65	384.65
65.0	374.58	369.58	379.58
66.0	369.64	365.59	373.68
67.0	364.93	361.88	367.97
68.0	360.55	358.51	362.59
69.0	356.47	354.42	358.51
70.0	352.53	350.50	354.57
71.0	348.71	346.67	350.75
72.0	344.95	342.91	346.99
73.0	341.18	339.14	343.21
74.0	337.42	335.39	339.45
75.0	333.81	331.78	335.84
76.0	330.45	328.42	332.48
77.0	327.38	325.35	329.40
78.0	324.46	322.43	326.48
79.0	321.58	319.56	323.61
80.0	318.65	316.63	320.67

position [cm]	T [K]	$T_{\min}$ [K]	$T_{\max}$ [K]
81.0	315.56	313.54	317.59
82.0	312.39	310.37	314.41
83.0	309.24	307.22	311.26
84.0	306.25	304.23	308.27
85.0	303.78	301.76	305.80
86.0	301.97	299.96	303.98
87.0	300.60	298.59	302.61
88.0	299.45	297.44	301.46
89.0	298.37	296.35	300.38
90.0	297.37	295.35	299.38
91.0	296.48	294.47	298.49
92.0	295.75	293.74	297.76
93.0	295.13	293.12	297.15
94.0	294.60	292.59	296.61
95.0	294.16	292.15	296.17
96.0	293.85	291.84	295.86
97.0	293.67	291.66	295.68
98.0	293.61	291.60	295.62
99.0	293.67	291.66	295.68
100.0	293.85	291.84	295.86

Table 7.5: Calculated and experimental isotope distribution from the reaction of a 48 MeV ^{3}He beam and a ^{197}Au foil. The calculations were made using the software LISEcute++. The experimental data was taken from ref. [108]

.

Isotope	calc. ratio	exp. ratio	calc. cross section [mb]	exp. cross section [mb]
^{195}Tl	85.9%	76.9%	1320	473 ± 95
^{196}Tl	8.9%	16.6%	134	102 ± 20
^{194}Tl	2.1%	6.5%	32.3	40 ± 8
^{196}Hg	1.0%	-	10.8	-
^{195}Hg	1.5%	-	23.1	-
^{193}Au	0.4%	-	7.69	-
^{192}Au	0.2%	-	4.62	-

7.3 Determination of the influence of the surface roughness of different materials on the adsorption enthalpy

Experimental and methods

For quantification of the roughness of the surface of quartz glass and α-aluminium oxide plates, surface roughness measurements were performed by Maxim Saifulin at the Helmholtz Institute Mainz. A 100x magnification objective was used with a KEYENCE VK-X3000 Series Confocal Laser Scanning Microscope. This setup resulted in a measurement area of $144.7\,\mu m \times 108.5\,\mu m$ on both the quartz glass plates and the α-aluminium oxide plates. The samples were identical in material and manufacturer to the columns used in the thermochromatography experiments (see Chapters 3.1.1 and 3.2.1, respectively). Before evaluating surface roughness parameters, the acquired topographical data was preprocessed by subtracting the mean plane to correct for sample tilt, ensuring accurate analysis of the surface height distribution.

Further evaluation was done by Katharina Hermainski. A factor between the size of the 'photographed' surface excerpt and the 'actual' size was calculated using the software Gwyddion. Afterwards this factor was implemented into the C++ code of the Monte Carlo simulation as it was proposed by Zvára.[59]

Results

A comparison of the height profiles of the quartz glass and α-aluminium oxide plates gives insight to the roughness of both materials. The taken images as well as the corresponding height profiles of the surfaces are shown in figure 7.3.

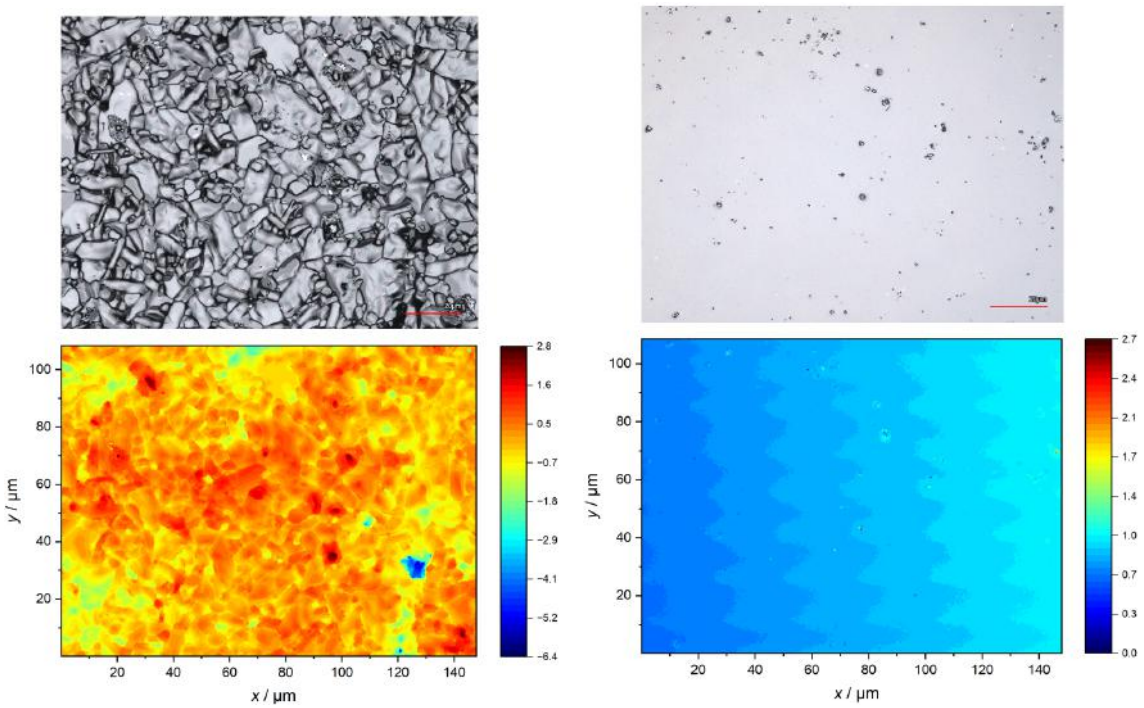

Figure 7.3: Laser scanning images and corresponding height profiles of α-aluminium oxide (left) and quartz glass plates (right), measured using a CLSM by Maxim Saifulin. The height profiles were plotted by Katharina Hermainski.

The determined surface roughness parameters, the seize of the 'photographed' and the 'actual' surface as well as the calculated factors for both examined surfaces are shown in table 7.6.

Table 7.6: Determined mean surface roughness parameters R_a and S_a, the mean area A of the 'photographed' and the 'actual' surface as well as the calculated factors F for the α-aluminium oxide and quartz glass plates. The evaluation was done by Katharina Hermainski.

Material	R_a [μm]	S_a [μm]	$A_{\text{pic.}}$ [μm^2]	$A_{\text{act.}}$ [μm^2]	F
SiO_2	0.0070±0.0003	0.0080±0.0003	15697	15797±20	1.006±0.001
α-Al_2O_3	0.41±0.02	0.429±0.001	15697	19300±200	1.23±0.01

Implementing the calculated factors into the Monte Carlo simulation and simulating experiment Tl-He-700 with the parameters shown in table 4.1 yields to the following adsorption enthalpies.

$$-\Delta H_{\text{ads};A}^{\text{rough.}} = 124\,\frac{\text{kJ}}{\text{mol}}$$

$$-\Delta H_{\text{ads};B}^{\text{rough.}} = 186\,\frac{\text{kJ}}{\text{mol}}$$

Discussion and interpretation of the results

By comparing the adsorption enthalpies determined in chapter 4.2.1 (-123^{+3}_{-2} kJ/mol and 185^{+4}_{-8} kJ/mol) and the values from the previous chapter it becomes clear that they fit well within the scope of the error. This means that the differing surface roughness of the different materials is negligible in this case and the implementation of the surface factor into the Monte Carlo simulation is not necessary for the evaluation.